Rational Design of Pd-Based Catalysts for Selective Alkyne Hydrogenations

THÈSE N^{O} 5235 (2011)

PRÉSENTÉE LE 5 DÉCEMBRE 2011

À LA FACULTÉ DES SCIENCES DE BASE
LABORATOIRE DE GÉNIE DE LA RÉACTION CHIMIQUE
PROGRAMME DOCTORAL EN CHIMIE ET GÉNIE CHIMIQUE

ÉCOLE POLYTECHNIQUE FÉDÉRALE DE LAUSANNE

POUR L'OBTENTION DU GRADE DE DOCTEUR ÈS SCIENCES

PAR

Rocio Micaela CRESPO QUESADA

acceptée sur proposition du jury:

Dr A.-S. Chauvin, présidente du jury
Prof. L. Kiwi, directrice de thèse
Dr D. Berthomieu, rapporteur
Dr D. Buluchev, rapporteur
Prof. G. Laurenczy, rapporteur

ÉCOLE POLYTECHNIQUE
FÉDÉRALE DE LAUSANNE

Suisse
2011

"The only certainty is that nothing is certain"

Plinio il Vecchio

Acknowledgments

First of all, I would like to thank Prof. Lioubov Kiwi-Minsker for accepting me in her group early in 2007 to do my master's diploma thesis, which ultimately led to the start of my PhD later that year. I have enjoyed these past 4 years of work, in which she's given me advice, ideas, support and trust. Furthermore, I'd like to thank her as well for the warmth she's always shown in the personal relations.

The financial support of the Swiss National Science Foundation (Grant n° 200021-118067) which made this thesis possible is highly appreciated.

Many sections of this thesis were performed in collaboration with other laboratories around the globe. A special thank you to Ryan Dykeman from Prof. Dyson's Laboratory of Organometallic and Medicinal Chemistry (EPFL-LCOM), with whom I worked since the very beginning of my thesis. After many years of common work, nanoparticle synthesis, reactions, NMR measurements, endless discussions and over 500 e-mails exchanged (I checked) we made it! I would also like to thank Prof. Younan Xia, Byungkwon Lim and Mingshang Jin from Prof. Xia's Department of Biochemical Engineering (Washington University, USA) for synthesizing exquisite shape-tailored Pd nanoparticles and for the input and feedback received during our collaborations.

Many thanks to Prof. Gabor Laurenczy, Dr. Dorothée Berthomieu and Dr. Dimitri A. Bulushev for reviewing my thesis, as well as Dr. MER Anne-Sophie Chauvin for presiding the jury. I also owe a thank you to those who reviewed the earlier drafts of this dissertation,

with special mention to Fernando Cárdenas Lizana and Prof. Kiwi-Minsker.

Throughout a PhD one has the opportunity to encounter and work with many different people from the university, which can be a very enriching and pleasent experience. From the EPFL, I'd like to thank:

- From the GGRC, Prof. Albert Renken, who can not only critically advise and revise you, but who also always welcomes you into his office with a smile if you need him. All the past and present PhD students and postdocs I had the pleasure to work with: Kim, Martin, Marina, Natasha, Madhav, Bryan, Edi, Igor, Anne-Laure, Pauline, Ameya, Charline, Julien, Jean-Michel, Artur, Daniel and Fernando.
- From CIME, Marco, Fabienne, Danièle, Barbora, Nicolas and Vincent. Thank you for your advice and expertise in XPS and especially the patience with my rookie mistakes during my "flight hours" with the electron microscope.
- Mme. Szuman and Madeleine for the administrative assistance given during the past five years.
- All the skillful staff from the Atelier de Chimie, who can build a whole installation out of a few tubes and screws. Jacky Gremaud and Marie Jirousek for the lab supplies and for not killing us each time we forgot to bring the blue trolley back down after picking up a gas bottle.
- PAP and Yoann Dind for putting up with my computer experiments and somehow anarchic laboratory computer administration.
- My three diploma students: Gaël Peng, Artur Yarulin and Clément Voisard who simply survived me.

Many thanks to all the people I met here and spent time with outside work: Pamela, James, Lisa, Erika & Jochen, Aga & Michal, Blanca & Michal, Pietro & Simone, Carmen & Henning, Irene & Leonidas. I sincerely hope I haven't forgotten anyone!

And since the most important acknowledgments go at the end, I must devote some words to my family, with whom I've gone so far, who walked me through life always encouraging me to learn how to walk for myself. The dear family who always supported me and who is still always by my side during the good and the rough times despite the distance.

Lastly, the most important thanks goes to my loving husband without whom I wouldn't have been able to endure the sometimes rough (but sometimes fun) voyage of a PhD, and with whom I've discovered a new dimension in life: our son Leonardo. Thank you for your charm and laughter and your unconditional support and love, always.

Abstract

Traditionally, the search for active and selective catalysts involved a rather tedious "hit-and-miss" approach in which hundreds, if not thousands catalysts were tested until the optimal substance was identified. With the advancing theoretical understanding of catalysis and the development of computational power, a new era of *rational catalyst design* is dawning. This approach, grounded on first principles, is based on new advances in synthesis, characterization and modeling with the ultimate aim of *predicting the expected behavior* of a catalyst based on chemical composition, molecular structure and morphology. The rational design of a catalyst is a complex process which spans across several levels of scale.

In this thesis, the pursuit of a rational design for Pd-based catalysts effective in alkyne hydrogenations is presented. A multi-level integrated approach was thus applied ranging from the nano-scale design of the active sites for a specific reaction, taking into account its structure sensitivity, to the micro-scale design of the supported Pd nanoparticles including metal-additive and metal-support interactions as well as mass and heat transfer phenomena.

In order to rationally design a catalyst at a nano-scale, i.e. a catalyst's active site, several methodologies have been hitherto applied, such as the study on single crystals or model catalysts. Here we present the use of metal nanoparticles with tuned sizes (5-30 nm) and shapes (cubes, octahedra and cube-octahedra) prepared via colloidal techniques. These nanoparticles can be tested per se and represent a new generation of model catalysts,

complementing single crystal studies, which inherently lack the complexity of industrial catalysis.

However, metal nanoparticles, especially those prepared in a controlled manner in order to tailor their shape and size, require the use of stabilizing and/or capping agents capable of directing their growth. These substances can mask the true catalytic behavior of the nanoparticles. Thus, it is of great importance to study the interactions of the active phase with the substances that are in close contact with it, in the so-called meso-scaled level of rational catalyst design. Therefore, the effect of the nature of the stabilizing agent on the catalytic response was studied, as well as the promoting effect of some of these substances. Finally, a methodology was developed capable of eliminating organic stabilizing agents from the surface of nanoparticles without compromising their morphological stability.

The knowledge gathered in the first two levels can be applied further to reach the micro-scale rational catalyst design. In this thesis, a final catalyst consisting on well-defined stabilizer-free supported Pd nanoparticles was used in the hydrogenation of acetylene.

This deep study of the catalytic behavior of well-defined Pd catalysts throughout several levels of scale and complexity have given us the tools needed to perform a rational catalyst design for alkyne hydrogenations. Depending on the specific reaction, the active phase can be optimized in terms of the desired activity and selectivity and can be tuned even further with the use of specific additives. Finally, the appropriate support also exerts a promoting effect on the nanoparticles and ensures their anchoring in addition to avoiding heat and mass transfer artifacts.

KEYWORDS: Rational catalyst design, structure sensitivity, palladium, hydrogenations.

Version abregée

Traditionnellement, la recherche des catalyseurs actifs et sélectifs avait lieu à travers d'une méthode empirique dans laquelle centaines, ou milliers de catalyseurs étaient testés jusqu'à l'identification de la substance optimale. Cependant, avec l'avancement de la compréhension théorique de la catalyse et le développement d'une forte puissance computationnelle, on se trouve à l'aube d'une nouvelle ère de conception de catalyseurs sur mesure. Cette méthode est basée sur la synthèse, la caractérisation et la modélisation avec le but de prévoir le comportement d'un catalyseur en regardant sa composition chimique, sa structure moléculaire et sa morphologie. La conception de catalyseurs sur mesure est un procédé complexe qui s'étend à travers de nombreux niveaux d'échelle.

Dans cette thèse, on présente la poursuite d'une conception sur mesure de catalyseurs à base de Pd pour des hydrogénations d'alcynes. Une approche intégrée a été appliqué à plusieurs niveaux depuis la conception des sites actifs à échelle nano, tout en considérant leur possible sensibilité à la structure, jusqu'à a l'échelle micro du catalyseur supporté dont les interactions métaux-additif et métaux-support et les phénomènes de transfert de chaleur et masse ont été considérées.

Plusieurs méthodes ont été appliquées jusqu'au présent pour concevoir des catalyseurs sur mesure à échelle nano, comme par exemple l'étude sur des monocrystaux et des catalyseurs modèles. Ici on présente l'utilisation de nanoparticules métalliques à forme et taille contrôlées préparées en solution colloïdale. Ces nanoparticules peuvent être considérées

comme une nouvelle génération de catalyseurs modèle tout en complémentent les études avec des cristaux parfaits, qui marquent la complexité des catalyseurs industriels.

Cependant, les nanoparticules présentes dans les catalyseurs supportés sont rarement isolées. En particulier, celles préparées avec des formes et tailles contrôlées nécessitent l'intervention d'agents stabilisants et/ou "coiffants", qui peuvent guider la croissance des cristaux. Ces substances peuvent aussi cacher le vrai comportement du catalyseur. Il est donc très important d'étudier les interactions possibles de la phase active avec les substances qui sont en contact intime avec elle. Ce type d'étude est la conception sur mesure à l'échelle méso. Dans cette thèse, l'effet de la nature des agents et leur possible effet promoteur ont été étudiés. En outre, une méthode capable d'éliminer ces substances de la surface des nanoparticules sans modifier leur morphologie a aussi été développée.

Les connaissances acquises dans les deux premiers niveaux d'échelle ont ensuite été appliquées pour arriver à la conception sur mesure à l'échelle micro. Un catalyseur complet basé sur des nanoparticules supportées avec forme contrôlée, libres d'agents stabilisants, à été utilisé pour élaborer sa conception sur mesure à l'échelle nano-micro. Cette étude approfondie du comportement d'un catalyseur supporté à base de nanoparticules de Pd à travers d'une série de niveaux d'échelle et de complexité a permis d'acquérir les outils nécessaires pour concevoir des catalyseurs à façon pour des hydrogénations C≡C. Selon la réaction, on peut optimiser la phase active pour obtenir l'activité et sélectivité désirées. En outre, le comportement observé peut être modifié ultérieurement avec l'aide d'agents stabilisants/de "coiffage" pertinents. Pour finir, le type de support peut aussi être choisi dans le but de modifier la performance catalytique des nanoparticules ainsi que pour assurer leur immobilisation, ou bien pour s'assurer de l'absence de problèmes de transfert de chaleur et masse.

Mots-clés: Conception de catalyseurs sur mesure, sensibilité à la structure, palladium, hydrogénations.

Contents

List of symbols

Abbreviations

AAS	Atomic absorption spectroscopy
AIN	Acetoin
AOT	Sodium di-2-ethylhexylsulfosuccinate
ATR-IR	Attenuated total reflection infrared spectroscopy
CNF	Carbon nanofibers
CSTR	Continuous stirred tank reactor
CTAB	Cetyltrimethylammonium bromide
CVD	Chemical vapor deposition
EDX	Energy dispersive X-ray spectroscopy
GC	Gas cromatography
IL	Ionic liquid
MBA	2-methyl-3-butan-2-ol
MBE	2-methyl-3-buten-2-ol

MBY	2-methyl-3-butyn-2-ol
MCT	Mercury cadmium telluride
MEA	Monoethanolamine
MFC	Mass flow controller
NMR	Nuclear magnetic resonance
PFR	Plug flow reactor
PVP	Poly (vinyl pyrrolidone)
RDS	Rate determining step
SEM	Scanning electron microscopy
SMF	Sintered metal filters
SMSI	Strong metal support interactions
TEM	Transmission electron microscopy
TLD	True lens detector
TOF	Turnover frequency
TTAB	Tetradecyltrimethylammonium bromide
UHV	Ultra high vacuum
XPS	X-ray photoelectron spectroscopy
XRD	X-ray diffraction

Greek Symbols

ρ	Density	$[\mathrm{g\,m^{-3}}]$

σ_1	Active site type 1	
σ_2	Active site type 2	
τ'	Modified residence time	$[\mathrm{g\,s\,m^{-3}}]$
τ	Residence time	[s]
τ	Tortuosity	[-]
$\theta_{\mathrm{i,k}}$	Coverage of compound i on active site k	[-]
ε	Porosity	[-]

Roman symbols

ΔG	Free energy change	
$\Delta\mathrm{H_R}$	Enthalpy of the reaction	$[\mathrm{kJ\,mol^{-1}}]$
$\Delta\mathrm{T_{max}}$	Maximum temperature difference	[K]
μ_{i}	Viscosity of compound i	[Pa s]
$\mathrm{C_i}$	Concentration of compound i	$[\mathrm{mol\,m^{-3}}]$
$\mathrm{d_{at}}$	Atomic diameter	[nm]
$\mathrm{D_{eff,i}}$	Effective diffusivity	$[\mathrm{m^2\,s^{-1}}]$
$\mathrm{D_i}$	Diffusivity of compound i	$[\mathrm{m^2\,s^{-1}}]$
$\mathrm{d_p}$	Nanoparticle diameter	[nm]
$\mathrm{d_{rel}}$	Relative diameter	[nm]
$\mathrm{d_{sph}}$	Equivalent spherical diameter	[nm]
$\mathrm{F_i}$	Massic flowrate of compound i	$[\mathrm{g\,s^{-1}}]$

$k^{***}_{j,k}$	Kinetic constant of reaction j on active site k	$[\mathrm{mol\,mol^{-1}_{Pd_{surf}}\,s^{-1}}]$
$k^{**}_{j,k}$	Kinetic constant of reaction j on active site k	$[\mathrm{mol\,mol^{-1}_{Pd_{surf}}\,s^{-1}}]$
$k^{*}_{j,k}$	Kinetic constant of reaction j on active site k	$[\mathrm{mol\,mol^{-1}_{Pd}\,s^{-1}}]$
k_{eff}	Effective thermal conductivity	$[\mathrm{W\,m^{-1}\,K^{-1}}]$
$K_{i,k}$	Adsorption constant of compound i on active site k	$[\mathrm{L\,mol^{-1}}]$
m_{cat}	Mass of catalyst	[g]
M_i	Molecular mass of i	$[\mathrm{g\,mol^{-1}}]$
Q_i	Volumetric flowrate of compound i	$[\mathrm{m^3\,s^{-1}}]$
R_i	Transformation rate of i	$[\mathrm{mol\,mol^{-1}_{Pd}\,s^{-1}}]$
S_i	Selectivity towards compound i	[-]
V_i	Molar volume of compound i	$[\mathrm{cm^3\,mol^{-1}}]$
V_R	Catalytic bed volume	$[\mathrm{m^3}]$
w_i	Mass fraction of compound i	[-]
x_{100}	Fraction of atoms located on (100) crystal planes	[-]
x_{111}	Fraction of atoms located on (111) crystal planes	[-]
x_{edge}	Fraction of atoms located on edges	[-]
X_i	Conversion of compound i	[-]
x_i	Molar fraction of compound i	[-]
D	Dispersion	[-]
m	Number of atoms along the edges of a crystallite	

N	Number of atoms	
T	Temperature	[K]
z	Coordination number	

Subscripts

A	Alkane
B	Bulk
bulk	In the bulk
D	Dimers
E	Alkene
edge	Edge atoms
eff	Effective
h	Surface atom type
I	Isomers
i	Generic compound
in	At the inlet
j	Number of nearest neighbors
j	Reaction path
k	Type of active site
out	At the outlet
plane	Plane atoms

S	Surface
T	Total
Y	Alkyne

Part I

Introductory Section

Chapter 1

Introduction

1.1 Context and motivation

The concept of *rational catalyst design*

Catalysis represents most of the present chemical, petrochemical, and life-sciences industries [1]. In terms of the transition-state theory, catalysts reduce the potential energy barrier over which the reactants must pass to form products, which in turn increases the rate of the reaction [2]. The catalytic hydrogenation of multiple carbon-carbon bonds is a type of reaction of special relevance due to its importance in the bulk and fine chemical industries [3–5].

The search for ever more *active* and *selective* catalysts has long been the goal of surface scientists and engineers. For most of the era of catalyst production, the methodology applied for finding and improving these catalysts has been an empirical "trial-and-error" approach, where there was little input of detailed theoretical understanding of catalysis. This approach could be better described as *catalyst development* [6] and, as depicted in Figure 1.1, it was based on an iterative "hit-and-miss" process where the catalysts were systematically modified from run to run in order to find the best candidate. One of the most famous examples of such methodology is perhaps the search for a catalytic substitute to

the scarce and expensive osmium in Haber-Bosch's process for ammonia synthesis. Alwin Mittasch, in collaboration with Georg Stern and Hans Wolf, embarked in this quest and thousands of trials were made, after which at least a thousand mixtures were tested [7]. Early in 1910 they identified iron promoted by potassium oxide and alumina as the most effective catalyst for this application, which is still commercialized by BASF.

With the advancing theoretical understanding of catalysis and the development of computational power, a new era of *rational catalyst design* is dawning. This approach, grounded on first principles, is also depicted in Figure 1.1 and it is based on new advances in synthesis, characterization and modeling with the ultimate aim of *predicting the expected behavior* of a catalyst based on chemical composition, molecular structure and morphology [8,9].

This methodology has thrived in the past few years, as witnessed by the exponential increase in the number of scientific articles published in the field during the last three decades. Nowadays, the detailed theoretical prediction of the state of adsorbed species can be validated experimentally with the aid of well-defined model surfaces under controlled reaction conditions (Ultra high vacuum, UHV), granting a precious and deep understanding of the structure-function relationship at a molecular level. Nonetheless, in order to understand catalysis, assessing the differences in structure between ideal single-crystal surfaces and the real catalysts used industrially is necessary. This so called "material gap" must be added to the difference in reaction conditions between UHV experiments and real industrial operation, or "pressure gap" [8,9]. This exemplifies the great advancements achieved in surface science and catalysis but it also underlines the necessity of further research to extrapolate the basic knowledge acquired through careful simulation and experimentation to real operating catalysts.

From nano to macro

In heterogeneous catalysis, the reactants/products and the catalyst are in different phases. Heterogeneous catalysts can be either bulk or supported, depending on the degree of dis-

Figure 1.1: Catalyst development flow chart depicting both the traditional "hit-and-miss" method and the more recent rational catalyst design approach. Adapted from [6].

persion of the active phase. Thus, a supported catalyst is usually made of three easily discernible components:

- the *active component/phase,* which is responsible for the catalytic behavior and is finely dispersed.
- the *support*, whose main function is to confer a high surface area to the active component ensuring its dispersion and preventing it from agglomeration.
- the *additives*, which modify the electronic properties, morphology or prevent/exert selective poisoning of the active component thus affecting the catalytic response of the latter.

An interesting feature that can be inferred from Figure 1.1 is the fact that the rational catalyst design spans over multiple levels of complexity, from the very basic molecular or nano-scale involving the active sites to the final macro-scale design of the industrial reactor where the catalyst is bound to operate. Indeed, it is of outmost importance to bear in mind that the overall performance of a catalyst depends not only on the behavior of the active component alone. The possible promoting or poisoning effects of the additives present in the formulation, as well as eventual support effects, together with the micro and macro structure of the support and the design of the reactor are all key factors that must always be pondered when assessing the performance of a given catalyst.

Therefore, to fully exploit the potential of a catalyst, the rational catalyst design approach must be integrated across several levels of complexity as presented in Figure 1.2.

- A nano-scale design concerning the active phase alone where the optimal active site is identified.
- A meso-scale design where the interactions between active phase and additives/support is assessed.

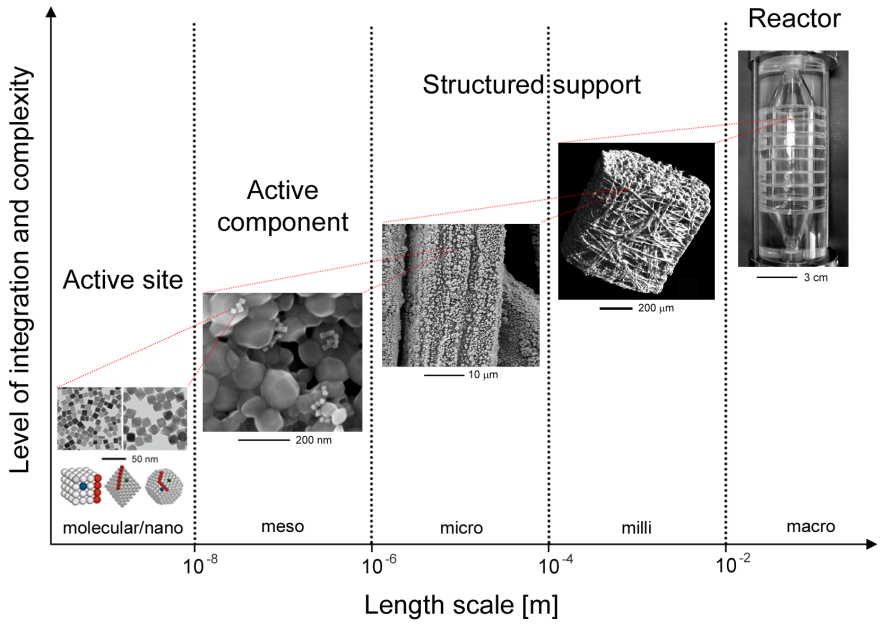

Figure 1.2: Rational catalyst design spans over several levels of scale and complexity.

- A micro-scale design where the support structure is tailored to meet the physical requirements of the reaction under study (thermal, mechanical, etc.).
- A milli-scale design where the catalyst is found in its final state.
- A macro-scale design which involves the design of the chemical reactor where the catalyst usually operates under kinetic regime.

Objectives of this thesis

The *main objective of this work* is the rational design of a Pd based catalyst for triple carbon-carbon bond hydrogenations focusing on the nano to micro levels. In order to do so, the material and pressure gaps found at the nano level must be "crossed over" through the study of well defined, yet real catalysts under real operational conditions. Furthermore, the effect and interactions between the optimized active phase and the additives/support must also be considered and studied at the meso-micro levels.

1.2 Structure of the present work

The present thesis is articulated around the combined use of modelling and experimental testing in order to develop an understanding of the structure-function relationship of supported Pd nanoparticle catalysts in triple carbon-carbon bond hydrogenations.

The first part of the thesis is an introductory section in which the current state of the art in the field of heterogeneous catalysis relevant to this work is reviewed (**Chapter 2**). **Chapter 3** presents the procedures used for preparing the catalysts studied as well as the characterization techniques employed throughout this work.

The second part gathers the experimental results obtained during this thesis.

Nano-scale rational catalyst design

In **Chapter 4**, unsupported well-defined shape and size-tailored Pd nanoparticles are tested in the liquid-phase selective hydrogenation of 2-methyl-3-butyn-2-ol. A two-site mechanism is proposed for describing the observed kinetics and explaining the differences observed in catalytic behavior with nanoparticle morphology. Finally, a prediction model is developed and an optimum nanoparticle size and shape is proposed.

From nano to meso-scale rational catalyst design

Chapter 5 analyzes how the stabilizing agents used to synthesize the size and shape-controlled nanoparticles used in the previous chapter may alter their catalytic performance. In it, Pd nanoparticles stabilized with different substances are tested under the same reaction conditions in the liquid-phase selective hydrogenation of 2-methyl-3-butyn-2-ol. The differences observed are rationalized in terms of stabilizer nature and their type of interaction with the active metal.

Although in some cases the stabilizing agents may merely block the active sites of the nanoparticles, a careful choice and/or design of these compounds which are in intimate

contact with the active phase can have promoting effects on the nanoparticles' activity and selectivity. In **Chapter 6**, the possible explanations to the promotion observed in the selective hydrogenation of 1-hexyne when N-containing ligands are used as stabilizers of Pd nanoparticles are presented and discussed.

Chapter 7 deals with the removal of the stabilizing agents surrounding shape and size-tailored nanoparticles through UV-Ozone cleaning, a mild procedure able to eliminate such compounds without compromising their morphological stability. The effect of such compounds on nanoparticle morphology and catalytic behavior is assessed by testing stabilizer-free supported Pd nanoparticles in the selective hydrogenation of acetylene.

From nano to micro-scale rational catalyst design

Once freed from their stabilizing agents, Pd nanoparticles can be tested in order to study the structure sensitivity of chemical reactions over "clean" supported metallic crystal planes. The results obtained for shape-tailored supported Pd nanoparticles in the hydrogenation of acetylene are thus presented in **Chapter 8**.

Conclusions and outlook

Finally, **Chapter 9** summarizes the results obtained in the preceding chapters and it also presents some concluding remarks and outlook.

Chapter 2

State of the art

This chapter presents the current state of the art in the field of catalysis relevant to this work. In each section, a brief theoretical introduction of each phenomena is presented, together with a literature review of the work published concerning the subject.

2.1 Structure sensitivity of catalytic reactions

One of the key factors affecting the catalytic behavior of the active phase is the interplay between its properties and the reacting molecules. Several explanations, such as mechanistic (quantum size effects, metastability of nanoparticles, defect sites), electronic (ionization potential, binding energies) as well as geometric (fraction of atoms with different coordination environment, adsorption mode changes) have been coined to tackle this complex phenomenon [3, 10–16].

2.1.1 The concept of structure sensitivity

Before the 1960s, it had become clear that the rates of some catalyzed reactions, expressed per unit area or turnover frequency (TOF), were independent of metal particle size and were at first described as facile. If, on the other hand, some form of TOF dependence with

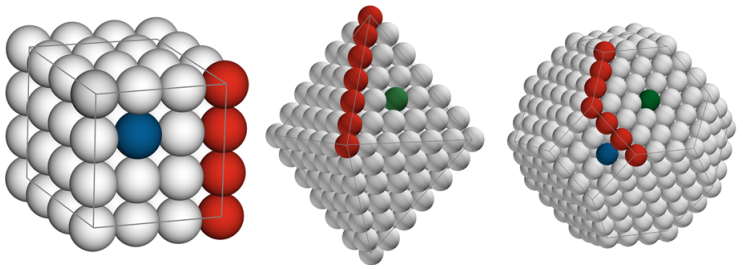

Figure 2.1: Schematic representation of the surface atoms found on three common *fcc* crystallites. ● low coordination number atoms, such as corner and edge atoms, ● (111) plane atoms and ● (100) plane atoms.

particle size was observed, the reaction was referred to as demanding [17].

For nanoparticles larger than 2-3 nm geometric explanations are often applied for interpreting the structure sensitivity phenomenon. Taylor suggested already in 1925 that demanding reactions required a specific grouping or ensemble of surface atoms [18]. To emphasize the supposed role of surface morphology on catalytic behavior, the terms facile and demanding were subsequently replaced by *structure-insensitive* and *structure-sensitive*, respectively [19]. It is, however, more likely that every reaction will show a degree of structure sensitivity, depending on the stringency of its requirements for an active center [17].

Van Hardeveld and Hartog published the results of numerous calculations describing the atomic arrangement in small metal particles [20]. Surface atoms vary essentially in their coordination numbers. Thus, mainly three types of surface atoms can be found on a metal nanoparticle (Figure 2.1): low coordination number atoms such as corner and edge atoms, depicted in red; plane atoms, denoted in blue and green depending on their crystallographic orientation; and high coordination number atoms, which correspond to the atoms directly underneath the outermost layer but which are still accessible to reacting molecules. With the aid of these calculations, it is possible to determine the change in the fraction of a given type of surface atom with nanoparticle size for any common shape (cube, octahedra, tetrahedra, cube-octahedra, etc.) as seen in Figure 2.2. The fraction of a given type of surface atoms, sometimes referred to as Taylor's ratio [21], is defined as the

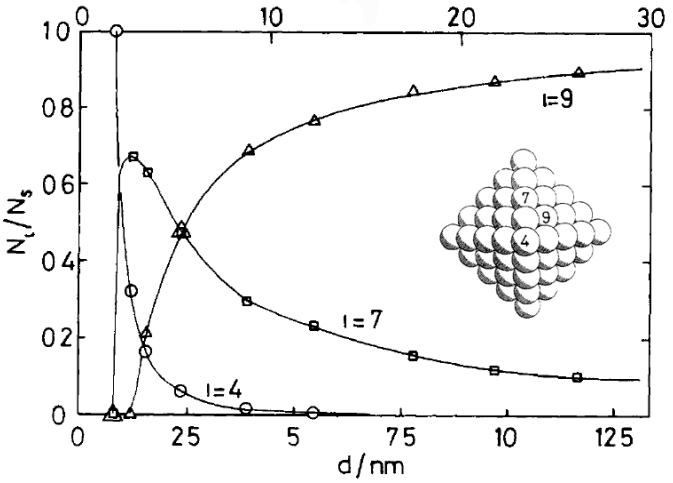

Figure 2.2: Variation of the fraction of surface atoms of coordination number I as a function of particle size. Adapted from [17,20].

ratio of that type of surface atom to the total of surface atoms:

$$x_h = \frac{N_h}{N_S} \tag{2.1}$$

Therefore, reactions can be classified in four categories depending on how the TOF varies as a function of particle size (Figure 2.3). The TOF of structure-insensitive reactions does not depend on particle size (curve 1). Structure-sensitive reactions, on the other hand, can behave in two opposite ways: TOF may decrease when the particle size decreases, this is termed a negative particle size effect or *antipathetic* structure sensitivity (curve 2); or it may increase for decreasing particle size, this is called a positive particle size effect or *sympathetic* structure sensitivity (curve 3). TOF may also go through a maximum if small particles present an antipathetic structure sensitivity, whereas large ones sympathetic effect (curve 4) [22].

It is worth mentioning that a variation in shape also implies important morphological differences: cubes only present (100) plane atoms, octahedra present only (111) plane atoms and cube-octahedra (spheres) a mixture of both (Figure 2.1). This will provoke another

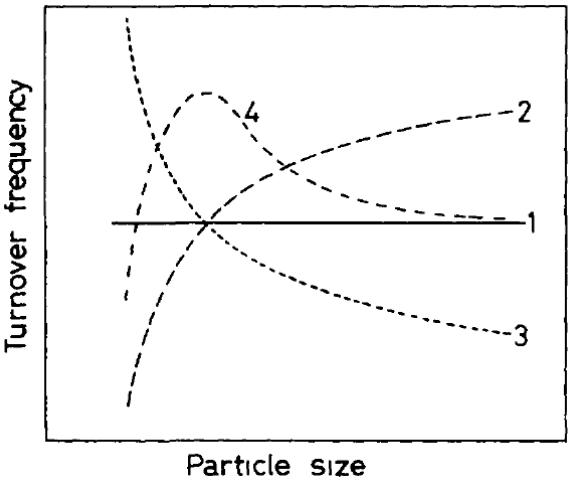

Figure 2.3: Possible forms of TOF dependence on particle size [17].

type of structure-induced effect, i.e. a shape-effect, especially if each type of surface atom possesses a different reactivity. The aforementioned shape- and size-effects could be used in structure-sensitive reactions for *rationally designing* the catalyst [23].

It appears to be a characteristic of reaction systems showing structure sensitivity that product selectivity can also exhibit marked variations. It seems probable that molecules may react at different rates on different types of sites. In some cases, product distribution changes markedly with particle size, presumably as alternative sites become available [21]. However, it is a question not much discussed in literature, whether a given reaction can proceed on a variety of types of active center, each having its characteristic TOF [17].

2.1.2 Structure-sensitivity reported in the literature

Structure-sensitivity studies began primarily on single crystals [24–27]. However, these systems lacked the complexity normally present under industrial operation, in both the catalyst (material gap) and the reaction conditions (pressure gap). Model catalysts [28–30] were thus developed so as to present well-defined metal nanoparticles, although the conditions used were still far from the real ones. With the development of simple preparation

routes for obtaining size-controlled metal nanoparticles during the past decade [4,5,31,32], along came numerous attempts to use such nanoparticles in structure-sensitivity studies under real operational conditions. Furthermore, the synthesis of shape-controlled metal nanoparticles was achieved more recently, and expanded the opportunities of research.

Indeed, there is a wealth of information concerning the study of structure-sensitive reactions using size and shape-tailored nanoparticles in either supported or unsupported (colloidal) form. Structure-sensitive reactions commonly studied include Heck and Suzuki coupling reactions [11,33,34], oxidation reactions [35–37], electron transfer reactions [38–41] and hydrogenation reactions [42–54]. The most common metals used as catalysts in these reactions include Pd [11,33,36,43,44,48–54], Pt [35,37–39,55–57], Rh [42] and Au [45–47], amongst others.

Given that size control was achieved earlier than shape control and considering that the former can be performed much more easily and over a wider variety of metals, most publications present size-effect studies over spherical nanoparticles (or cube-octahedra) of different sizes. Qualitative explanations of such effects were based on either electronic [49–51,54] or geometric effects, depending mainly on the size range used. However, some attempts have been made to explain the observed structure-sensitivity of chemical reactions through theoretical analysis or modeling. For instance, thermodynamic and kinetic calculations based on the change of chemical potentials upon adsorption [16,58,59] have been used as a tool for the kinetic analysis of size-dependent activity and selectivity. When geometric effects are coined as explanation to the observed behavior, either sympathetic or antipathetic structure-sensitivities are observed and interpreted using Van Hardeveld's and Hartog's surface statistics approach. Thus, oxidation and hydrogenation reactions usually show antipathetic structure sensitivities, with the exception of acetylene hydrogenation on Au [46] and CO oxidation on Pd [36] whereas Heck and Suzuki coupling reactions were found to take place mainly on low coordination surface atoms [11, 33]. Unfortunately, satisfying

quantitative correlations between observed activity and surface morphology are however hard to find in the literature. Furthermore, little attention is paid to changes in selectivity with particle size, with only a few exceptions [43,44,52].

Structure-sensitivity studies based on shape-effects are less abundant and are performed basically over shape-tailored Pt nanoparticles. Thus, electron transfer reactions [38–40], isomerizations [55] and several hydrogenation reactions [56,57,60,61] were performed over several different shapes in order to elucidate the role of each type of crystallographic plane on their catalytic behavior.

Despite that much has been achieved and explained with the aid of single crystals, model catalysts, theoretical calculations and experimental results, much is still to be done in this field, especially concerning the structure sensitivity of hydrogenation reactions over Pd size and shape-tailored nanoparticles. There is undoubtedly a lack of quantitative correlations between experimental results, kinetic data and especially reaction mechanisms which could be filled with careful kinetic studies over well-defined nanoparticles.

2.2 Selective C≡C hydrogenations over Pd-based catalysts

Selective C≡C hydrogenations are widely employed in fine chemicals production. Moreover, they are performed to meet the need for a complete elimination of alkynes from alkene feedstocks in industrial polymerization processes [3,62,63].

For such reactions, Pd was found to be the most active and selective catalyst [63,64]. Although olefin hydrogenation over Pd is faster than that of the acetylenic counterpart, the latter gets preferentially reduced because of its higher adsorption strength. The acetylenic compound thus acts as a poison against olefin hydrogenation. This form of selectivity has been identified as thermodynamic [63].

Possible reactive intermediates during hydrogenation of alkynes are presented in Figure 2.4. Both π-adsorbed (I) and doubly σ-bonded (II) structures have been considered

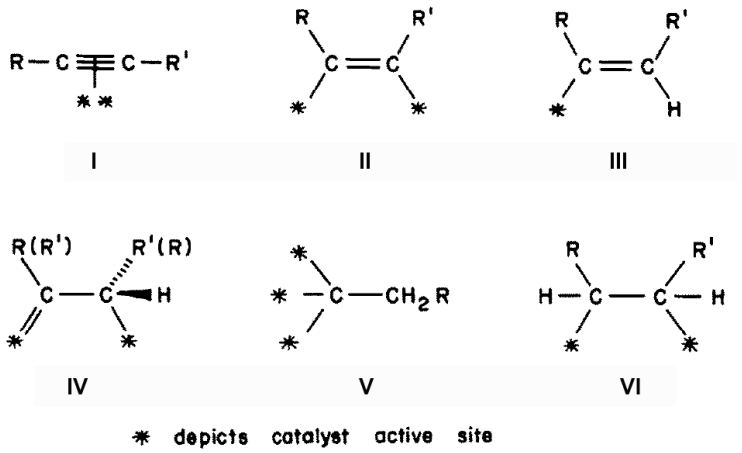

Figure 2.4: Possible reactive intermediates during alkyne hydrogenations [63].

for the adsorbed acetylenes. Compounds III-V have been proposed as intermediate species leading to the products of the reaction. While III lies on the pathway to the olefin, IV and V have been suggested as additional species leading to the fully hydrogenated product. Intermediate VI arises from the adsorption of the olefin, leading also to the alkane. V is valid only for mono-substituted acetylenes [63].

The catalytic hydrogenation of alkynes and its functionalized derivatives has been extensively studied and covered in books and review papers since the 1960's. The search for more selective catalysts is, however, still active and numerous studies have been published recently [3].

2.2.1 Structure sensitivity of alkyne hydrogenations

Size-effects

The first study tackling the issue of nanoparticle size-effects was published in 1983 by Boitiaux et al. [50]. The data published since then concerning size effects in the selective hydrogenation of multiple carbon-carbon bonds is however rather controversial, although most studies show that an increase in metal dispersion decreases TOF. The low activities shown by very small nanoparticles is usually explained by strong complexation of the

highly unsaturated electron-rich alkyne to the electron-deficient atoms with low coordination number predominant on their surfaces. Moreover, β-PdH phase disappears with decreasing metal particle size [65]. Some studies have shown this phase to be responsible for the direct alkyne hydrogenation to alkane [12], while some reports did not find this detrimental effect [3, 66].

Gas-phase hydrogenations Numerous investigations were carried out on Pd size effects in two-phase alkyne and alkadiene hydrogenations [3, 51, 52, 54]. Recent studies revealed that TOF does not change with particle size when normalized per number of Pd atoms in the incomplete (111) facets [29, 30]. The reaction was therefore proposed to be structure-sensitive but size-independent for nanoparticles larger than 4 nm. It was then concluded that the hydrogenation reaction took place mainly on the (111) facets of these Pd nanoparticles. By-product distribution was also found to change with Pd nanoparticle structure: Pd_{111} crystals showed lower selectivity to the isomerization with respect to the alkane.

Different Pd crystals facets were shown to have different activities in the essential carbon laydown process during alkyne hydrogenations. If carbon dissolution is not a favorable process, as on (111) facets, then the emergence of energetic bulk-dissolved hydrogen to the surface of finite-sized particles can be predicted to shift the reaction selectivity toward the formation of alkane. This paradigm claims the decisive role of carbon in creating the active site for the hydrogenation of a C≡C bond [67]. With pulse hydrogenation, in situ TEM, in situ XPS, and HRTEM it was demonstrated that carbon dissolves into the palladium lattice (mainly in the near-surface region) and a palladium-carbon surface phase builds up in the early stage of the reaction depending on the Pd particle structure.

Much effort has been devoted to studying the structure sensitivity of acetylene hydrogenation. During the hydrogenation of acetylene, TOF is usually found to increase with nanoparticle size. For instance, Borodzinski reported an increase of TOF with size over Pd/SiO_2 catalysts with Pd diameter of 4, 5, 7, 16, and 26 nm. The size effect observed was

claimed to be "geometric" in nature since the catalysis involved large ensembles of surface atoms [52]. Furthermore, Ruta et al. studied the behavior of monodispersed particles of 8, 11, and 13 nm [68]. TOF was found to increase with Pd particle size in the 8−13 nm range. On the other hand, studies conducted by Tribolet et al. [69] showed a decrease in TOF of 1 order of magnitude for particles smaller than 3 nm. This observation was rationalized taking into consideration the stronger adsorption of alkynes on electron deficient small nanoparticles. The data available point towards the independence of selectivity on nanoparticle structure, although the support was found to exert an influence on it [68,69].

Liquid-phase hydrogenations For acetylenic alcohol hydrogenations, TOF and selectivity to the olefinic product were shown to increase with the particle size: Pd nanoparticles of 7.5 nm size exhibited a 6-fold higher activity and 14% higher selectivity in hydrogenation of 2-methyl-3-butyn-2-ol (MBY) in comparison with 2.5 nm particles [70,71]. A correlation between a spherical Pd nanoparticle size and TOF for the hydrogenation of allyl alcohol was found for the particle size between 1 and 2 nm [49]. Analyses indicated that the hydrogenation kinetics are dominated by electronic effects for the smallest particles (<1.5 nm diameter) and by geometric effects for larger particles (1.5-1.9 nm diameter).

Shape-effects

There are very few data on Pd nanoparticle shape-effect for alkyne hydrogenations available in the literature. Most shape-effect studies have been performed over Pt nanoparticles for a wide variety of reactions [38,39,55–57,60,61].

Shape control allowed tailoring the activity and selectivity in 2-butyne-1,4-diol hydrogenation [72]: PVP-stabilized cubic Pd nanoparticles were compared to spherical particles produced by radiolytic reduction. The influence of size on TOF was found to be opposite for the two catalysts: higher spherical particle sizes led to higher TOF, while the highest TOF was observed for the smallest nanocubes. Selectivity to 2-butene-1,4-diol in both

cases increased with the particle size showing the existence of a selectivity/activity optimum which depends on the catalyst structure and size. However, the preparation method and stabilizing agents used for both nanoparticles were completely different, thus rendering their conclusions questionable. Pd nanohexagons were compared to nanospheres in the hydrogenation of 2-methyl-3-butyn-2-ol, and Pd_{111} was found to be the active site of the reaction [48]. In this case, the stabilizing agents used were also different in each case.

There is, therefore, an urge for shape-effect studies in alkyne hydrogenation reactions, especially on well defined nanocrystals synthesized with the same stabilizing agent.

2.2.2 Case studies: 2-methyl-3-butyn-2-ol, acetylene and 1-hexyne

Three types of alkyne hydrogenations were used as case studies throughout this thesis, namely the hydrogenation of 2-methyl-3-butyn-2-ol, 1-hexyne and acetylene.

The hydrogenation of acetylene is a key unit operation within the ethylene process. Indeed, traces of acetylene can poison the catalysts used for the downstream ethylene polymerization, for which it must be hydrogenated selectively to ethylene. The behavior of Pd on the hydrogenation of 1-hexyne illustrate the effect of chain length on its catalysis. Furthermore, 2-methyl-3-butyn-2-ol include the effect of multi-substitution other than being an industrially relevant reaction in the perfume and food industries.

Hydrogenation of 2-methyl-3-butyn-2-ol (MBY)

The hydrogenation of 2-methyl-3-butyn-2-ol (MBY) to 2-methyl-3-buten-2-ol (MBE) and the fully hydrogenated alkane, 2-methyl-3-butan-2-ol (MBA) is generally agreed to proceed following the reaction network shown in Figure 2.5 [44,48,73,74]. MBY can be either semi-hydrogenated to MBE through *path a*, directly hydrogenated to MBA through *path c*, or it can oligomerize through *path d* to give rise to C-10 dimers. On the other hand, MBE can be over-hydrogenated to MBA through *path b*.

Metallic palladium is known to be the most selective metal for MBY hydrogenation

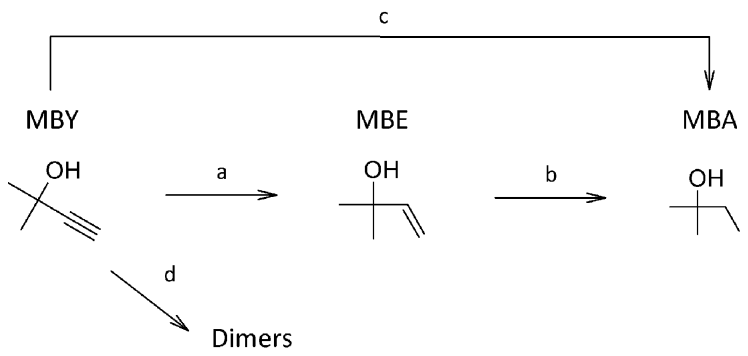

Figure 2.5: Reaction network for the hydrogenation of MBY.

to MBE, followed by Ni, Pt and Rh. However, its catalytic performance can be strongly influenced by the dispersion of the nanoparticles, nature of support, the use of promoters and additives. The correct combination of these factors is of crucial importance in achieving the best possible catalytic activity-selectivity-stability compromise [3, 75, 76].

Acetylene hydrogenation

The network of the reaction is shown in Figure 2.6. The target reaction is the semi-hydrogenation to ethylene (*path a*), but over-hydrogenation of ethylene to ethane may occur (*path b*). Besides, the direct hydrogenation of acetylene to ethane can also take place (*path c*) [77]. Approximately 25-30% of the acetylene consumed is transformed into oligomers and polymers (*path d*), commonly referred to as "green oil" [78]. The high selectivity towards oligomer formation is a peculiar feature of acetylene. Indeed, with increasing substitution, the selectivity of oligomers formation decreases due to steric interferences in the C–C bond forming step [3].

The complexity of this system is the reason for the slow progress in establishing a molecular mechanism. Nowadays, the most accredited mechanistic scheme is the one elaborated by Borodzinski [79]. It assumes the existence of specific types of active sites, created on the catalyst surface by carbonaceous deposits. On A sites (A_1 and A_2) only acetylene

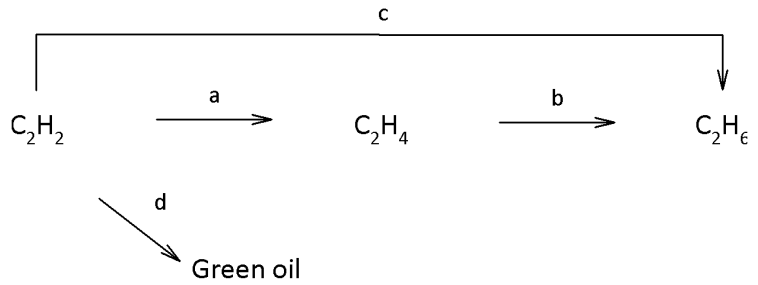

Figure 2.6: Reaction network for the hydrogenation of acetylene.

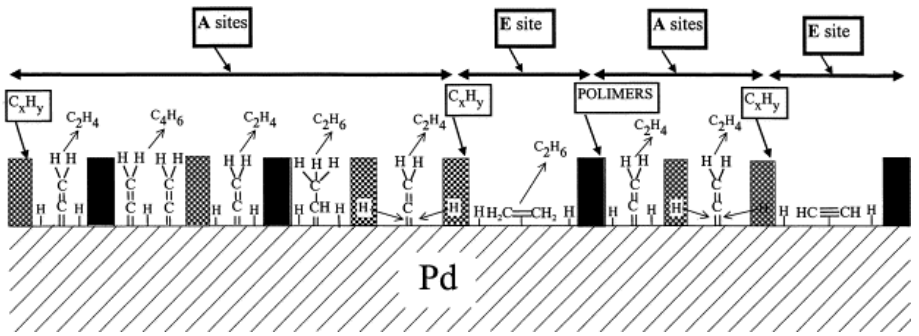

Figure 2.7: A simplified representation of active sites created on a palladium surface by carbonaceous deposits [79].

and hydrogen can be adsorbed. On E sites, all gases (acetylene, ethylene and hydrogen) can be adsorbed. The gaps in A_1 sites are so small that only acetylene can be adsorbed as vinylidene, perpendicularly to the surface, and is selectively hydrogenated to ethylene by competitively adsorbed hydrogen atoms. Ethylene is unable to adsorb on A_1 sites because of steric constraints. A_2 sites exist on deposits where acetylene is non-competitively adsorbed and hydrogenated by hydrogen spill-over. The gaps in E sites are sufficiently large to competitively adsorb ethylene, acetylene and hydrogen. These sites are responsible for the unwanted hydrogenation of ethylene to ethane. A schematic representation of the catalytic surface is shown in Figure 2.7.

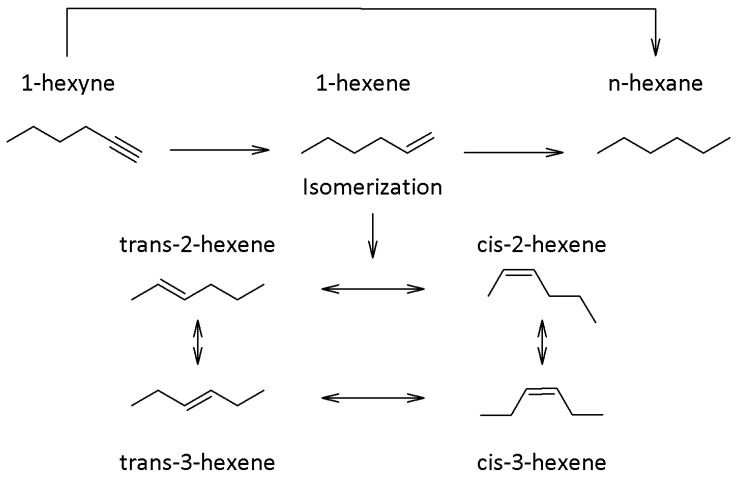

Figure 2.8: Reaction network for the hydrogenation of 1-hexyne. Adapted from [80].

Hydrogenation of 1-hexyne

There is not much information available in the literature concerning the hydrogenation of 1-hexyne. Nonetheless, the reaction is thought to proceed through a standard alkyne mechanism, as proposed by Anderson et al. [80] (Figure 2.8). In this case, however, oligomerization is not encountered probably due to the considerable chain length of the molecule [3]. Instead, isomerization of 1-hexene towards its 2-hexene and 3-hexene counterparts is possible and observed experimentally [43, 81].

2.3 Shape and size-tailored synthesis of metal nanoparticles

A key to overcoming the "material gap" presented in Chapter 1 and to studying the structure sensitivity of metal nanoparticles, is the synthesis of shape-controlled metallic nanoparticles which present well-defined surface structures. Furthermore, in order for them to be catalytically active, their size must be controlled in the nanometer range. An ulterior restriction should be applied to the synthesis of metallic nanoparticles for catalytic applications: both size and shape must be varied in absence of other perturbations, such as stabilizing agents, solvents, pH, etc. [20]. The development of simple and versatile meth-

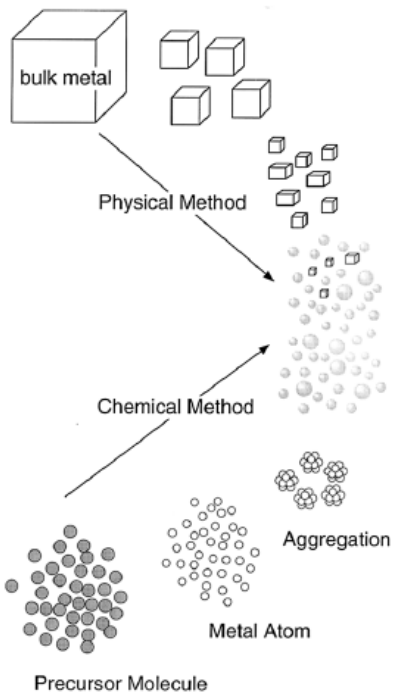

Figure 2.9: Preparation methods of metal nanoparticles [4].

ods for the preparation of nanoparticles in a size and especially shape-tailored manner has attracted significant attention in the past 10 years [4,5,13,31,32,82].

Colloidal metal nanoparticles can be prepared in two distinct ways, i.e., by subdivision of bulk metal (top-down methods), which utilizes physical methods, or by growing nanoparticles from metal atoms (bottom-up methods), in which liquid-phase colloidal chemistry is used or where nanoparticles are grown to clusters in the gas phase (Figure 2.9). In the synthesis of metal nanoparticles through top-down techniques, despite the fact that they allow the preparation of high quantities of nanoparticles, size control is very difficult to achieve.

Colloidal techniques present a valid alternative in formation of monodispersed nanostructures of desirable size. Colloidal methods are advantageous because no specialized equipment is necessary, solution-based processing and assembly can be readily implemented and large quantities of nanoparticles can be synthesized [32]. Typical ways of preparing col-

loidal solutions of size and shape-controlled nanoparticles include the chemical reduction of metal precursors, electrochemical synthesis and controlled decomposition of organometallic compounds [4, 5, 13, 82]. Chemical reduction methods imply the mixing of the metal precursor together with a reducing agent (alcohol, hydrogen, sodium borohydrate, hydrazine hydrate) and a stabilizing agent (such as polymers [14, 33, 83–85], dendrimers [86], block copolymer micelles [87], surfactants [88–91], electrolytes [92]), which prevents the agglomeration of the nanoparticles. Colloidal nanoparticle synthesis involves two distinctive steps: nucleation and growth.

Nucleation

This step is crucial for obtaining size and shaped nanoparticles. Nuclei can be generated in situ (homogeneous nucleation) or added to a growth solution (heterogeneous nucleation) [32]. It is unclear if the precursor compound is reduced to zero-valent atoms first, which aggregate into seeds, or if the unreduced metal species begin forming seeds prior to reduction [31].

In homogeneous nucleation, seed formation occurs according to LaMer's model. This model states that there is a critical concentration above which nucleation takes place. This phenomena has a thermodynamic driving force, since the supersaturated solution is not energetically stable. The overall free energy change, ΔG, is the sum of the free energy due to the formation of new volume and the free energy due to the new surface created. After the nuclei are formed from the solution, they grow via molecular addition, which relives the supersaturated step [13]. When the concentration drops below the critical level, further nucleation is discouraged and all subsequent growth occurs on pre-existing nuclei [32].

In order to obtain monodispersed size and shape-tailored nanoparticles, the nucleation step must occur rapidly, which can be achieved by slowly building up the concentration of metal ions in solution [32]. Depending on the reduction conditions used during nucleation, i.e., under thermodynamic or kinetic control, seeds can be either monocrystalline (from

which platonic shapes can be obtained) or twinned (from which unconventional shapes can be synthesized), respectively [31].

Growth

At this point a seed can grow into a nanoparticle through the addition of new metal atoms. This step is controlled by a competition between a decrease in bulk energy (which favors growth) and an increase in surface energy (which favors dissolution). Smaller particles grow more rapidly than the larger ones because the free energy, i.e. the driving force, is larger for smaller particles than for larger ones provided that they are larger than the critical size.

2.3.1 Size-controlled growth

Due to the difficulty inherent to observing the growth mechanism of metal nanoparticles, size control synthesis methods have been developed empirically. To achieve it, many parameters have been varied (stabilizer, reducing agent, solvent, pH) [4,5]. Size control has been achieved with the aid of several different stabilizing agents.

Poly (vinyl pyrrolidone) (PVP) is the most widespread linear polymer used as stabilizer given its versatility and its growth-directing capability on a wide variety of metals. For instance, a series of monodispersed PVP-stabilized Pd nanoparticles in the range of 1.7 to 6.6 nm diameter were prepared by a one-pot technique [11,14] as well as nanoparticles in the 3-6 nm range through a stepwise growth reaction [33]. With its use, size control was achieved for several other metals metals, such as Pt [93,94], Rh [95] and Ru [96].

Excellent size control may also be provided in an easy way by a reverse microemulsion technique, where the nanoparticles grow in a thermodynamically stable aqueous nanocore of reverse micelles [88,89,97–100]. Typical surfactants used in this technique include cetyltrimethylammonium bromide (CTAB) and sodium di-2-ethylhexylsulfosuccinate (AOT). Size control is achieved by changing the water-to-surfactant ratio in the micellar so-

lution. This approach has been successfully applied to conduct size-effects studies [43,44,88] over Pd nanoparticles. Furthermore, block-copolymers have also been used for this application [101].

Other less frequent stabilizing agents used for controlling the size of metal nanoparticles include dendrimer templates [49] and ligands [102–104].

2.3.2 Shape-controlled growth

Controlled synthesis procedures have been published for various nanoobjects, such as nanospheres [56,105], nanorods [106–108], nanocubes [109–111], nanocages [112,113], nanoplates [114, 115], nanoprisms [116], etc. Pt is one of the most extensively studied metal in shape-controlled synthesis of nanoparticles [38, 39, 55–57], although much research has been done on shape control of Pd nanoparticles as well [110, 112, 117–119].

In colloidal syntheses, shape control can be achieved by employing molecular capping agents that selectively adsorb to specific crystal planes. The general strategy to generate shape anisotropy during nanocrystal growth is by stabilizing a particular facet through this molecular interaction; growth is limited on the crystal plane where binding is strong and promoted on the crystal plane where binding is weak. The stabilizers presented in Section 2.3.1 may also restrict the nanoparticles growth in a desirable direction giving rise to different morphologies [120–122]. Empirical synthetic experiments have shown a wide variety of molecules that can facilitate shape control, including large surfactants, polymers, bio-molecules, small molecules such as adsorbed gas, and even atomic species, such as different metal ions [32].

Surfactants such as CTAB and AOT have been proven successful in producing shape-controlled nanoparticles of Au [121, 123] and Cu [124], respectively. Furthermore, gold nanorods were prepared via a seed-mediated sequential growth process involving the use of citrate-stabilized seed crystals and their subsequent growth in the presence of CTAB [125]. Improved structure-directing abilities were shown also for a plethora of di- and triblock-

copolymers [120]. These systems are extremely delicate, since the choice of the adsorbate must be carefully done for a given crystal structure. Although shape-control was achieved by this means, much is still to be done to elucidate the mechanism.

The most successful route to produce noble metal colloids with controlled shape is probably the polyol process employing PVP as capping agent. The role of the polymer is twofold: it acts as stabilizing agent, preventing aggregation of metal nanoparticles and retaining a uniform colloidal dispersion, and is used as a shape-directing agent, promoting reduction onto specific crystal faces while preventing reduction onto others [32]. Although the actual mechanism for this selectivity is still under consideration, PVP is believed to bind preferentially to the (111) and (100) planes. As seen in Figure 2.10, PVP has been demonstrated to be an excellent shape-control agent for Ag, Au, Pt colloids [126, 127] after optimizing the reaction parameters (temperature, reactant concentrations, solvent viscosity, reaction time, reactant injection time and volumes, and the addition of ionic impurities the reaction flask).

The addition of small-molecules or atomic adsorbates to polyol synthesis also allows a morphological control of the thus obtained nanoparticles. These adsorbates selectively block further addition of metal ions on the surface of the growing nanoparticle. For instance, Br^- [118, 119] and Cl^- [36] were found to selectively bind to Pd_{100} crystal planes, thus yielding nanocubes or nanobars. On the other hand, the presence of NO_2 [128] and citric acid [129] favored the formation of Pd nanoparticles bounded by Pd_{111} facets, such as octahedra and decahedra. Silver ions were also found to stabilize (111) facets for Au and Pt systems [127, 130], and subsequent removal of Ag by selective etching was performed without compromising the morphology of the Pt nanoparticles [131].

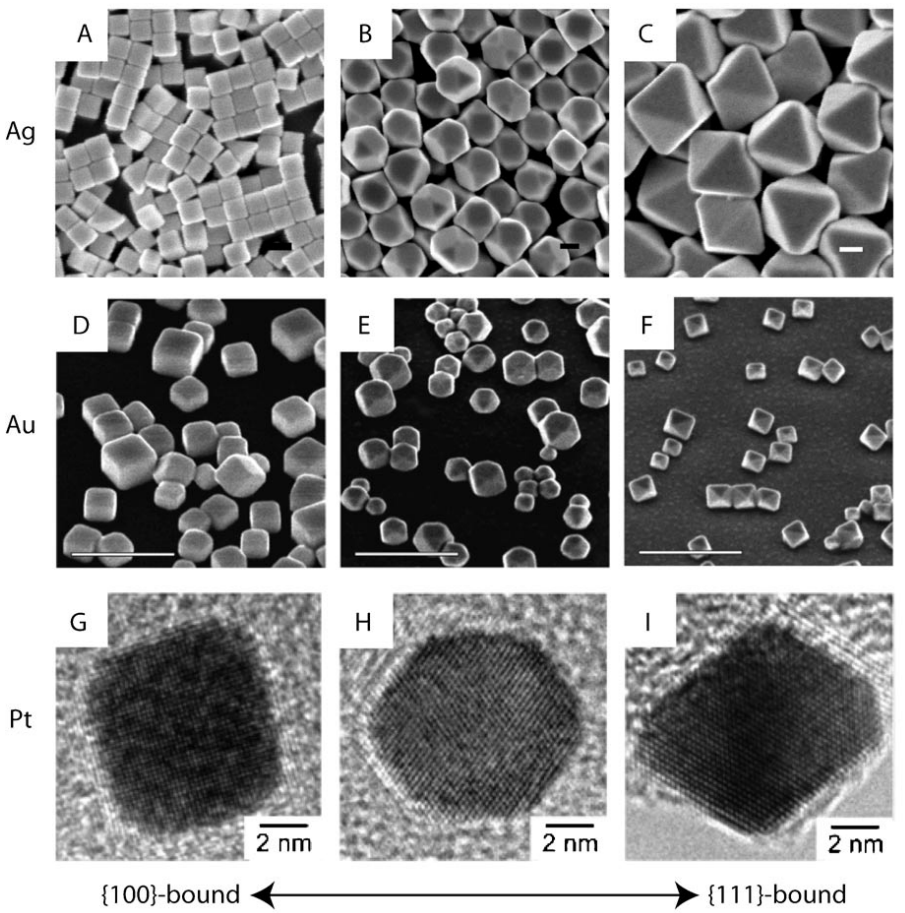

Figure 2.10: Cubes, cube-octahedra and octahedra have been synthesized for Ag (A-C, scale bar: 100 nm), Au (D-E, scale bar: 1 μm), and Pt (G-I, scale bar: 2nm) [32].

2.4 Structured supports for catalytic applications

2.4.1 Types of structured supports

Conventional catalysts are usually supported and used in the form of pellets. Structured supports have open macrostructures leading to low pressure drop during fluid-passage, narrow residence-time distribution and enhanced heat and mass transfer [132]. Monoliths [133, 134], membranes [135], bidimensional glass [136] and carbon fabrics [137, 138] have been used as supports for alkyne hydrogenations. Therefore, three basic types of structured supports can be distinguished:

- Monolith or honeycomb. They are continuous unitary structures containing small parallel channels. The catalytically active material is deposited on or inside the walls of the passages.
- Membrane. The membranes show selectivity in mass transport rates for various compounds present and can combine catalytic reaction in the wall with reactant/product separation.
- Arranged catalysts. They are often made from superimposed sheets of different geometric arrangements covered with the catalytically active phase.

2.4.2 Sintered metal fibers (SMF) as supports

Sintered metal fibers (SMF), consisting of mechanically and chemically stable thin metal filaments (d=2-30 μm) combine the advantages of metal wires with the properties of fibrous materials [139–141]. Available commercially in the form of panels of different compositions, they possess uniform highly porous 3D macrostructures with porosities ranging between 70 and 90%. The high thermal conductivity of the metal fiber matrix provides a radial heat transfer coefficient in the catalytic bed about two times higher compared to randomly packed beds [139], resulting in nearly isothermal conditions in the reactor, which is a

particularly useful characteristic for exothermic hydrogenations. SMF have been used as catalyst supports for gas-phase applications [68, 69, 141–144] as well as liquid-phase reactions [73, 74, 145].

2.4.3 SMF surface modification

The major drawback associated with fibrous supports is their relatively small specific surface area, which can limit the dispersion of the active catalytic phase. To achieve better performances, a non-porous support can be modified by coating with a layer presenting high surface area.

Oxide layers are usually developed via a physical treatment (anodisation [146], plating [147]) or a chemical route (suspension [141], sol–gel [148]). Carbon [149] or Zeolites [142, 150, 151] have also been deposed through direct synthesis on the surface. SMF have been successfully coated with ZnO [73, 74] and Co_3O_4 [152] in our lab.

Carbon materials have long been used as catalyst supports [153,154]. Activated carbons have one main drawback, namely their microporosity. This microporosity induces strong mass transfer influences during catalysis, which can be detrimental for the performance. Graphite, on the other hand, does not present this disadvantage, but its surface area is too low for being a viable catalyst support. Carbon nanofibers (CNF) are a promising alternative since they exhibit a higher surface area, large pore volume and are mesoporous materials. Indeed, CNF have been used in several catalytic applications, although they're mostly studied in hydrogenation reactions, where they've shown superior activities and selectivities as compared to traditional supports [69, 155–157]. CNF can be directly grown on Inconel-based SMF to form a homogeneous and mesoporous layer of graphitic carbon [69, 156].

Many mechanisms have been proposed over the years for the growth of CNF. Most of them rely on the presence of metal catalysts. An early model was developed by Baker and coworkers [158] and outlined in four main steps:

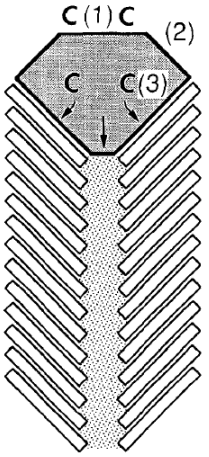

Figure 2.11: One-dimensional CNF growth model from a single metal nanoparticle [159].

- carbon-containing compounds adsorb dissociatively at the metal surface
- carbon dissolves into the bulk of metal cluster
- carbon diffuses through the bulk to the rear end
- the carbon atoms are incorporated into a new graphene sheet of the growing nanofiber.

The growth stops when the buildup of a carbon overlayer prevent further hydrocarbon decomposition. According to the model based on the diffusion through the metal particle, two growth-mode have been identified: tip-growth, if the catalyst particle detaches form the support and is found a the tip of the fiber (Figure 2.11), and root-growth if the particle remains anchored to the support due to the strong interaction between them.

Much like graphite, CNF exhibit are hydrophobic and inert in nature. For many applications, it is therefore suitable to chemically modify the surface to enhance the wettability by polar solvents such as water. In the perspective of supporting metal-containing species on CNF, some preparation methods, such as incipient wetness impregnation, ion-exchange, and organometallic grafting, require surface functionalization. Treatment with strongly oxidizing media in gas or in liquid phase, oxygen-containing groups can be introduced on the surface of CNF [160].

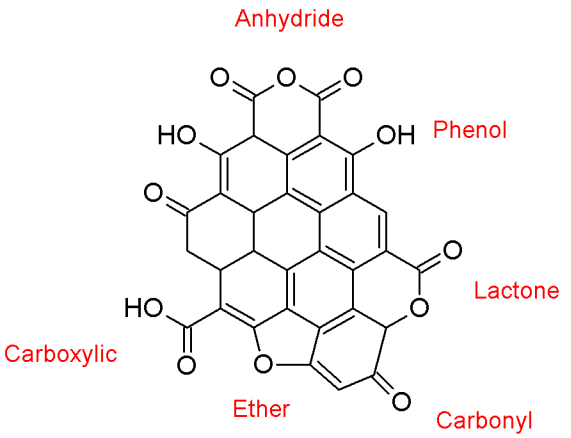

Figure 2.12: Schematic representation of the oxide groups found on the surface of carbon after oxidative treatment.

The surface groups created by oxidative treatments are mainly acidic in character [161]. In Figure 2.12 a schematic representation of the possible surface groups on carbon is shown. They can be divided in four categories: strongly acidic groups (carboxylic and anhydride), weakly acidic groups (lactone and quinone), hydroxylic groups with phenolic characters, and carbonyl groups.

2.5 Enhancement of catalytic performance

In addition to the active phase, secondary components are often included in a catalyst formulation in order to finely tune its performance.

2.5.1 Catalyst promotion through support effects

Supports not only influence metal distribution, structure and morphology of metal particles, surface area and pore distribution contribute also to the internal mass transfer effects. Indeed, the acid/base properties of the support can strongly influence the behavior of the catalyst. Bönnemann et al. [162] compared the activity of Pd on various supports in the hydrogenation of 3-hexyn-1-ol and found that the activity increased in the order

$CeO_2 < C < Al_2O_3 < CaCO_3$. Zakarina et al. [70] compared the activity and selectivity of 1% Pd/SiO_2, 1% Pd/Al_2O_3 and 1% Pd/MgO in MBY hydrogenation, finding that activity and selectivity decreased concomitantly with the acidity of the support in the order $Pd/MgO > Pd/Al_2O_3 > Pd/SiO_2$.

Specific surface area is another factor influencing catalytic performance. In general, Pd catalysts deposited on non-porous supports are believed to be the most selective for hydrogenation of acetylenic alcohols. A decrease in the specific surface area diminishes the influence of internal mass transfer thus increasing selectivity [75].

Finally, supports can also alter a catalyst's performance through electronic interactions [155, 157]. Furthermore, when the metal oxide is reducible, high temperature treatments under hydrogen provoke the formation of intermetallic species which drastically change the catalytic performance. In the particular case of titania, this effect, often referred to as strong metal support interaction (SMSI), has been widely studied and published in one of the most cited articles in catalysis [163]. Indeed, adding a second metal to the catalyst has found countless promoting applications. The first clear example of Pd promotion with a second metal is Lindlar's catalyst [164, 165]. This effect is usually interpreted as follows:

1. An electronic (ligand) effect leading to a change of the relative adsorption strength of the alkyne and alkene and/or decomposition of the β-PdH phase.

2. Geometric (or ensemble) effect, i.e. the dilution of Pd surface atoms decreasing the probability of strongly multi-bonded alkylidine intermediate formation responsible for the direct hydrogenation of alkynes to alkanes [3, 12].

Special attention should be paid to the use of ZnO as a support for Pd catalyst for acetylenic alcohol hydrogenation. In this case Zn should also be considered as promoter giving rise to a PdZn alloy phase. ZnO has been found to readily reduce in the presence of Pd nanoparticles, thus creating an intermetallic PdZn phase which improved the selectivity of

the target product of the catalyst in several hydrogenation reactions [73, 74, 166–171]. In this particular case, Zn is believed to act both through an ensemble effect (especially at high Zn concentrations) by a "skin" model, rather than a progressive front of PdZn phase [167], and through an electronic effect, described as "long-range", which was found to be strong enough to drastically modify the catalytic behavior of Pd in the presence of very small amounts of Zn by rearranging the electronic structure of the active metal [172–174]. The formation of a PdZn phase imposes new adsorption properties on the catalyst, both towards hydrogen and the organic substrate. It has the additional advantage of being a low surface area oxide, which reduces the negative influence of internal mass transfer.

2.5.2 Catalyst promotion through the use of modifiers

The yield of the olefinic hydrogenation product is known to increase considerably in the presence of additives in the reaction mixture (*reaction modifiers*) or in the catalyst formulation (*catalyst modifiers*) such as nitrogen bases (ammonia, quinoline [76,175,176], pyridine, etc.) and sulfur compounds [177]. Tschan et al. [177] studied the effect of different modifiers on the selectivity and activity of amourphous $Pd_{81}Si_{19}$ catalyst in the hydrogenation (3,7,11,15-tetramethyl-1-hexadecyn-3-ol). They concluded that that selectivity towards isophytol (3,7,11,15-tetramethyl-1-hexadecen-3-ol) was improved with modifiers containing a higher number of heteroatoms. Furthermore, the presence of conjugated double bonds was also found to amplify the effect of the modifier, probably due to enhanced bonding to the catalyst surface. The effect mechanism of the nitrogen organic bases is still not quite obvious but is usually interpreted as:

- A "ligand" effect: a nucleophilic modifier increases the electron density of the palladium surface through electron donation from the coordinating ligand [76] that leads to a change in the alkyne/alkene relative strength of adsorption. A decrease in alkene heat of adsorption favors its desorption and increases the selectivity [75, 76, 178].

- Poisoning (site blocking) effect: the least selective sites are blocked by irreversibly adsorbed additive molecules [175, 177].

Chapter 3

Experimental

3.1 Size and shape-tailored Pd nanoparticles preparation

3.1.1 Poly (vinyl pyrrolidone) (PVP) as stabilizing agent

PVP-stabilized Pd nanoparticles were prepared at Prof. Xia's Department of Biochemical Engineering at Washington University. The preparation procedure used is summarized in Figure 3.1 and a detailed description can be found below. All nanoparticles were prepared with PVP as stabilizing agent but different reaction temperatures, reducing and capping agents were used depending on the desired size and shape. In all cases, the final products were collected by centrifugation and washed with ethanol to remove the highest amount of PVP possible.

Cube-octahedral Pd nanoparticles [108]

8.0 mL of an aqueous solution containing 105 mg of PVP and 60 mg of L-ascorbic acid were placed in a 25 mL vial, and pre-heated in air under magnetic stirring at 100 °C for 10 min. Then, 3.0 mL of an aqueous solution containing 57 mg Na_2PdCl_4 was added using a pipette. After the vial had been capped, the reaction was allowed to proceed at 100 °C for 3 h, after which the product was collected by flocculation with acetone.

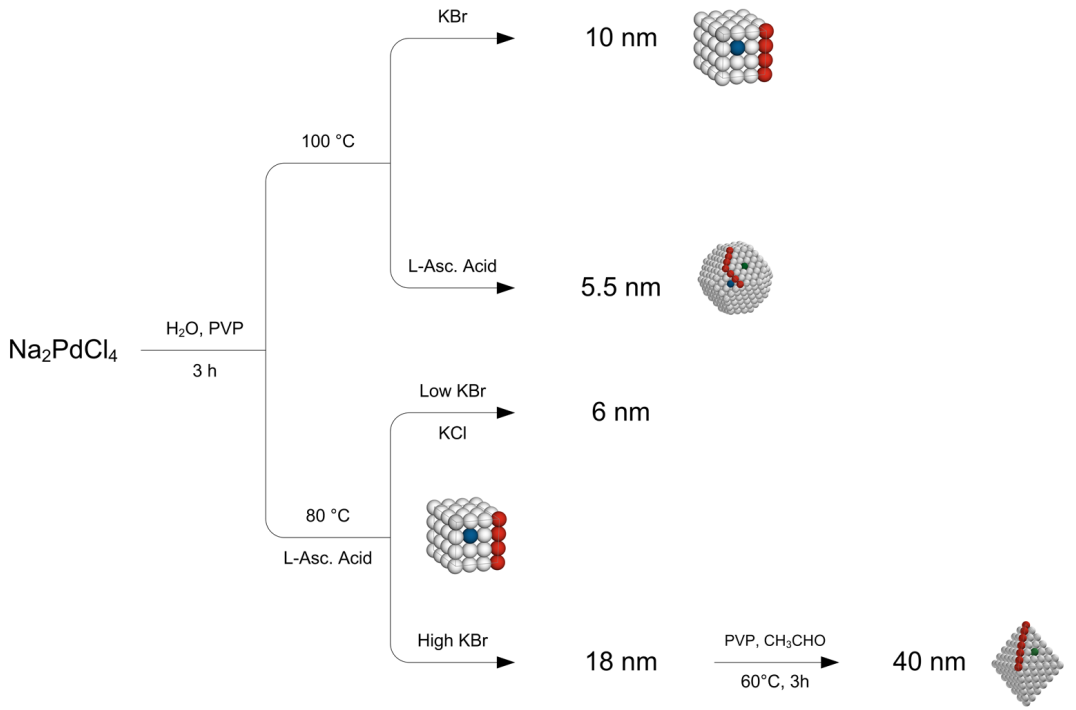

Figure 3.1: Schematic representation of the preparation procedures used for synthesizing differently sized and shaped Pd nanoparticles. All nanoparticles were prepared with PVP as stabilizing agent at a temperature between 80 and 100°C. Different reducing and capping agents were used depending on the desired size and shape.

10 nm cubic Pd nanoparticles [108]

8.0 mL of an aqueous solution containing 105 mg of PVP and 600 mg of KBr were placed in a 25 mL vial, and pre-heated in air under magnetic stirring at 100 °C for 10 min. Then, 3.0 mL of an aqueous solution containing 57 mg Na_2PdCl_4 was added using a pipette. After the vial had been capped, the reaction was allowed to proceed at 100 °C for 3 h, after which the product was collected by flocculation with acetone.

6 nm and 18 nm cubic Pd nanoparticles [36]

8.0 mL of an aqueous solution containing 105 mg of PVP, 60 mg of L-ascorbic acid, and 5 mg and 185 mg of KBr and KCl, respectively, were placed in a 20 mL vial and pre-heated in air under magnetic stirring at 80 °C for 10 min. Then, 3.0 mL of an aqueous solution

containing 57 mg of Na_2PdCl_4 was added using a pipette. After the vial had been capped, the reaction was allowed to proceed at 80 °C for 3 h, after which the 6 nm nanocubes were collected by flocculation with acetone. In order to obtain 18 nm nanocubes, all reaction conditions were kept constant only that KBr was the only capping agent employed (600 mg).

Octahedral Pd nanoparticles

8.0 mL of an aqueous solution containing 105 mg of PVP, 100 μL of CH_3CHO, and 0.3 mL of 18 nm Pd nanocube solution (1.8 mg/mL) were placed in a 25 mL vial, and pre-heated in air under magnetic stirring at 60 °C for 10 min. Then, 3.0 mL of an aqueous solution containing 29 mg of Na_2PdCl_4 was added using a pipette. After the vial had been capped, the reaction was allowed to proceed at 60 °C for 3 h, after which the product was collected by flocculation with acetone.

3.1.2 Sodium di-2-ethylhexylsulfosuccinate (AOT) as stabilizing agent

Pd nanoparticles were synthesized in a reverse microemulsion of water/AOT/isooctane at different water-to-surfactant ratios as described in the literature [100]. Figure 3.2 shows a scheme of the preparation procedure employed.

An aqueous solution of $PdCl_2(NH_3)_4$ (0.05 M) was used as metal precursor (pH 9, adjusted with ammonia), and a solution of hydrazine hydrate (3 M) as reducing agent, giving a N_2H_4 : Pd molar ratio of 60 to ensure complete reduction. Both solutions were then mixed with an isooctane solution of AOT (0.35 M) in order to prepare the microemulsions. Subsequently, both microemultion solutions were mixed and left to react for 1 h at room temperature. Isooctane was then evaporated in a rotary evaporator at 323 K, and the nanoparticles were purified from AOT by cyclic redispersion-centrifugation in methanol.

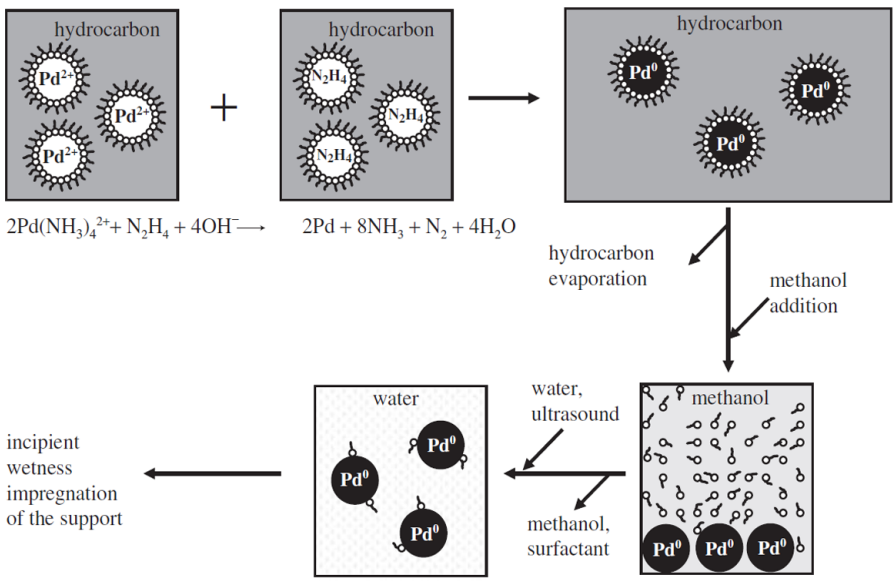

Figure 3.2: Scheme of the the preparation procedure for AOT-stabilized Pd nanoparticles [179].

3.1.3 N-based ligands as stabilizing agent

Two N-based ligands were used in the synthesis of Pd nanoparticles, namely 2,2'-bipyridine (bipy) and an imidazolium functionalized bipyridinic ligand {4,4'-Bis[7-(2,3-dimethylimidazolium)heptyl]-2,2'-bipyridine}bromide ([BIHB]Br_2). While bipy is commercially available, [BIHB]Br_2 was synthesized in-house at Prof. Dyson's Laboratory of Organometallic and Medicinal Chemistry at the EPFL.

[BIHB]Br_2 ligand preparation

Under an atmosphere of nitrogen 4,4'-Bis(7-bromoheptyl)-2,2'-bipyridine (0.638 g) and 1,2-dimethylimidazole (804 mg) in toluene (50 mL) were stirred under reflux for 20 h, after which a white solid formed. The solid was removed by filtration and washed with ether (20 mL) and residual solvent removed in vacuo to give [BIHB]Br_2 (829 mg, 94%) (see Figure 3.3).

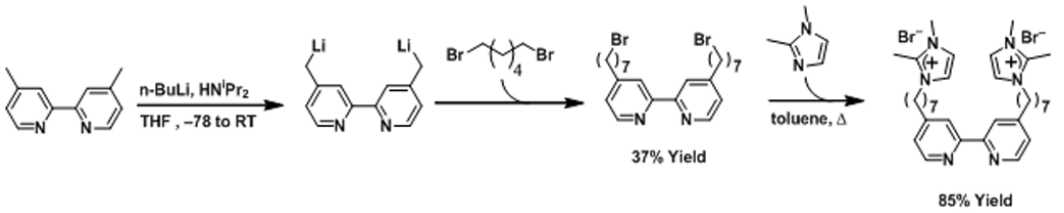

Figure 3.3: Synthetic route for the modified bipyridine stabilizer, [BIHB]Br_2.

Pd nanoparticle preparation

Both bipy and [BIHB]Br_2-stabilized Pd nanoparticles were prepared using the same procedure. In a typical experiment, $Pd(CH_3CO_2)_2$ (5.6 mg), bipy (3.9 mg) in 4 ml of either water or 1-butyl-3-methyl-imidazolium hexafluorophosphate ([bmim][PF_6]) were stirred for 10 min and then placed in an ultrasonic bath for a further 10 min. The mixture was then placed in an autoclave, pressurized to 10 bar under H_2 and stirred for 1 h. The reduction resulted in an opaque black solution, which was then stirred for 1 h while exposed to air. The Pd NPs obtained were purified by centrifugation and redispersed in acetone.

3.2 Support preparation

3.2.1 SMF-based supports

Table 3.1 shows the composition of the different SMF used during this work. SMF-based supports were prepared by surface modification of SMF of different compositions.

Carbon nanofibers grown on SMF

Commercially available Inconel SMF ($SMF_{Inconel}$, Bakaert Fibre Technology, Belgium) were used as a growth-media for CNF. The method of preparation (Figure 3.4) of CNF over $SMF_{Inconel}$ (CNF/$SMF_{Inconel}$) was developed in our group [156].

CNF were grown on SMF filters by the catalytic pyrolysis (chemical vapor deposition, CVD) of ethane in the presence of hydrogen. The synthesis was carried out in a tubular

Table 3.1: Characteristics of filters of sintered metal fibers, SMF.

Material	Composition [wt. %]	Fiber diameter μm	Filter thickness [mm]	Porosity
FeCrAlloy	Cr:20%, Al:4.75%, Ni:0.35%, Mn:0.35%, Si:0.35%, Y:0.3%, Cu:0.15%, P:0.035%, C:0.03%, S:0.01%, Fe: balance	20	0.3	0.71
Inconel 601	Ni:60.5%, Cr:23%, Al:1.25%, Cu:1%, Mn:1%, Si:0.5%, C:0.1%, S:0.015%, Fe:balance	8	0.49	0.81

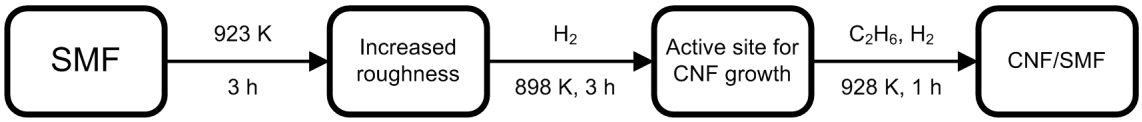

Figure 3.4: CNF coated structured SMF support preparation procedure.

quartz reactor with 24 mm internal diameter posed in a tubular furnace. The temperature was monitored with a thermocouple inserted into the reactor in a protective quartz tube.

Prior to any use, the filters were calcined at 923 K for three hours in order to increase the roughness of the fiber and create the surface sites needed for CNF growth. The calcined SMF filters were then reduced in hydrogen (120 ml(STP) min^{-1}) while the temperature was ramped at 10 °C min^{-1} and held at 898 K for 2 h. Afterwards, the reactor was heated to 928 K and the CVD mixture $Ar : C_2H_6 : H_2 = 80 : 3 : 17$ (600 ml(STP) min^{-1}) was then introduced for 1 h, after which a homogeneous layer of CNF was obtained on the SMF. The newly formed $CNF/SMF_{Inconel}$ supports were cooled down to room temperature under a reductive atmosphere in order to ensure the integrity of the CNF.

ZnO-coated SMF

The preparation procedure for the ZnO/$SMF_{FeCrAlloy}$ support is summarized in Figure 3.5.

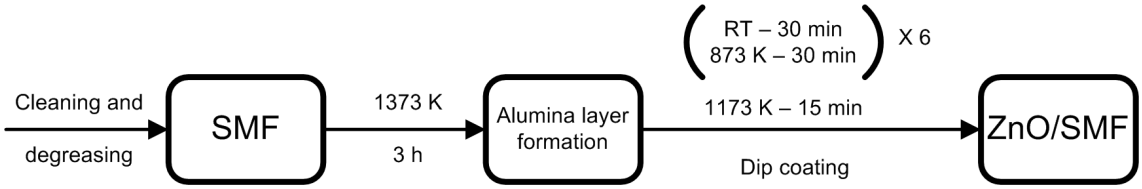

Figure 3.5: ZnO coated structured SMF support preparation.

In order to remove contaminants, the SMF panels were degreased with acetone and then boiled in toluene for 0.5 h twice. To further improve the adhesion of the ZnO layer, SMF are oxidized in air at 1373 K for 3 h. Such treatment is known to lead to the formation of a structured $\alpha - Al_2O_3$ film over the FeCrAlloy, characterized by equiaxed grains on the outer surface.

A thin, uniform ZnO film is prepared using zinc acetate dihydrate and solubility enhancement additives (monoethanolamine, MEA and acetoin, AIN) at a molar ratio of MEA:AIN:Zn = 1:0.5:1. The additives were mixed by sonication prior to the addition of the zinc acetate. The imine that evolves from the reaction of MEA and AIN grants the solution a red-brownish colour, which is used to perform a dip-coating procedure. The gel film thus obtained is air-dried at room temperature for 30 min and then heated at 873 K for 30 min. Since a fast heating is applied, highly oriented ZnO crystals are formed. The coating-heating procedure is then repeated 6 times to achieve a weight gain of roughly 5%. The ZnO coating is then post-annealed at 1173 K for 15 min to promote the formation of island-like grains of ZnO with increased specific surface area.

3.3 Nanoparticle immobilization

When supported catalysts were used in this work, the Pd nanoparticles (prepared following the procedure presented in section 3.1) were immobilized on the structured supports, pre-

pared following the procedure presented in Section 3.2, by incipient wetness impregnation. The impregnated supports were then dried in a vacuum oven. The fresh catalysts were immediately used for catalysis and/or characterization, unless otherwise specified.

3.4 Experimental setup

3.4.1 Liquid-phase hydrogenations

Semi-batch reactor

Liquid-phase hydrogenations (MBY and 1-hexyne) were carried out in a semi-batch stainless steel reactor (250 mL autoclave, Büchi AG, Switzerland) equipped with a heating jacket and a hydrogen supply system (Figure 3.6A). When unsupported colloidal metal nanoparticles were used as catalysts, an 8 blade turbine impeller was used as stirrer. For structured catalysts, an in-house modified cage stirrer shaft was used (Figure 3.6C). In this case, the catalyst was secured to the stirrer cages between two metal gauzes.

Experimental procedure

The reactor was flushed with N_2 and set to the target temperature. The reactor was then flushed with H_2 and brought to the appropriate pressure. The consumption of hydrogen was monitored using a Pressflow gas Controller (BPC-6002) (Büchi, Switzerland) (Figure 3.6B). Samples were periodically withdrawn from the reactor via a sampling tube and analyzed by gas chromatography (GC).

GC analysis for 1-hexyne hydrogenation was performed using an Auto System XL (Perkin Elmer) equipped with a 100 m Petrocol DH 0.25 mm capillary column with a 0.5 μm coating. The pressure of the carrier gas (He) was 280 kPa. The temperature of the injector and the FID was 493 K. The oven temperature was held for 20 min at 333 K, then increased to 373 K at a rate of 10 $\mathrm{K\,min^{-1}}$and held for 7 min and finally increased to

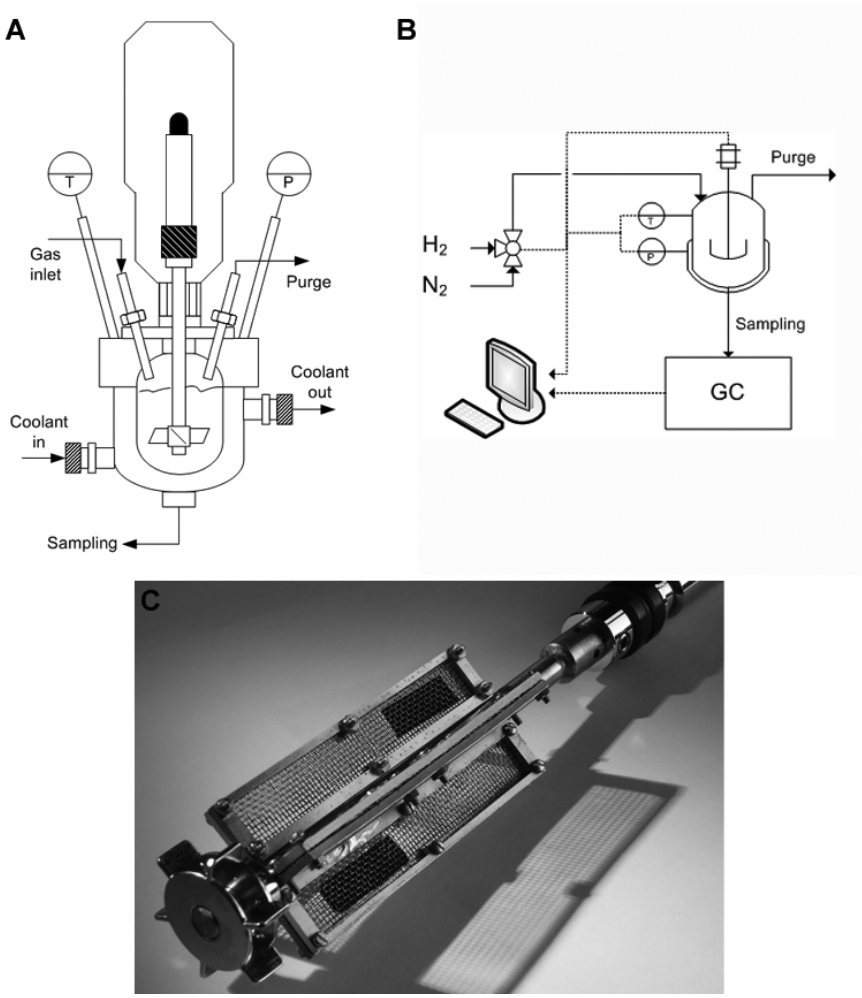

Figure 3.6: Liquid-phase installation: A) detailed scheme of the batch reactor, B) general scheme of the installation and C) detail of the in-house modified cage stirrer shaft.

418 K at a rate of 45 K min^{-1}.

GC analysis for MBY hydrogenation was performed using an Auto System XL (Perkin Elmer) equipped with a 30 m Stabilwax (Crossbond Carbowax-PEG, Restek, USA) 0.32 mm capillary column with a 0.25 μm coating. The carrier gas (He) pressure was 101 kPa. The temperature of the injector and the FID were 473 K and 523 K, respectively. The oven temperature was held for 4 min at 323 K, then increased to 473 K at a rate of 30 K min^{-1}.

Definitions and calculations

The mass fraction concentrations of the reaction mixture components were calculated from the GC area percentages either assuming similar GC-response factors or with the aid of an internal standard. The conversion, selectivity and yield were defined in terms of molar fractions. Molar fractions were calculated from the massic fraction according to the following equation.

$$x_i = \frac{\frac{w_i}{M_i}}{\sum \frac{w_i}{M_i}} \tag{3.1}$$

Conversion was defined as:

$$X_i = 1 - x_i \tag{3.2}$$

Selectivity, on the other hand, was defined as follows.

$$S_i = \frac{x_i}{\sum x_i} 100 \tag{3.3}$$

Yield was defined as shown in equation 3.4

$$Y_i = \frac{X\, S_i}{100} \tag{3.4}$$

Concentrations were calculated assuming that the density of the reaction mixture remained constant and equal to its initial value.

$$C_i = \frac{w_i\, \rho^0}{M_i} \tag{3.5}$$

3.4.2 Gas-phase hydrogenations

Differential tubular reactor for gas feedstocks

Acetylene hydrogenation experiments were carried out in a jacketed tubular reactor with internal diameter 12 mm (Figure 3.7A). A disc of catalyst was placed into the central part of the reactor between two metallic rings to ensure that the position of catalyst was perpendicular to the gas flow. A fixed bed of glass beads inside the reactor was used to homogenize and preheat the flow of reactants upstream of the catalyst. The temperature was controlled by a Juvo thermostat (Type 500, K.K. Juchheim Laborgeräte GmbH, Bernkastel-Kues, Germany). The temperature inside the reactor was kept constant and monitored with a quartz-protected thermocouple.

A differential reactor operating with "once-through" flow has the advantage of functioning, like a continuous stirred tank reactor (CSTR), at one well-defined conversion level. Moreover, this level is directly set by the chosen composition of the entering fluid and the metal loading on the catalytic bed [180].

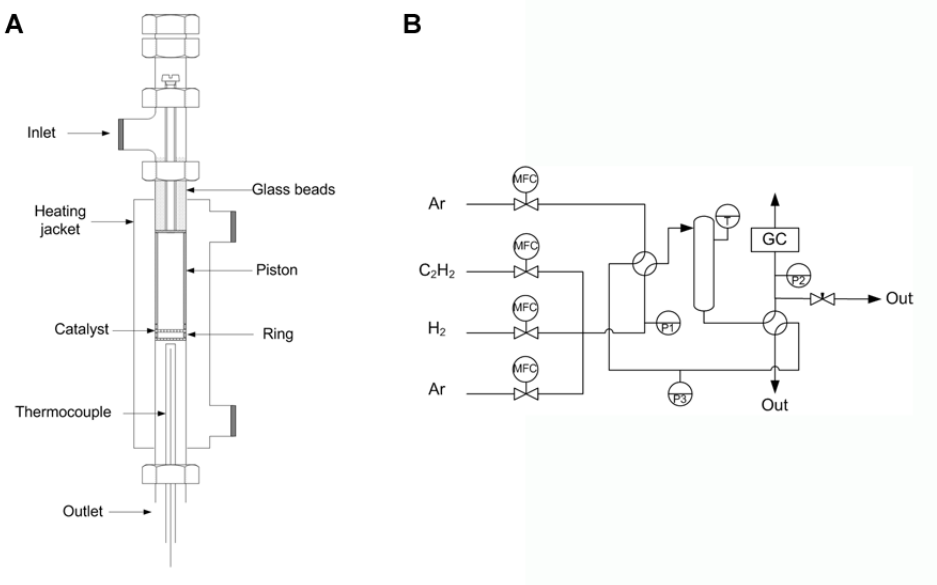

Figure 3.7: Continuous gas-phase installation: A) detailed scheme of the differential tubular reactor and B) general scheme of the installation.

Experimental procedure

Before the catalytic run, the feed mixture consisting on acetylene, hydrogen and argon, was circulated through the bypass and into the GC in order to measure the initial concentrations of the reactants. Simultaneously, argon was flowed through the reactor to prevent catalyst damage. After the first GC injection, the reaction mixture was redirected in the reactor. During the reaction the pressure in the reactor was kept at 1.04 bar.

GC analysis for acetylene hydrogenation was performed using an HP 6890 (Agilent Technology AG, Switzerland) equipped with a 30 m Carboxen 1010 0.53 mm capillary column. The pressure of the carrier gas (He) was 72 kPa. The temperature of the FID and TCD detectors was 253 K in both cases. The oven temperature was raised from 333 K to 453 K at a rate of 13 $\mathrm{K\,min^{-1}}$and held for 2 min. The analysis was repeated every 10 min on-stream.

Definitions and calculations

The conversion of acetylene was calculated from the difference between the reactor inlet and outlet concentrations.

$$X_{C_2H_2} = \frac{C_{C_2H_2,in} - C_{C_2H_2,out}}{C_{C_2H_2,in}} \tag{3.6}$$

The selectivity toward ethylene and ethane were calculated as the molar ratio of ethylene obtained to acetylene converted.

$$S_{C_2H_4} = \frac{C_{C_2H_4,out}}{C_{C_2H_2,in} - C_{C_2H_2,out}} \tag{3.7}$$

$$S_{C_2H_6} = \frac{C_{C_2H_6,out}}{C_{C_2H_2,in} - C_{C_2H_2,out}} \tag{3.8}$$

C_2H_2, C_2H_4, C_2H_6 can be detected by GC analysis. The amount of green oil produced

was then estimated from the mass balance in the reactor, according to equation 3.9.

$$S_{Green\,oil} = 100 - (S_{C_2H_4} + S_{C_2H_6}) \tag{3.9}$$

The transformation rate of acetylene was derived from the mass balance in an ideal plug flow reactor (PFR):

$$\frac{m_{cat}}{F_{C_2H_2,in}} = \frac{m_{cat}\,\tau}{C_{C_2H_2,in}\,V_R} = \int_0^X \frac{dX_{C_2H_2}}{-R_{C_2H_2}} \tag{3.10}$$

and given that the reaction rate is constant and does not depend on conversion, equation 3.10 can be transformed into:

$$d\left(\frac{m_{cat}\,\tau}{C_{C_2H_2,in}\,V_R}\right) = \frac{m_{cat}\,d\tau}{C_{C_2H_2,in}\,V_R} = \frac{dX_{C_2H_2}}{-R_{C_2H_2}} \tag{3.11}$$

which becomes, after rearranging:

$$\frac{dX_{C_2H_2}}{d\tau} = \frac{m_{cat}\,(-R_{C_2H_2})}{C_{C_2H_2,in}\,V_R} \tag{3.12}$$

For this system, a modified residence time was calculated according to equation 3.13 corresponding to the time of contact of acetylene on the catalyst as a function of the catalytic mass and of the volumetric flow of acetylene:

$$\tau' = \tau\frac{m_{cat}}{V_R} = \frac{V_R}{Q_T}\frac{m_{cat}}{V_R} = \frac{m_{cat}}{Q_T} \tag{3.13}$$

Combining equations 3.13 and 3.12:

$$\frac{dX_{C_2H_2}}{d\tau'} = \frac{-R_{C_2H_2}}{C_{C_2H_2,in}} \tag{3.14}$$

The final equation for the reaction rate was calculated as the ratio between the difference of the acetylene concentration and the time of contact of the gas in the reactor:

$$-R_{C_2H_2} = \frac{C_{C_2H_2,in} - C_{C_2H_2,out}}{\tau'} \tag{3.15}$$

3.5 Characterization techniques

Atomic Absorption Spectroscopy (AAS)

To determine the concentration of precious metal on a catalyst, the catalyst was dissolved in aqua regia and the sample was analyzed by atomic absorption spectroscopy with a Shimadzu AA-6650 spectrometer and an air-acetylene flame. The specific wavelength used for $Pd^{2+}$was 475 nm.

Attenuated Total Reflection (ATR-IR)

In order to perform the infrared spectroscopy experiments, a homemade ATR high-pressure stainless steel (316 L) cell was equipped with an internal reflection element made of Ge crystal (angle of incidence 60 °; 6 active reflections). A PTFE ring was used as sealing between the multiple reflection crystal and the cell to avoid leaks. Spectra were recorded using an EQUINOX-55 Fourier transform infrared spectrometer (Bruker Optics) purged continuously with dried air. IR spectra were recorded on the range of $4000-600$ cm^{-1} with a resolution of 2 cm^{-1} using a liquid N_2-cooled mercury cadmium telluride (MCT) detector.

Nuclear Magnetic Resonance (NMR)

NMR spectra were recorded on either an Avance 400 MHz or a 400 MHz Bruker DRX instrument with ^1H chemical shifts referenced to residual solvent peaks. The ^1H NMR spectrum was fitted with WINNMR and NMRICMA2.8/MATALAB programs (nonlinear least squares fit, minimizing the difference between the measured and calculated spectra

to determine the spectral parameters and integrals).

Scanning Electron Microscopy (SEM)

Morphological studies of the catalysts were performed by high-resolution scanning electron microscopy with a FEI XL30 SFEG microscope equipped with a True Lens Detector (TLD) detector. The acceleration voltage was varied between 10 and 20 kV and the working distance was kept between 4 and 6 mm.

Transmission Electron Microscopy (TEM)

Transmission electron microscopy was used to study size and structure of unsupported Pd nanoparticles. The microscope used was a CM20 FEG (Philips) operated at 200 kV. High-resolution images were recorded with a CM300 FEG (Philips/FEI) microscope operated at 300 kV. The solution containing the nanoparticles was cast dropped on TEM Cu grids and dried in air under infrared light for at least an hour before introducing them into the microscope.

X-Ray Diffraction (XRD)

Powder X-ray diffractograms were recorded on a Bruker/Siemens D500 incident X-ray diffractometer using Cu Kα radiation. The samples were scanned at a rate of 0.02 $^\circ$ step^{-1} over the range 30 $^o \leq 2\theta \leq$ 90 ^{o} (scan time = 5 s step^{-1}). Diffractograms were identified using the JCPDS-ICDD reference standard for Pd (46-1043).

X-Ray Photoelectron Spectroscopy (XPS)

X-ray photoelectron spectroscopy data were collected by an Axis Ultra instrument (Kratos analytical, Manchester, UK) under ultra-high vacuum condition ($<10^{-8}$ Torr) and using a monochromatic Al Kα X-ray source (1486.6 eV). The source power was maintained at 150 W and the emitted photoelectrons were sampled from a square area of 750$\times$350 μm^2.

The photoelectron take-off angle, between the surface and the direction in which the photoelectrons were analyzed, was 90 °. The analyzer pass energy was 80 eV for survey spectra (0 - 1000 eV) and 40 eV for high resolution spectra. The adventitious carbon 1*s* peak was calibrated at 284.5 eV and used as an internal standard to compensate for any charging effects. Both curve fitting of the spectra and quantification were performed with the CasaXPS software, using relative sensitivity factors given by Kratos.

Part II

Results and Discussion

Chapter 4

Size and shape-tailored Pd nanoparticles for structure sensitivity studies

In this chapter, well-defined Poly (vinyl pyrrolidone) (PVP)-stabilized cubic, octahedral and cube-octahedral Pd nanoparticles were synthesized and tested in the hydrogenation of 2-methyl-3-butyn-2-ol (MBY). Kinetic modeling based on a two-site Langmuir-Hinshelwood mechanism was consistent with the observed experimental data and allowed catalyst optimization based on a dual selectivity-activity criterion. This study is an attempt to close the *material* and *pressure gaps* between model single crystal surfaces, tested under ultra high vacuum conditions, and real catalytic systems.

This chapter is based on the following publication:

M. Crespo-Quesada, A. Yarulin, M. Jin, Y. Xia, and L. Kiwi-Minsker. The Structure Sensitivity of Alkynol Hydrogenation on Shape- and Size-Controlled Pd Nanocrystals: Which Sites Are Most Active and Selective? *Journal of the American Chemical Society*, 133(32):12787-12794, 2011.

4.1 Introduction

4.1.1 Context

Many recent studies have been carried out to investigate the catalytic behaviors of different crystal planes on model catalysts [28–30]. Most of these studies were performed in ultra-high vacuum using single metal crystals exhibiting definite crystallographic planes. However, these model catalysts are far away from the real catalytic systems. These *material* and *pressure* gaps are believed to be overcome using stable nanostructures with desirable crystallographic orientations such as nanowires [181], cubes [182], tetrahedra [40, 41], and cubo-octahedra [61, 128]. These nanoparticles with well-defined shapes can be used as-prepared as catalysts to explore the facet sensitivity of liquid-phase reactions. Recent reviews gather the results of the catalytic behavior of colloidal nanoparticles in cross-coupling, electron transfer, hydrogenation and oxidation reactions [4,5,31,32].

Among structure-sensitive reactions, Pd-catalyzed alkyne hydrogenations are of special interest due to their importance in bulk and fine chemical production. The size effect for this type of reaction was first reported by Boitiaux and co-workers [183]. Recently, it was shown that the dependence of TOF on the particle size disappeared when only one type of surface atom, namely Pd_{111}, was taken into account [11,33], suggesting that these atoms were the active sites involved in the catalysis. Using this approach, atoms located on Pd_{111} have been identified as the active sites in the hydrogenation of 1,3-butadiene and 2-methyl-3-butyn-2-ol (MBY) [44, 48]. However, the nanoparticles used in these size-dependence studies only presented a very low percentage of Pd_{100} atoms on the surface [29,30,44,48,49,184], implying that their influence, although measurable, might be easily overlooked. Furthermore, the existence of two or more different kinds of active sites responsible for observed size effects has not been thoroughly discussed in the literature [17].

In this chapter, poly(vinyl pyrrolidone) (PVP)-stabilized Pd nanoparticles with well-defined shapes were synthesized and tested per se (without any catalytic support) in the

water-assisted selective hydrogenation of MBY in order to compare the activity and selectivity of plane surface atoms, namely Pd_{100} and Pd_{111}, with edge surface atoms, Pd_{edge}. Specifically, we examined Pd nanocubes of two different sizes (6 nm and 18 nm in edge length), Pd octahedra of 31 nm in edge length, and Pd cubo-octahedra of 5.5 nm in size. A simple model involving two different types of active site was used to successfully describe the differences observed in activity and selectivity between the samples. The kinetic modeling was performed using a two-site Langmuir-Hinshelwood mechanism, with one single set of kinetic and adsorption constants specific to the reaction path or adsorption equilibrium of a compound on a given active site. The results of modeling were consistent with our observations, which, in turn, allowed optimizing the Pd catalyst's size and shape.

4.1.2 Experimental details

Catalyst preparation

The shape-tailored PVP-stabilized nanoparticles were prepared following the procedures presented in Section 3.1.1.

Their catalytic behavior was assessed with the as prepared nanoparticles in colloidal form.

Catalyst characterization

Pd concentration was determined by AAS. Surface characterization of the nanoparticles was performed with XPS. The morphology of the nanoparticles was examined with TEM and HRTEM imaging. Detailed descriptions of the apparatus used and conditions applied to perform all these analyses can be found in Section 3.5.

Hydrogenation experiments

MBY hydrogenation reactions were carried out in the baffled semi-batch stainless steel reactor described in Section 3.4.1. The 8-blade disk turbine impeller was used as stirrer. The nanoparticles, together with the reactant, were diluted in water up to 200 mL and sonicated for five minutes before introducing them in the reactor. The detailed experimental procedure can be found in the aforementioned section.

4.2 Nanoparticle characterization

4.2.1 Morphology

We synthesized Pd nanocubes, octahedra, and cuboctahedra to investigate the effect of shape on catalytic properties. We also prepared Pd nanocubes with two different sizes using a bromide-assisted method described previously (Figures 4.1A and B) [36]. Figure 4.1 shows TEM images of the Pd nanoparticles, where the Pd octahedra were obtained by reducing a Pd precursor with CH_3CHO in the presence of the 18 nm Pd nanocubes as seeds (Figure 4.1C) and the Pd cuboctahedra were synthesized by reducing a Pd precursor with L-ascorbic acid in the presence of PVP (Figure 4.1D). HRTEM imaging of each sample showed the nanoparticles to be monocrystalline and bounded by the expected crystallographic planes as seen in Figure 4.2. Furthermore, particle counting allowed determining the average particle size of each sample in which more than 95% of the nanoparticles corresponded to the expected shapes (Figure 4.3).

Despite the extensive cleaning procedures to which the nanoparticles are subjected, it is common to find traces of the stabilizing agent in the samples, which can modify the behavior of the catalyst [128, 185, 186]. Therefore, during this study, all samples were prepared with the same stabilizer, namely PVP. XPS analyses did not detect Br^- or Cl^- on the surface of the nanoparticles after cleaning, as shown in Figure 4.4 for CUB6 as

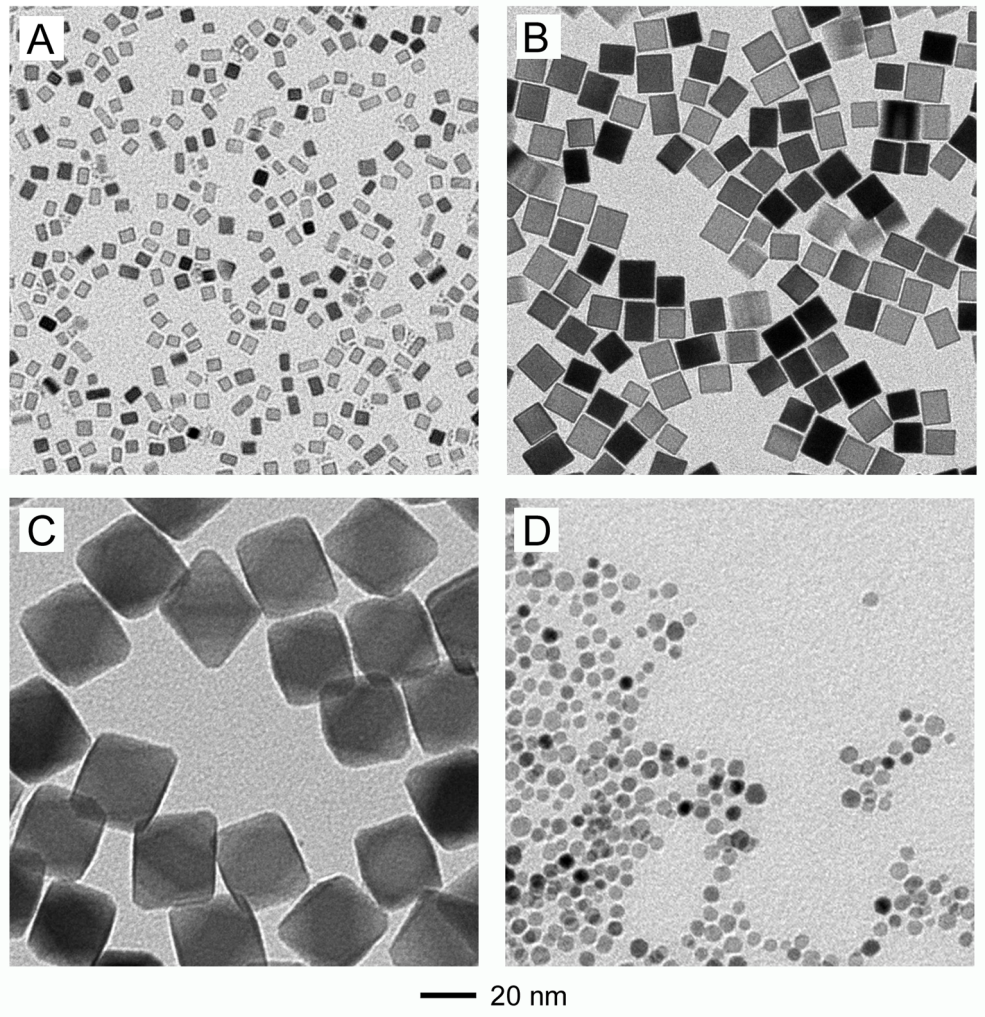

Figure 4.1: TEM images of the PVP-stabilized Pd nanoparticles used in this work. A) 6 nm cubes, B) 18 nm cubes, C) 31 nm octahedra, and D) 5.5 nm cubo-octahedra.

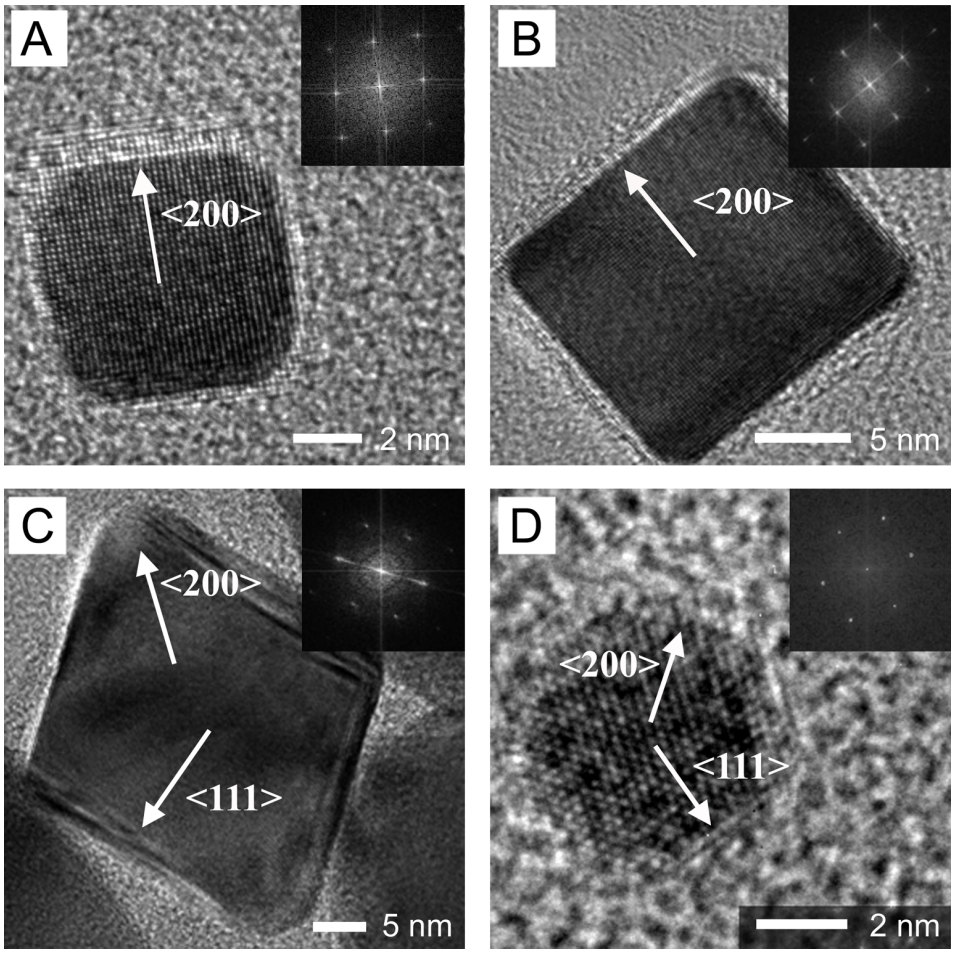

Figure 4.2: HRTEM images of the nanoparticles used during this study. A) CUB6, B) CUB18, C) OCT and D) COT. The inset in the figures show the FTT patterns of an individual nanoparticle where the lattice spacings can be indexed to reflections of face-centered cubic Pd as depicted in each panel.

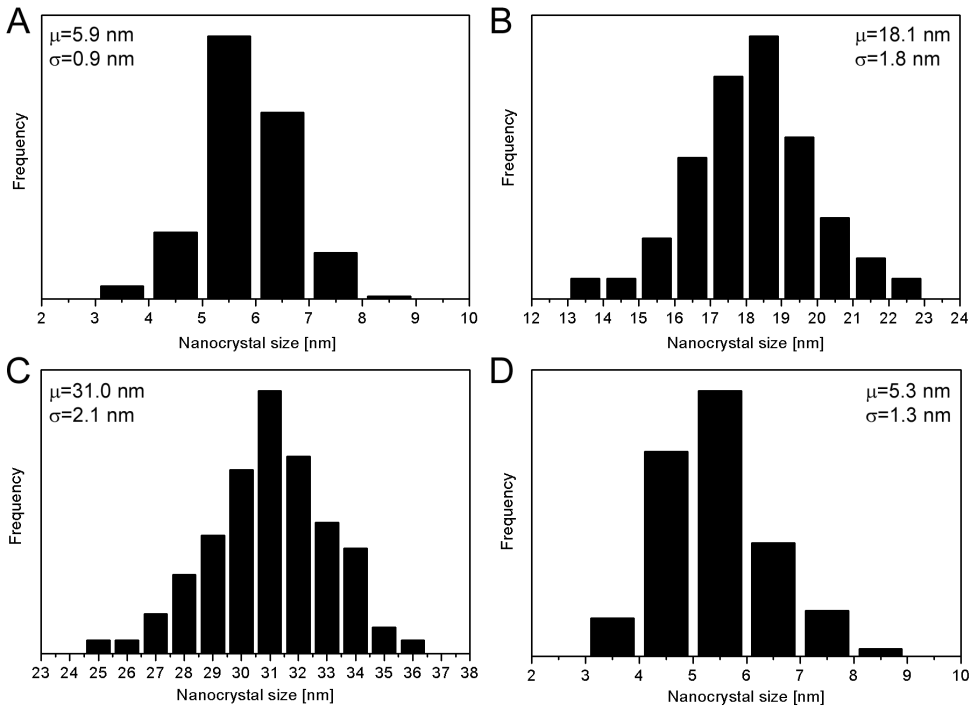

Figure 4.3: Particle size distributions of the nanoparticles used in this study. A) CUB6, B) CUB18, C) OCT and D) COT. In all samples, more than 95% of the nanoparticles presented the predominant shape.

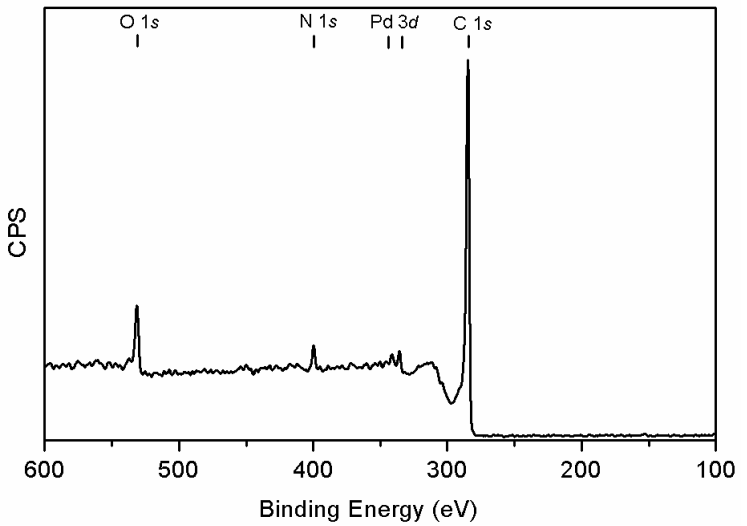

Figure 4.4: XPS survey spectrum for CUB6 sample, where only C, O, Pd and N were detected.

representative.

4.2.2 Surface statistics

The statistics of surface atoms for ideal face-centered cubic (*fcc*) nanoparticles allow one to determine the relative numbers of different types of surface atoms on a nanoparticle with a particular size and shape. Van Hardeveld and Hartog studied in the late '60's how the proportions of surface atoms differing in number and arrangement of their nearest neighbors vary with crystallite size and shape for *fcc bcc* and *hcp* structures [20].

Definitions and nomenclature

Surface atoms differ from atoms in the bulk of the crystal in that they have an incomplete set of nearest neighbors (j), i.e. their coordination number is lower than that of a generic atom in the ideal unit cell of the corresponding structure. Furthermore, the number and arrangement of the remaining nearest neighbors of a given surface atom depends on its position on the crystallite. Thus, for an *fcc* structure, such as that of metallic Pd, the

coordination number (z) of a generic bulk atom C_j^{z-j} is 12 as depicted in Figure 4.5A. This nomenclature was developed in order to differentiate surface atoms which present the same number of nearest neighbors but in a different arrangement. Therefore, for a given surface atom, its notation can be deduced as follows:

- The z atoms in the complete set of nearest neighbors are numbered as shown in Figure 4.5A.
- The upper index denote the serial numbers of the z-j missing atoms. This set of indeces can be abbreviated as long as the missing atoms are consecutive.
- In a few cases, where only one arrangement of the missing atom is possible, the upper indices are not needed and can thus be omitted.

Figure 4.5B shows the nomenclature for the different types of surface atoms found in an *fcc* cube-octahedra. In the present work and for simplicity reasons, the different types of atoms were grouped and denoted as:

- C_9^3: Pd_{111}
- $C_8^{4,5}$: Pd_{100}
- Atoms with low coordination numbers, ranging from 3 to 7: Edge atoms

Surface statistics

The total amount of atoms (N_T) constituting a crystal is made up of the number of bulk atoms (N_B) and surface atoms (N_S). In a given crystallite, N_T and N_B will be given by a polynomial of the third degree in m, where m is the number of atoms along the edge of the crystallite. N_S, on the other hand, will be given by a polynomial of the second degree in m. Analogously, the number of surface atoms (N_{111}, N_{100}, N_{edge}, etc) will be given by

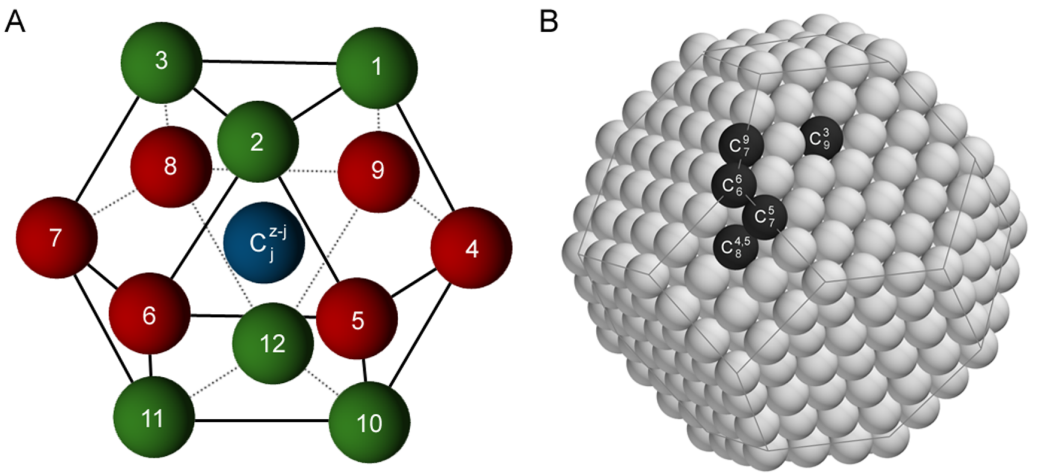

Figure 4.5: Surface statistics for an fcc nanoparticle. A) Numbering of the z nearest neighbors for atom C_j^{z-j} and B) Formal nomenclature for the surface atoms in a cube-octahedral fcc structure.

a polynomial of the zeroth, first, or second degree in m, depending on whether this type of atoms occurs on the corners, the edges or on the planes of the crystallite.

The amounts of each type of atom in *fcc* crystallites of different shapes could then be expressed as a function of nanoparticle size. For the crystallite size, the relative diameter, d_{rel}, was first estimated. This diameter is defined as the ratio of the diameter of a sphere with a volume equal to N_T times the volume occupied by an atom in the unit cell, d_{at}, which can be generalized for fcc crystallites as:

$$d_{rel} = \frac{d_{sph}}{d_{at}} = 1.105 \cdot N_T^{\frac{1}{3}} \tag{4.1}$$

from which the actual particle size can be deduced from the atomic ratio of the atom in the unit cell.

Concern has been expressed regarding the utilization of idealistic models to characterize the surface of nanoparticles [17]. Therefore, a non ideal model was chosen instead, where an incomplete extra layer of atoms lays on the surface of the nanoparticle.

In this way it is possible to estimate the surface statistics of Pd nanoparticles with

Table 4.1: Summary of the equations employed for estimating the surface statistics of some platonic *fcc* shapes [20].

	Cubes (m>4; even)	Octahedra (m>7)	Cube-octahedra (m>6)
N_T	$4m^3 - 6m^2 + 3m$	$\frac{1}{3}(2m^3 + 12m^2 - 83m + 144)$	$(16m^3 - 3m^2 - 108m + 144)$
N_S	$12m^2 - 12m - 16$	$4m^2 + 8m - 66$	$30m^2 - 24m - 66$
N_{edge}	$12(m-2) + 24(m-4) + 8$	$12(3m - 14) + 6$	$24(3m - 10) + 12(3m - 10) + 24$
N_{111}	-	$4(m-7)(m-6)$	$24(m-3)^2$
N_{100}	$6(m-2)^2 + 6(m-4)^2$	-	$6(m-5)^2$

Table 4.2: Surface statistics of the catalysts used in this study.

Sample	d_p [nm]	D [%]	x_{111} [%]	x_{100} [%]	x_{edge} [%]
CUB6	6	16.7	-	72.1	15.8
CUB18	18	6.0	-	90.0	6.0
OCT	31	3.6	93.2	-	5.5
COT	5.5	18.3	43.7	5.6	30.3

different platonic shapes (cubes, octahedra and cube-octahedra). The equations used to estimate the number of each type of atom can be found in Table 4.1 and the corresponding graphical representation of the variation of each type of atom with nanoparticle size can be seen in Figure 4.6.

4.3 Structure sensitivity of MBY hydrogenation

4.3.1 Catalytic behavior

The approach presented in Section 4.2.2 can be used to estimate the surface statistics of the nanoparticles used in this work. Table 4.2 gathers this information.

The reaction network for MBY hydrogenation is depicted in Figure 2.5 [44, 48, 73, 74]. MBY can be either semi-hydrogenated to 2-methyl-3-buten-2-ol (MBE) through path a, directly hydrogenated to 2-methyl-3-butan-2-ol (MBA) through path c or oligomerized into C-10 species through path d. Furthermore, MBE can be over-hydrogenated to MBA

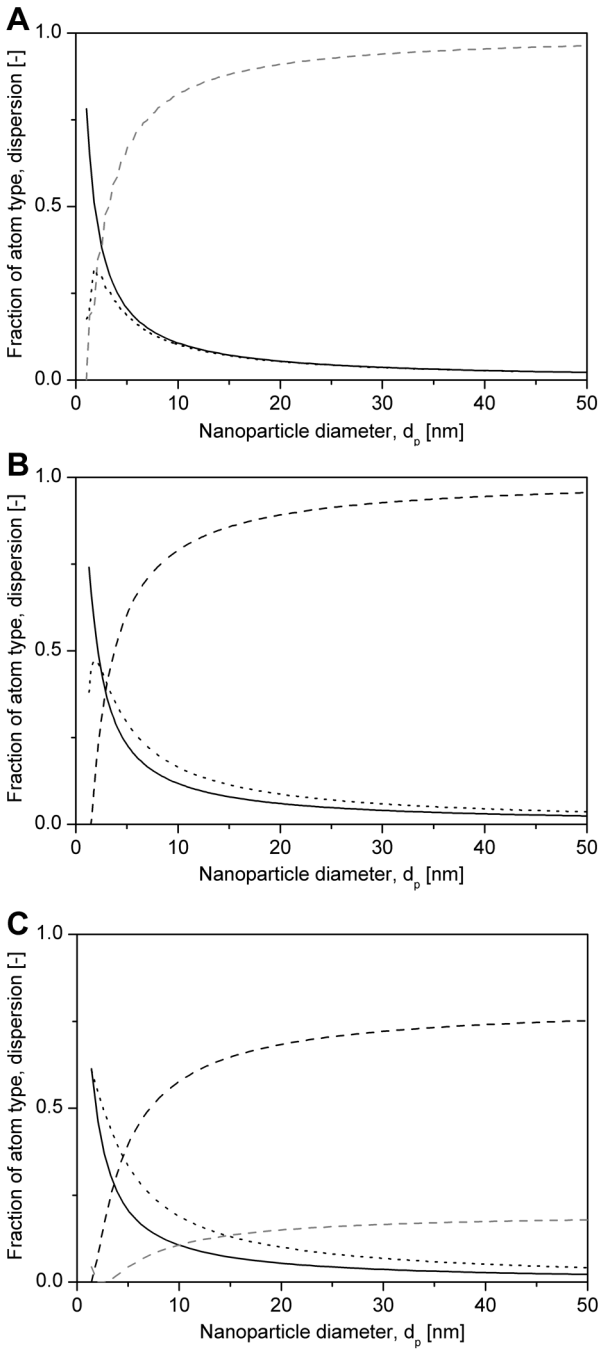

Figure 4.6: Dispersion (bold line), Pd_{111} fraction (black dashed line), Pd_{100} fraction (gray dashed line) and low-coordination (edge) atoms fraction (dotted line) as a function of the diameter for A) cubic, B) octahedral and C) cube-octahedral *fcc* nanoparticles.

through path b. In this work path d was not observed, and was thus eliminated from the network for simplicity. In our previous study [44], the hydrogenation of MBY showed an antipathetic structure-sensitivity, suggesting at a first glance that only plane surface atoms were responsible for the catalytic activity of Pd nanoparticles, since their relative amount increases with particle size (Figure 4.6).

The Pd nanoparticles shown in Figure 4.1 were tested as unsupported catalysts for the water-assisted hydrogenation of MBY. In order to confirm the morphological stability of the nanoparticles throughout the reaction, cubic nanoparticles were subjected to the reaction conditions for 2.5 h and were observed with TEM immediately after. The nanoparticles maintained their shape (Figure 4.7) and, being the least favorable shape, the result could be extrapolated to the other shapes.

All nanoparticles were active, thus confirming that Pd_{100} present on cubes could indeed catalyze the hydrogenation of MBY. The values for MBY transformation rate and TOF are summarized in Table 4.3. In order to evaluate the specific activities of the various types of surface atoms, two models describing the observed TOF were applied. The first activity model (A) is based on the assumption that the observed activity (TOF_{obs}) depends linearly on the fraction of each atom type (x_i) and their specific activity (TOF_i):

$$TOF_{obs} = TOF_{111} \cdot x_{111} + TOF_{100} \cdot x_{100} \tag{4.2}$$

Edge atoms were considered to be inactive, following the results published in literature [11, 29, 30, 33, 44, 48]. As a result, the observed size and/or shape dependence of the nanoparticles would actually be due to the change of the relative amount of surface atoms.

Model A was first applied to CUB18 and OCT, the two samples with the highest fraction of plane atoms. Equation 4.2, together with the statistics of surface atoms from Table 4.2, was used to estimate TOF_{111} and TOF_{100}. From these calculations, Pd_{100} and Pd_{111} plane atoms were found to be almost equally active in MBY hydrogenation. The

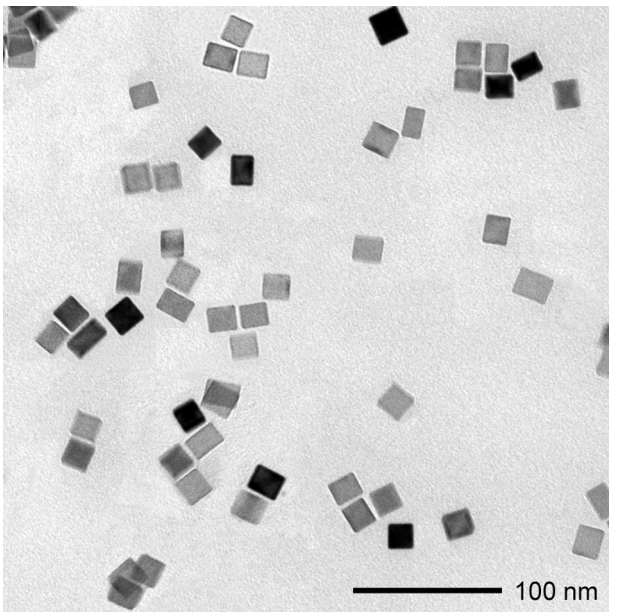

Figure 4.7: TEM image of cubic nanoparticles after a 2.5 h catalytic run, after which the morphology was well maintained.

model was, however, unable to predict the observed values of TOF for CUB6 and COT. These results, together with the fact that CUB6 and COT samples present 15% and 30% of low-coordination (edge) atoms on their surfaces, suggest that a model including the latter would be able to describe the system more accurately. Since $Pd_{(100)}$ and $Pd_{(111)}$ plane atoms were found to show a similar activity, then model B was suggested as follows:

$$TOF_{obs} = TOF_{plane} \cdot x_{plane} + TOF_{edge} \cdot x_{edge} \tag{4.3}$$

The application of this model (Table 4.3) simultaneously on all four samples allowed the estimation of the specific plane and edge TOFs, which were found to be 19.3±2.4 s^{-1} and 4.7±0.8 s^{-1}, respectively, suggesting that MBY adsorbs on all types of surface atoms, but its reactivity depends on the coordination number of the active site. Indeed, strong adsorption strengths of the electron rich alkyne on low-coordination atoms, such as edge atoms, led to a decrease in activity in the hydrogenation of 1-butyne [49,50]. It is worth noting that this model still accounts for the antipathetic structure sensitivity shown by

Table 4.3: Activity models A and B as applied to the catalytic responses of differently shaped Pd nanoparticles to account for the structure-sensitivity of the reaction.[a]

Sample	R_Y^b	TOF_{obs}	Model A			Model B	
			TOF_{111}	TOF_{100}	TOF_{est}	TOF_{plane}	TOF_{edge}
		$[s^{-1}]$	$[s^{-1}]$	$[s^{-1}]$	$[s^{-1}]$	$[s^{-1}]$	$[s^{-1}]$
CUB6	2.55	15.3	-	19.2	13.8	19.3 ± 2.4	4.7 ± 0.8
CUB18	1.05	17.5	-	19.2	17.5	19.3 ± 2.4	4.7 ± 0.8
OCT	0.53	14.6	15.6	-	14.6	19.3 ± 2.4	4.7 ± 0.8
COT	2.25	12.3	15.6	19.2	9.3	19.3 ± 2.4	4.7 ± 0.8

[a]Reaction conditions: 1 g of MBY, MBY:Pd_{surf}=140000, 200 mL of H_2O, 333 K, 0.3 MPa of H_2.
[b]Transformation rate of MBY: $\left[\text{mol} \cdot \text{mol}_{\text{Pd}}^{-1} \cdot \text{s}^{-1}\right]$

MBY hydrogenation, since an increase in size will still imply an increase in TOF.

Selectivity towards the target product, MBE, also pointed towards the existence of two types of active sites, namely plane and edge atoms. Figure 4.8 shows the selectivity of each sample as a function of amount of edge atoms on their surfaces. It can be appreciated that at 50% conversion it is independent of both the size and shape of the nanoparticle. This is in line with the thermodynamic selectivity shown in alkyne hydrogenations; as long as the coverage of the alkyne is still high enough, it will "block" the active sites due to it higher adsorption strength as compared to the olefinic compound [51]. This implies that both plane and edge sites selectively hydrogenate towards MBE, only that the latter does so at 20% the rate of the former.

When approaching full conversion, however, there seems to be a clear correlation between over-hydrogenation and amount of edge atoms (Figure 4.8). For a given metal, the adsorption strength of the substrate varies in the same order aromatic<olefin<diolefin<alkyne. A plot depicting the activity of the metal as a function of the adsorption strength gives thus rise to a characteristic "volcano" curve (Figure 4.9), with the maximum located between olefins and diolefins [51].

This implies that an increase in the adsorption strength of the alkyne, such as adsorb-

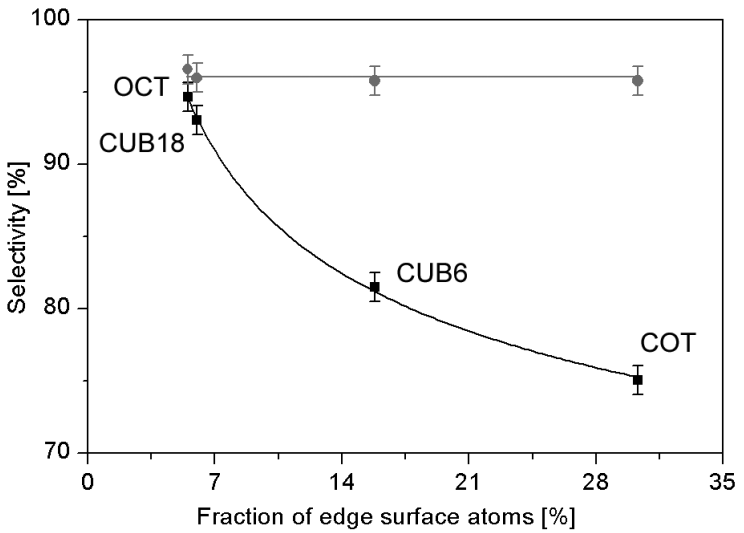

Figure 4.8: Selectivity towards MBE at ● 50% and ■ 95% conversion.

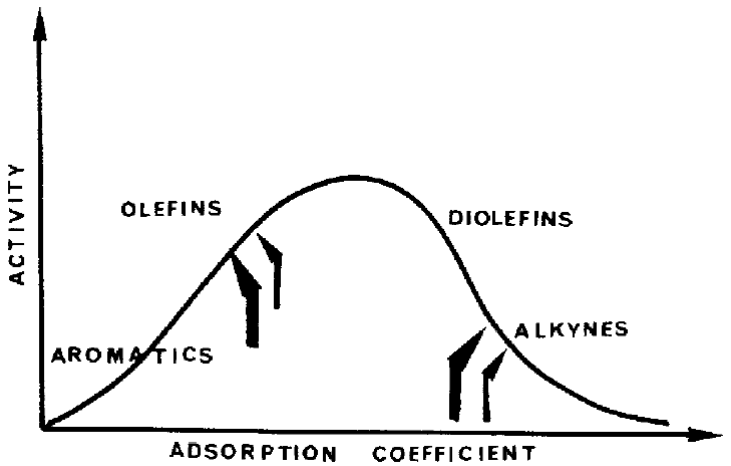

Figure 4.9: Schematic graph of activity in hydrogenation reaction as a function of adsorption coefficient on large nanoparticles (bold arrow) and on small nanoparticles (thin arrow) [51].

ing on an edge atom rather than a plane atom, would decrease the activity, whereas the opposite would be observed for the olefin. Therefore, when the coverage of MBY is insufficient to ensure the blocking of all active sites, MBE can thus adsorb and over-hydrogenate towards MBA. The rate of over-hydrogenation of MBE should then be higher on edge sites than on plane sites. This can indeed be observed on the high selectivities at 95% conversion found on CUB18 and OCT samples, which contain very few edge sites. It has also been found that at high dispersions, i.e. small particle size, 1-butene hydrogenation was fast, whereas the hydrogenation of 1-butyne decreased sharply [50]. Furthermore, edge sites were recently suggested as active sites for the hydrogenation of MBE over Pd [187].

Figure 4.10A shows a schematic representation of the active sites present on each nanoparticle shape used in this work; Pd_{100} and Pd_{111} plane atoms were considered as a single site, σ_1. Edge atoms were considered as a separate type of active site, σ_2. The reaction network for MBY hydrogenation shown in Figure 2.5, can then be modified to include the observations gathered experimentally, presented in Figure 4.10B. The semi-hydrogenation of MBY proceeds through both σ_1 and σ_2 sites. The direct over-hydrogenation of MBY to MBA, observed since the beginning of the reaction, takes place exclusively on σ_1 sites. The over-hydrogenation of MBE to MBA, on the other hand, is catalyzed solely by σ_2 sites. Equation 4.3 could be then rewritten as:

$$TOF_{obs} = TOF_{\sigma_1} \cdot x_{\sigma_1} + TOF_{\sigma_2} \cdot x_{\sigma_2} \tag{4.4}$$

4.3.2 Kinetic modelling

In order to model the reaction kinetics, a Langmuir-Hinshelwood mechanism assuming two types of active sites as well as dissociative hydrogen adsorption [188] and bimolecular reactions between the adsorbed species was applied. The series of elementary steps comprising

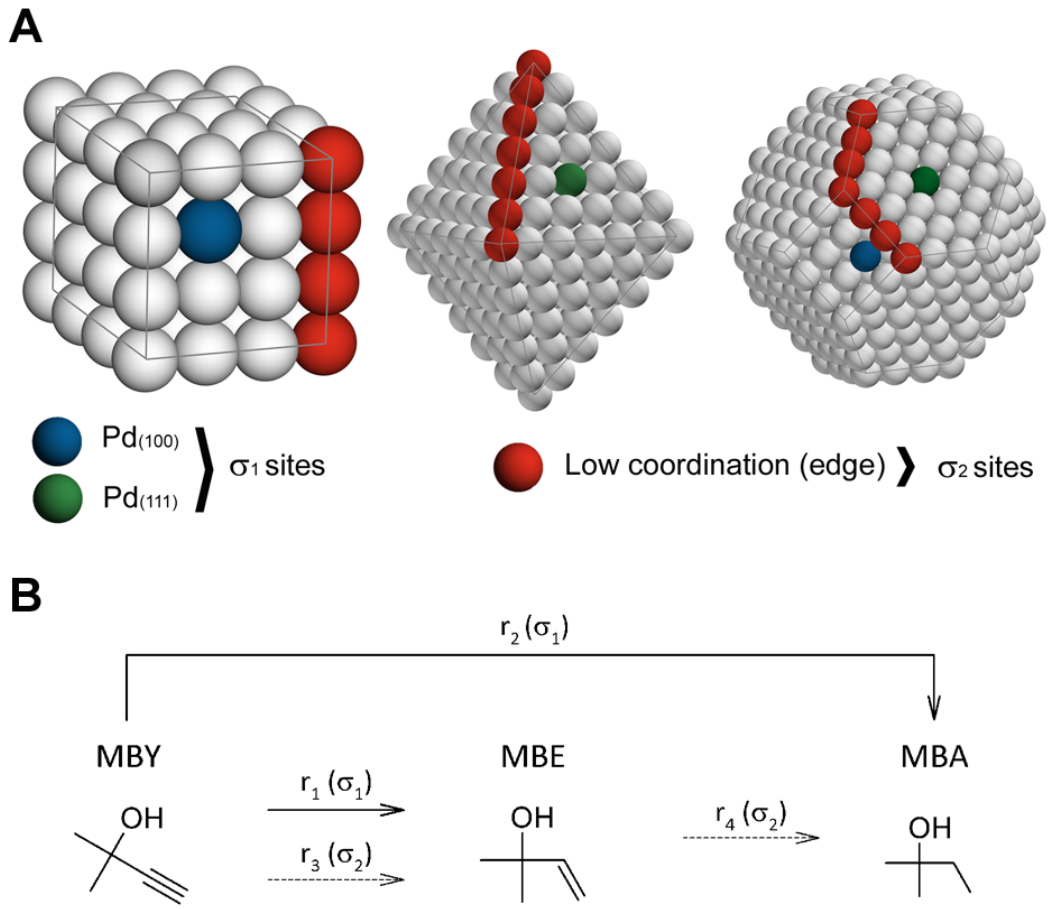

Figure 4.10: A) Schematic illustrations of the two types of active sites involved in the hydrogenation of 2-methyl-3-butyn-2-ol (MBY). Atoms on the planes, regardless of their crystallographic orientations, constitute the first type of active site, σ_1. Low-coordination atoms, or atoms at the edges, represent the second type of active site, σ_2 and B) Modified reaction network for the hydrogenation of 2-methyl-3-butyn-2-ol (MBY), showing the active sites involved in each path.

the reaction network presented in Figure 4.10 is listed in Table 4.4. The kinetic constant, or reaction rate expression of each step is also included.

A surface balance of active sites must be performed in order to express site vacancies in terms of measurable parameters. The coverage of the intermediate species was neglected:

$$\theta_{\sigma_1} = \theta_{Y,\sigma_1} + \theta_{E,\sigma_1} + \theta_{A,\sigma_1} + \theta_{H_2,\sigma_1} \tag{4.5}$$

$$\theta_{\sigma_2} = \theta_{Y,\sigma_2} + \theta_{E,\sigma_2} + \theta_{A,\sigma_2} + \theta_{H_2,\sigma_2} \tag{4.6}$$

If coverages are expressed in terms of adsorption constants and bulk concentrations (obtained from Table 4.4):

$$\theta_{\sigma_1} = \frac{1}{1 + K_{Y,\sigma_1}C_Y + K_{E,\sigma_1}C_E + K_{A,\sigma_1}C_A + \sqrt{K_{H_2,\sigma_1}C_{H_2}}} \tag{4.7}$$

$$\theta_{\sigma_2} = \frac{1}{1 + K_{Y,\sigma_2}C_Y + K_{E,\sigma_2}C_E + K_{A,\sigma_2}C_A + \sqrt{K_{H_2,\sigma_2}C_{H_2}}} \tag{4.8}$$

Thus, the reaction rate expressions for all four paths of the mechanism can be developed and are presented below.

$$r_1 = \frac{k_{1,\sigma_1}K^*_{Y,\sigma_1} \cdot K_{H_2,\sigma_1}C_{H_2} \cdot K_{Y,\sigma_1}C_Y}{\left(1 + K_{Y,\sigma_1}C_Y + K_{E,\sigma_1}C_E + K_{A,\sigma_1}C_A + \sqrt{K_{H_2,\sigma_1}C_{H_2}}\right)^2} \tag{4.9}$$

$$r_2 = \frac{k_{2,\sigma_1}K^{***}_{Y,\sigma_1} \cdot K^{**}_{Y,\sigma_1} \cdot K^*_{Y,\sigma_1} \cdot K^2_{H_2,\sigma_1}C^2_{H_2} \cdot K_{Y,\sigma_1}C_Y}{\left(1 + K_{Y,\sigma_1}C_Y + K_{E,\sigma_1}C_E + K_{A,\sigma_1}C_A + \sqrt{K_{H_2,\sigma_1}C_{H_2}}\right)^2} \tag{4.10}$$

$$r_3 = \frac{k_{3,\sigma_2}K^*_{Y,\sigma_2} \cdot K_{H_2,\sigma_2}C_{H_2} \cdot K_{Y,\sigma_2}C_Y}{\left(1 + K_{Y,\sigma_2}C_Y + K_{E,\sigma_2}C_E + K_{A,\sigma_2}C_A + \sqrt{K_{H_2,\sigma_2}C_{H_2}}\right)^2} \tag{4.11}$$

Table 4.4: Langmuir-Hinshelwood mechanism for the hydrogenation of MBY assuming two types of active sites.

Reaction path	Site		Step	Kinetic expression
		1	$Y + \sigma_1 \longleftrightarrow Y\sigma_1$	$K_{Y,\sigma_1} = \frac{\theta_{Y,\sigma_1}}{C_Y \theta_{\sigma_1}}$
1		2	$H_2 + 2\sigma_1 \longleftrightarrow 2\,(H\sigma_1)$	$K_{H_2,\sigma_1} = \frac{\theta^2_{H_2,\sigma_1}}{C_{H_2} \theta^2_{\sigma_1}}$
MBY $\rightarrow$ MBE	σ_1	3	$Y\sigma_1 + H\sigma_1 \longleftrightarrow Y^*\sigma_1 + \sigma_1$	$K^*_{Y,\sigma_1} = \frac{\theta_{Y^*,\sigma_1}\theta_{\sigma_1}}{\theta_{Y,\sigma_1}\theta_{H,\sigma_1}}$
(Y $\rightarrow$ E)		4*	$Y^*\sigma_1 + H\sigma_1 \longrightarrow E\sigma_1 + \sigma_1$	$r_1 = k_{1,\sigma_1}\theta_{Y^*,\sigma_1}\theta_{H,\sigma_1}$
		5	$E\sigma_1 \longleftrightarrow E + \sigma_1$	$K_{E,\sigma_1} = \frac{\theta_{E,\sigma_1}}{C_E \theta_{\sigma_1}}$
2		1	$Y^*\sigma_1 + H\sigma_1 \longleftrightarrow Y^{**}\sigma_1 + \sigma_1$	$K^{**}_{Y,\sigma_1} = \frac{\theta_{Y^{**},\sigma_1}\theta_{\sigma_1}}{\theta_{Y^*,\sigma_1}\theta_{H,\sigma_1}}$
MBY $\rightarrow$ MBA	σ_1	2	$Y^{**}\sigma_1 + H\sigma_1 \longleftrightarrow Y^{***}\sigma_1 + \sigma_1$	$K^{***}_{Y,\sigma_1} = \frac{\theta_{Y^{***},\sigma_1}\theta_{\sigma_1}}{\theta_{Y^{**},\sigma_1}\theta_{H,\sigma_1}}$
(Y $\rightarrow$ A)		3*	$Y^{***}\sigma_1 + H\sigma_1 \longrightarrow A\sigma_1 + \sigma_1$	$r_2 = k_{2,\sigma_1}\theta_{Y^{***},\sigma_1}\theta_{H,\sigma_1}$
		4	$A\sigma_1 \longleftrightarrow A + \sigma_1$	$K_{A,\sigma_1} = \frac{\theta_{A,\sigma_1}}{C_A \theta_{\sigma_1}}$
		1	$Y + \sigma_2 \longleftrightarrow Y\sigma_2$	$K_{Y,\sigma_2} = \frac{\theta_{Y,\sigma_2}}{C_Y \theta_{\sigma_2}}$
3		2	$H_2 + 2\sigma_2 \longleftrightarrow 2\,(H\sigma_2)$	$K_{H_2,\sigma_2} = \frac{\theta^2_{H_2,\sigma_2}}{C_{H_2} \theta^2_{\sigma_2}}$
MBY $\rightarrow$ MBE	σ_2	3	$Y\sigma_2 + H\sigma_2 \longleftrightarrow Y^*\sigma_2 + \sigma_2$	$K^*_{Y,\sigma_2} = \frac{\theta_{Y^*,\sigma_2}\theta_{\sigma_2}}{\theta_{Y,\sigma_2}\theta_{H,\sigma_2}}$
(Y $\rightarrow$ E)		4*	$Y^*\sigma_2 + H\sigma_2 \longrightarrow E\sigma_2 + \sigma_2$	$r_3 = k_{3,\sigma_2}\theta_{Y^*,\sigma_2}\theta_{H,\sigma_2}$
		5	$E\sigma_2 \longleftrightarrow E + \sigma_2$	$K_{E,\sigma_2} = \frac{\theta_{E,\sigma_2}}{C_E \theta_{\sigma_2}}$
4		1	$E\sigma_2 + H\sigma_2 \longleftrightarrow E^*\sigma_2 + \sigma_2$	$K^*_{E,\sigma_2} = \frac{\theta_{E^*,\sigma_2}\theta_{\sigma_2}}{\theta_{E,\sigma_2}\theta_{H,\sigma_2}}$
MBE $\rightarrow$ MBA	σ_2	2*	$E^*\sigma_2 + H\sigma_2 \longrightarrow A\sigma_2 + \sigma_2$	$r_4 = k_{4,\sigma_2}\theta_{E^*,\sigma_2}\theta_{H,\sigma_2}$
(E $\rightarrow$ A)		3	$A\sigma_2 \longleftrightarrow A + \sigma_2$	$K_{A,\sigma_2} = \frac{\theta_{A,\sigma_2}}{C_A \theta_{\sigma_2}}$

* Rate determining step (RDS)

$$r_4 = \frac{k_{4,\sigma_2} K^*_{E,\sigma_2} \cdot K_{H_2,\sigma_2} C_{H_2} \cdot K_{E,\sigma_2} C_E}{\left(1 + K_{Y,\sigma_2} C_Y + K_{E,\sigma_2} C_E + K_{A,\sigma_2} C_A + \sqrt{K_{H_2,\sigma_2} C_{H_2}}\right)^2} \tag{4.12}$$

Equations can be simplified by partly grouping the constants in the numerator as well as by neglecting the coverage of hydrogen [188] and alkane in the active site balance of the denominator. This diminishes the number of degrees of freedom of the system by reducing the number of adjustable parameters:

$$r_1 = \frac{k^*_{1,\sigma_1} K_{Y,\sigma_1} C_Y}{\left(1 + K_{Y,\sigma_1} C_Y + K_{E,\sigma_1} C_E\right)^2} \tag{4.13}$$

$$r_2 = \frac{k^*_{2,\sigma_1} K_{Y,\sigma_1} C_Y}{\left(1 + K_{Y,\sigma_1} C_Y + K_{E,\sigma_1} C_E\right)^2} \tag{4.14}$$

$$r_3 = \frac{k^*_{3,\sigma_2} K_{Y,\sigma_2} C_Y}{\left(1 + K_{Y,\sigma_2} C_Y + K_{E,\sigma_2} C_E\right)^2} \tag{4.15}$$

$$r_4 = \frac{k^*_{4,\sigma_2} K_{E,\sigma_2} C_E}{\left(1 + K_{Y,\sigma_2} C_Y + K_{E,\sigma_2} C_E\right)^2} \tag{4.16}$$

The mass balance for MBY, MBE and MBA are given by the following equations:

$$\frac{dC_Y}{dt} = \frac{n_{Pd}}{V}\left(-r_1 - r_2 - r_3\right) \tag{4.17}$$

$$\frac{dC_E}{dt} = \frac{n_{Pd}}{V}\left(r_1 + r_3 - r_4\right) \tag{4.18}$$

$$\frac{dC_A}{dt} = \frac{n_{Pd}}{V}\left(r_2 + r_4\right) \tag{4.19}$$

Equations 4.13-4.19 were solved simultaneously using Berkeley's Madonna [189] software with Runge-Kutta's method for differential equations. Subscripts Y, E and A refer

Table 4.5: Adsorption and kinetic constants obtained from kinetic modeling.

	Adsorption constants $[\mathrm{L\,mol^{-1}}]$				Kinetic constants $[\mathrm{mol\,mol_{Pd}^{-1}\,s^{-1}}]$			
Sample	K_{Y,σ_1}	K_{Y,σ_2}	K_{E,σ_1}	K_{E,σ_2}	k^*_{1,σ_1}	k^*_{2,σ_1}	k^*_{3,σ_2}	k^*_{4,σ_2}
CUB6					10.0	0.3	0.6	12.8
CUB18	20.5	56.5	0.2	2.7	4.8	0.2	0.1	1.8
OCT					2.1	0.06	0.03	0.6
COT					9.3	0.2	1.7	19.3

to the alkyne, alkene and alkane, respectively. The adsorption constants K_{Y,σ_1}, K_{Y,σ_2}, K_{E,σ_1} and K_{E,σ_2} were set to be equal for all samples since the main premise of the study is that the MBY molecules interact specifically with each type of site, regardless of the size or shape of the nanoparticle. The kinetic constants, however, were varied from sample to sample (Table 4.5). The quality of the fitting to the experimental points obtained was satisfactory in all cases, as it can be appreciated in Figure 4.11.

Since it was observed that activity could be correlated to the relative amounts of plane and edge sites, the model was pushed one step further by assuming that the kinetic constants should follow the same principle. They were thus rendered independent of the size and shape of the Pd nanoparticles by expressing them in terms of mols of surface atom of Pd:

$$k^{**}_{j,k} = \frac{k^*_{j,k}}{D} \left[\frac{mol}{mol_{Pd_{surf}} s} \right] \tag{4.20}$$

where the subscripts j and k correspond to reaction path and site type, respectively, and D refers to the dispersion of the nanoparticle. The constant shown in equation (4.20) is thus expressed by total amount of surface Pd atoms, but it is not yet specific to one of the two types of sites used in this work. A further normalization with respect to the fraction of each type of site is then necessary:

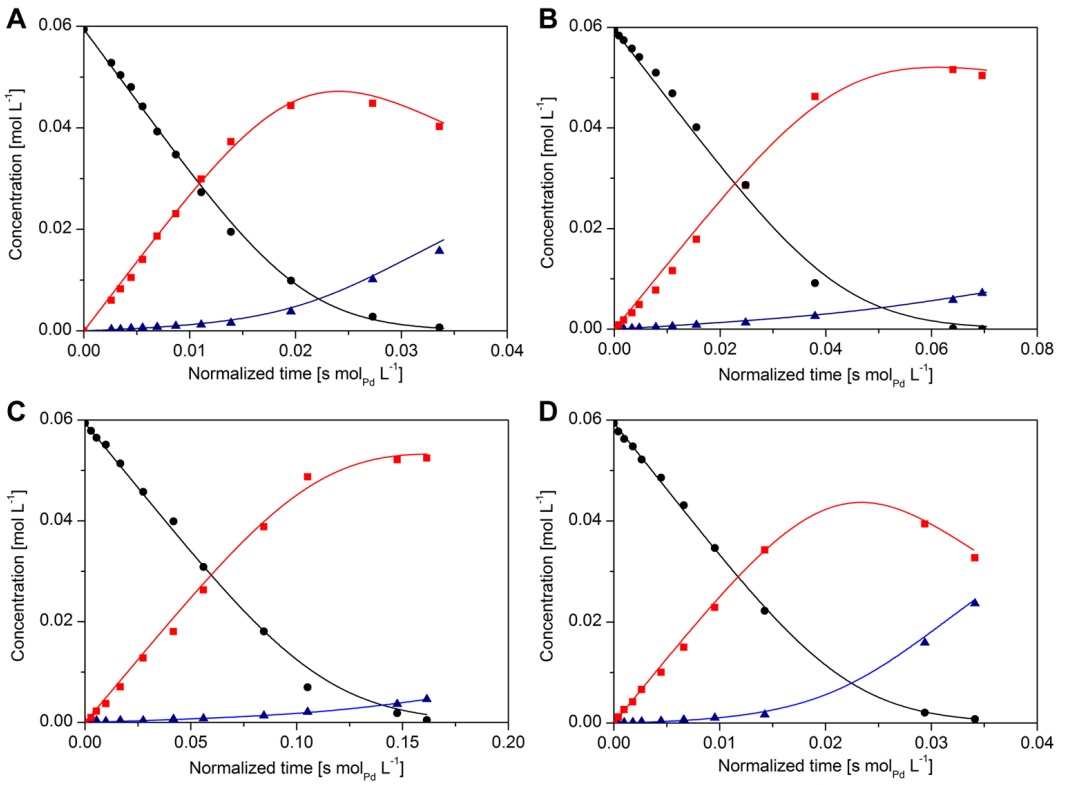

Figure 4.11: Experimental data points for 2-methyl-3-butyn-2-ol (MBY, ●), 2-methyl-3-buten-2-ol (MBE, ■), and 2-methyl-3-butan-2-ol (MBA, ▲) and the prediction curves obtained by fixing the adsorption constants and varying the kinetic constants for each run for (A) CUB6, (B) CUB18, (C) OCT, and (D) COT samples. Reaction conditions: 1 g of MBY, molMBY : Pd_{surf} = 140000, 200 mL of H_2O, 333 K, 0.3 MPa of H_2.

Table 4.6: Adsorption and kinetic constants obtained from kinetic modeling.

Adsorption constants $\left[\mathrm{L\,mol^{-1}}\right]$				Kinetic constants $\left[\mathrm{mol\,mol^{-1}_{Pd_{surf}}\,s^{-1}}\right]$			
K_{Y,σ_1}	K_{Y,σ_2}	K_{E,σ_1}	K_{E,σ_2}	k^{***}_{1,σ_1}	k^{***}_{2,σ_1}	k^{***}_{3,σ_2}	k^{***}_{4,σ_2}
20.5	56.5	0.2	2.7	83.8	2.3	24.0	428.2

$$k^{***}_{j,k} = \frac{k^{**}_{j,k}}{x_k}\left[\frac{mol}{mol_{Pd_{surf}}\,s}\right] \tag{4.21}$$

The constants obtained in this way are specific to a reaction path and active site type, but independent of the size and shape of the nanoparticles. Four specific kinetic constants were estimated and then found to satisfy all samples through equations (4.13-4.21) with errors lower than 20% (see Table 4.6). These values suggest that plane sites are 3.5 times more active in the selective hydrogenation of MBY to MBE, but that this reaction can indeed take place over the edge sites as well. Furthermore, it can be seen that the consecutive hydrogenation of MBE to MBA on edge sites is kinetically favored.

The kinetics obtained for all samples were successfully modeled using this set of constants. It can be seen (Figure 4.12) that the fitting remains accurate despite the experimental error and the simplifications made. The conjugation of equations (4.13-4.21) with the set of empirically obtained constants (Table 4.6) provides a powerful tool that allows for a full kinetic description of a Pd nanoparticle regardless of its size and shape, as long as the statistics of surface atoms can be estimated.

4.3.3 Nanoparticle size and shape optimization

Activity as optimization criterion

Size and shape optimization is often performed by only considering activity as the optimization criterion [187]. If this approach is applied, then equation (4.4) can be combined with the surface statistics for common nanoparticle shapes to yield the graph presented in

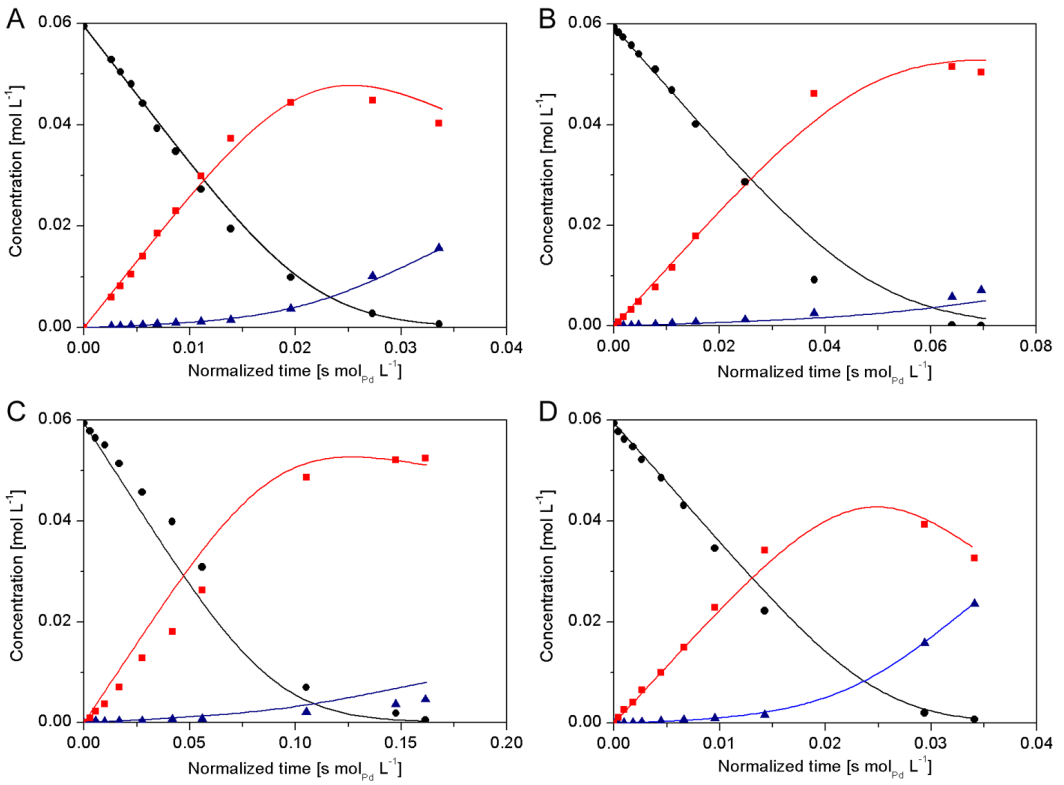

Figure 4.12: Experimental data points for 2-methyl-3-butyn-2-ol (MBY, ●), 2-methyl-3-buten-2-ol (MBE, ■), and 2-methyl-3-butan-2-ol (MBA, ▲) and the prediction curves obtained with a single set of adsorption and kinetic constants for (A) CUB6, (B) CUB18, (C) OCT, and (D) COT samples. Reaction conditions: 1 g of MBY, mol MBY : Pd_{surf} = 140000, 200 mL of H_2O, 333 K, 0.3 MPa of H_2.

Figure 4.13A.

As expected, shape does not exert a considerable effect on TOF for MBY transformation since both (111) and (100) planes behave similarly. Cubo-octahedra, however, are slightly disfavored due to the larger fraction of edge atoms (or σ_2 sites), which are considerably less active in the hydrogenation of MBY relative to plane atoms (or σ_1 sites). The most significant size effect is observed in the 3-20 nm range, after which the reaction becomes size and shape independent with respect to TOF. nanoparticles smaller than 3 nm in size start to lose their bulk properties [17, 22] and, consequently, the catalytic behavior may not follow the prediction. This region is depicted with dotted lines.

If, on the other hand, MBY transformation rate is referred to the total amount of Pd, then both size and shape effects change substantially (Figure 4.13B). While there would be no difference between cubic or octahedral nanoparticles, cubo-octahedra will be significantly less active due to their low dispersions. This difference, however, can be neglected for particles larger than 15 nm in size, after which the reaction becomes again size and shape independent. Therefore, if the activity of a catalyst is used as the only optimization criterion, either cubes or octahedra of roughly $\sim$5 nm in size should be the best choice for the catalyst.

Selectivity as optimization criterion

Selectivity is a very, if not the most, important catalytic property for most applications. Therefore, a *dual selectivity-activity* criterion for optimization seems to be well-justified. To achieve this, we had to combine equations (4.13-4.21) with the set of empirically obtained constants (Table 4.6) and the statistics of surface atoms for the nanoparticles in study presented in Section 4.2.2. This allowed simulating the kinetic curves (analogous to those shown in Figures 4.11 and 4.12) for each shape in the nanoparticle size range of 3-50 nm by changing only one parameter, namely the number of atoms along the edge of the nanoparticle (m). Selectivity could be thus estimated for a given conversion for each

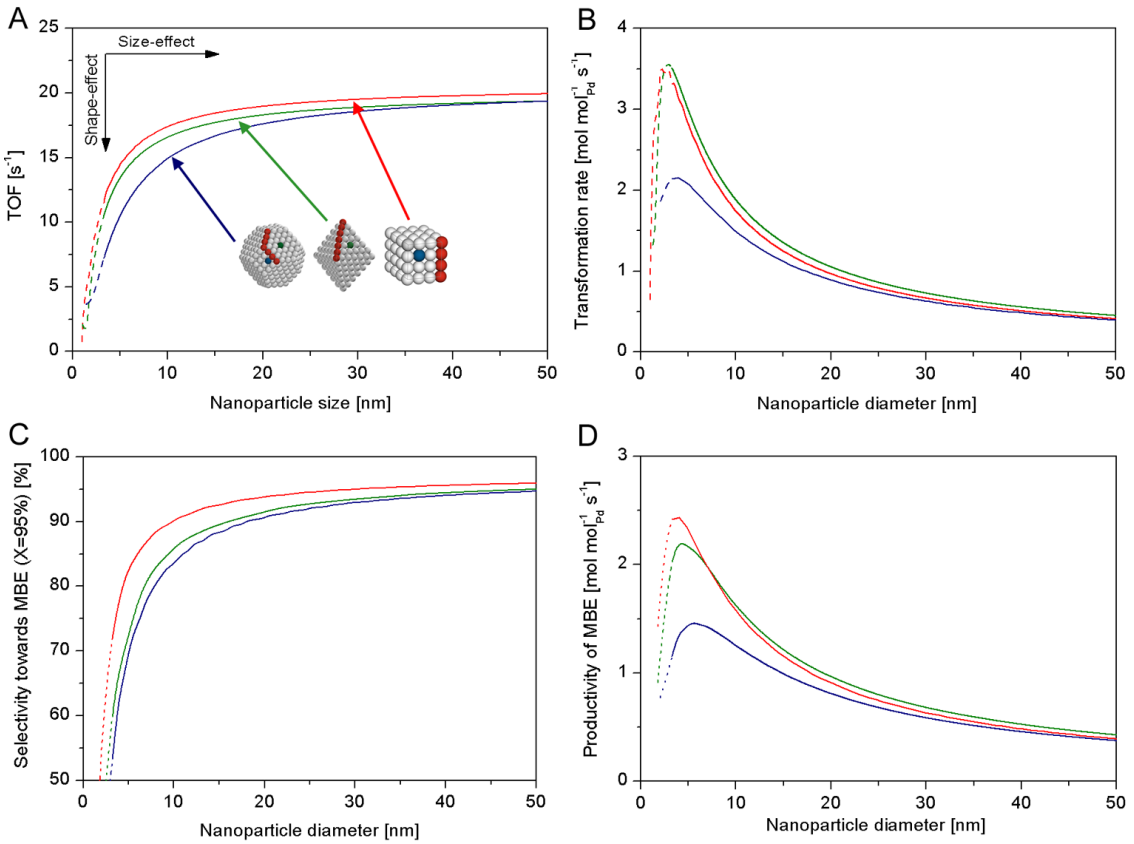

Figure 4.13: Optimization of Pd nanocrystal size and shape based on (A) TOF, (B) MBY transformation rate, (C) selectivity toward 2-methyl-3-buten-2- ol (MBE) at 95% conversion, and (D) transformation rate, or productivity, of MBE.

shape in the aforementioned size range.

$$S_E = \frac{C_E}{C_Y^0 - C_Y} \tag{4.22}$$

The program shown below was implemented on Berkeley Madonna and batch runs were performed with m as the only independent variable and corresponds to the octahedral nanoparticles. Analogous programs were written and implemented for cubic and cube-octahedral nanoparticles.

Initial conditions

$C_Y^0 = 0.05941$

$C_E^0 = 0$

$C_A^0 = 0$

$m = 20$

Surface statistics of a nanoparticle with m atoms along its edge

$d_{rel} = 1.105\, N_T^{1/3}$

$d_p = 0.2103\, d_{rel}$

$N_T = \frac{1}{3}\,(2m^3 + 12m^2 - 83m + 144)$

$N_S = 4m^2 + 8m - 66$

$D = \frac{N_S}{N_T}$

$N_{\sigma_1} = 4\,(m-7)(m-6)$

$N_{\sigma_2} = 12\,(3m - 14) + 6$

$x_{\sigma_1} = \frac{N_{\sigma_1}}{N_S}$

$x_{\sigma_2} = \frac{N_{\sigma_2}}{N_S}$

Kinetic and adsorption constants of a nanoparticle with m atoms along its edge

$k^{**}_{1,\sigma_1} = 83.8 \cdot x_{\sigma_1} \rightarrow k^{*}_{1,\sigma_1} = k^{**}_{1,\sigma_1} \cdot D$

$k^{**}_{2,\sigma_1} = 2.3 \cdot x_{\sigma_1} \rightarrow k^{*}_{2,\sigma_1} = k^{**}_{2,\sigma_1} \cdot D$

$k^{**}_{3,\sigma_2} = 24.0 \cdot x_{\sigma_2} \rightarrow k^{*}_{3,\sigma_2} = k^{**}_{3,\sigma_2} \cdot D$

$k^{**}_{4,\sigma_2} = 428.2 \cdot x_{\sigma_2} \rightarrow k^{*}_{4,\sigma_2} = k^{**}_{4,\sigma_2} \cdot D$

$K_{Y,\sigma_1} = 20.5$

$K_{Y,\sigma_2} = 56.5$

$K_{E,\sigma_1} = 0.2$

$K_{E,\sigma_2} = 2.7$

Langmuir-Hinshelwood rate expressions

$r_1 = \frac{k^{*}_{1,\sigma_1} K_{Y,\sigma_1} C_Y}{\left(1+K_{Y,\sigma_1} C_Y + K_{E,\sigma_1} C_E\right)^2}$

$r_2 = \frac{k^{*}_{2,\sigma_1} K_{Y,\sigma_1} C_Y}{\left(1+K_{Y,\sigma_1} C_Y + K_{E,\sigma_1} C_E\right)^2}$

$r_3 = \frac{k^{*}_{3,\sigma_2} K_{Y,\sigma_2} C_Y}{\left(1+K_{Y,\sigma_2} C_Y + K_{E,\sigma_2} C_E\right)^2}$

$r_4 = \frac{k^{*}_{4,\sigma_2} K_{E,\sigma_2} C_E}{\left(1+K_{Y,\sigma_2} C_Y + K_{E,\sigma_2} C_E\right)^2}$

Conversion and selectivity

$X = \frac{0.05941 - C_Y}{0.05941}$

$S = \frac{C_E}{0.05941 - C_Y}$

Mass balances

$\frac{dC_Y}{dt} = -r_1 - r_2 - r_3$

$\frac{dC_E}{dt} = r_1 + r_3 - r_4$

$\frac{dC_A}{dt} = r_2 + r_4$

Figure 4.14 shows some of the simulation steps performed. Over 200 simulations were run for this sample, but only 40 are shown in the figure for clarity reasons. Figure 4.14A and 4.14B show the same variable, MBE concentration as a function of conversion and reaction time, respectively. They exemplify two possible ways of presenting the same information, only that Figure 4.14A is visually more straightforward with respect to the maximum concentration of MBE. Figure 4.14C, on the other hand, shows MBA concentration profile with respect to conversion, which is logically complementary to that of MBE. The combination of Figure 4.14A and 4.14C derives in Figure 4.14D, which shows the selectivity of MBE expected for different sizes of octahedral nanoparticles, the lower curve

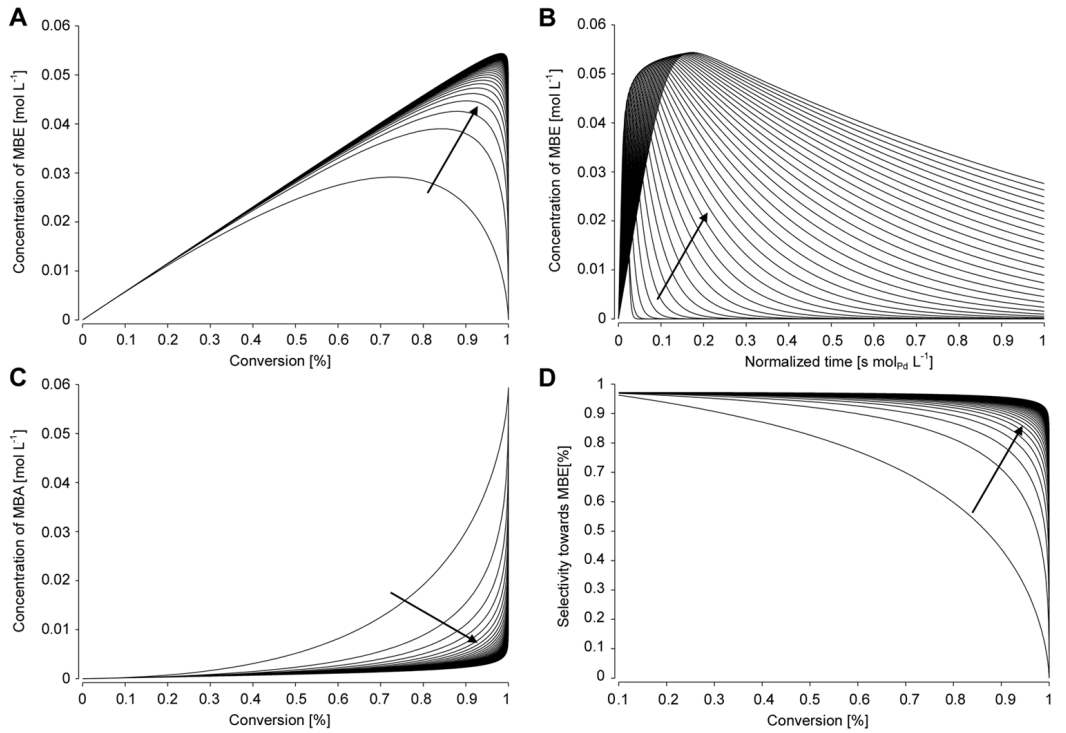

Figure 4.14: Some of the simulation steps performed for octahedral Pd nanoparticles. The arrows point towards increasing nanoparticle size. A) MBE concentration profiles as a function of conversion, B) MBE concentration profiles as a function of reaction time, C) MBA concentration profiles as a function of conversion and D) selectivity towards MBE as a function of conversion.

corresponding to roughly 3 nm nanoparticles and the uppermost to 50 nm nanoparticles, respectively.

Figure 4.13C shows the results of the simulations runs. Selectivity towards MBE increases monotonically with particle size in the order cubes>octahedra>cube-octahedra. Figure 4.13B and C can be combined (Figure 4.13D) to simultaneously optimize selectivity and activity, showing that the reaction is indeed structure sensitive in the size range studied. In this case, the productivity of the target product is plotted against particle size for all three shapes. As a result, two optimal nanoparticles can be proposed. If the productivity of MBE is to be maximized, then cubic nanoparticles of approximately 3 nm would be the best choice. If, on the other hand, a pure selectivity criterion is judged as more

appropriate, then larger cubic nanoparticles should be chosen. In this case, a compromise between productivity and selectivity must be reached.

The structure-sensitivity of a chemical reaction is specific for each catalytic system [17]. Therefore, such modeling-simulation approach combined with the experimental kinetic data obtained from uniform, well-defined metal nanoparticles, gives a powerful tool for rational catalyst design for a given chemical reaction.

4.4 Conclusions

We have studied the structure sensitivity of the water-assisted selective hydrogenation of MBY over uniform, unsupported Pd nanoparticles with different sizes and shapes. The Pd nanoparticles were prepared using a solution-phase method, with PVP serving as a stabilizing agent. The observed activity and selectivity suggested that two types of active sites were involved in the catalysis, which differ in coordination numbers and are located on planes and edges, respectively. A two-site Langmuir-Hinshelwood kinetic model allowed for an accurate description of the experimentally observed activity and selectivity. Semi-hydrogenation to MBE was found to occur on both types of sites, but the reactivity depended on the coordination number of the atoms. Edge atoms were 4-fold less active in the semi-hydrogenation as compared to the plane atoms. Over-hydrogenation to MBA occurred solely on the edge atoms presumably due to increased adsorption strength of the alkene. Selectivity was then linked to the fraction of edge sites on each type of nanoparticle. Kinetic simulations pointed towards $\sim$3 nm cubic nanoparticles as an optimal catalyst for the highest productivity of MBE per gram of Pd. The morphology of the nanoparticles was found to be stable under the conditions used as shown by TEM imaging.

Metal nanoparticles with tuned sizes and shapes prepared via colloidal techniques can be considered as a new generation of model catalysts, which allow overcoming the material and pressure gaps in catalysis and complementing single crystal studies, which inherently

lack the complexity of industrial catalysis. The approach shown in this work provides a powerful tool for rational catalyst design for a given industrially relevant chemical reactions under real conditions.

Chapter 5

Stabilizer effect on the structure sensitivity of MBY hydrogenation

In this chapter, the results obtained when testing di-2-ethylhexylsulfoccinate (AOT)stabilized cube-octahedral Pd nanoparticles of two different sizes in the water-assisted hydrogenation of MBY are reported. The observed behavior was rationalized applying the two-site reaction mechanism developed in Chapter 4, and the results compared to those obtained with PVP-stabilized nanoparticles in order to elucidate how the nature of the stabilizing agents used during synthesis could affect the behavior of the specific active sites. This study implies stepping into the meso-scale complexity of rational catalyst design, since the interaction of the species surrounding the active sites and the catalytic response of the latter is investigated.

This chapter is based on the following publication:

M. Crespo-Quesada and L. Kiwi-Minsker. Size-Tailored Pd Nanoparticles in the Selective Hydrogenation of 2-methyl-3-butyn-2-ol: Effect of the Stabilizing Agent. Submitted.

5.1 Introduction

5.1.1 Context

As seen previously, structure-sensitivity studies began primarily on single crystals [24, 26, 27]. However, these systems lacked the complexity normally present under industrial operation. Model catalysts [28–30] were thus developed so as to present well-defined metal nanoparticles, although the conditions used were still far from the real ones. With the development of simple preparation routes for obtaining size-controlled metal nanoparticles during the past decade [4,5,31,32], along came numerous attempts to use such nanoparticles in structure-sensitivity studies under real operational conditions. On the other hand, the synthesis of shape-controlled metal nanoparticles was achieved more recently, and expanded the opportunities of research even further. However, the shape-controlled synthesis of Pd nanoparticles implies the use of various growth-directing agents. Despite the extensive cleaning procedures applied to the obtained nanoparticles, it is common to find traces of the stabilizing and capping agents which modify the true catalytic behavior of the metal [128, 185, 186].

In Chapter 4, we used well-defined Pd nanoparticles of several sizes and shapes to study the structure sensitivity of the hydrogenation of MBY. By testing the nanoparticles in unsupported form, possible support effects were avoided. Furthermore, since the same stabilizing agent was used for all samples, its effect could be neglected. Therefore, a strictly *nano-scale rational catalyst design* was performed through simulation of the kinetics of the reaction derived from a reaction mechanism that satisfied the experimental evidence.

If a step further is taken in the pursuit of rational catalyst design, then the *meso-scale level* is encountered, in which the active sites are influenced by their environment. In this chapter, we embark in the study of the interaction of the specific active sites with the stabilizing agents surrounding the nanoparticles. In order to achieve this objective, di-2-ethylhexylsulfoccinate (AOT)-stabilized cube-octahedral Pd nanoparticles of two different

sizes were synthesized and tested in the selective hydrogenation of MBY under the same reaction conditions than those in Chapter 4. Thus, the influence of the nature of the stabilizing agent on the catalytic behavior of the specific active sites involved in the catalysis could be assessed.

5.1.2 Experimental details

Catalyst preparation

The AOT-stabilized Pd nanoparticles were prepared following the procedures presented in Section 3.1.1.

Catalyst characterization

Pd concentration was determined by AAS. The morphology of the nanoparticles was examined by TEM imaging. Detailed descriptions of the apparatus used and conditions applied to perform all these analyses can be found in Section 3.5.

Hydrogenation experiments

MBY hydrogenation reactions were carried out in the baffled semi-batch stainless steel reactor described in Section 3.4.1. The 8-blade disk turbine impeller was used as stirrer. The nanoparticles, together with the reactant, were diluted in water up to 200 mL and sonicated for five minutes before introducing them in the reactor. The detailed experimental procedure can be found in the aforementioned section.

5.2 Nanoparticle characterization

Figure 5.1 shows the AOT-stabilized cube-octahedral Pd nanoparticles of two different sizes, namely COT6 and COT12 of 5.5 nm and 11.5 nm in diameter, obtained by synthesis

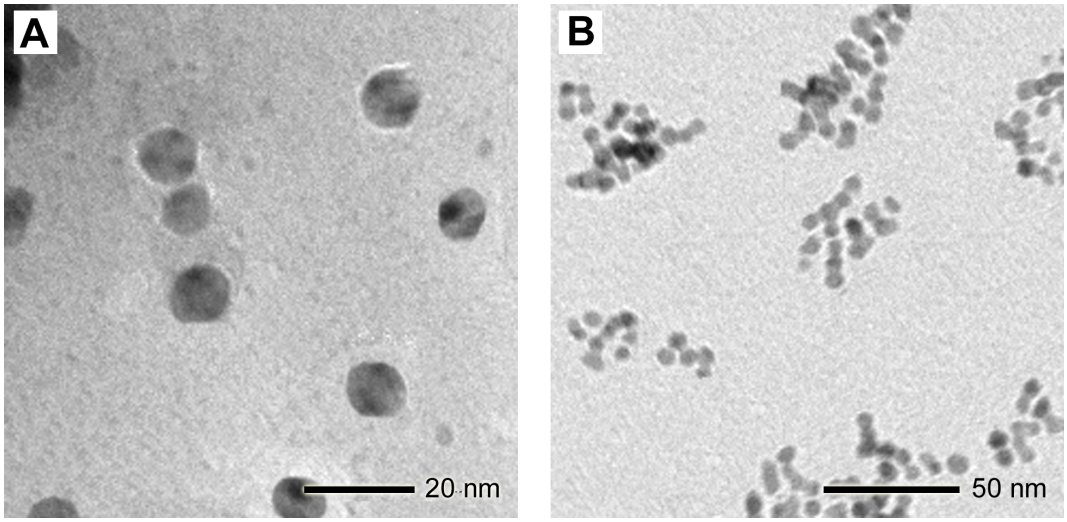

Figure 5.1: TEM images of the samples used in this work. A) AOT-stabilized 11.5 nm cube-octahedra (COT12) and B) AOT-stabilized 5.5 nm cube-octahedra (COT6).

Table 5.1: Surface statistics of the catalysts used in this study.

Sample	d_p [nm]	D [%]	x_{111} [%]	x_{100} [%]	x_{edge} [%]
COT6	5.5	18.3	43.7	5.6	30.3
COT12	11.5	9.2	60.6	11.8	16.6

through a reverse microemulsion technique in which the surfactant to metal ratio was changed in order to control the size.

Table 5.1 gathers the surface statistics of the nanoparticles used in this study. In order to estimate this information, Van Hardeveld and Hartog's [20] approach was used with the more realistic model accounting for an incomplete outermost layer of surface atoms .

5.3 Structure sensitivity of MBY hydrogenation

The aforementioned nanoparticles were tested in the water-assisted hydrogenation of MBY under the same conditions than those shown in Chapter 4. The observed activities were then expressed in terms of TOF:

$$TOF\left[s^{-1}\right] = \frac{r\left[\frac{mol}{mol_{Pd}s}\right]}{D} \tag{5.1}$$

In Chapter 4, PVP-stabilized cubic (6 and 18 nm), octahedral (31 nm) and cube-octahedral (5.5 nm) nanoparticles were tested in order to elucidate the structure sensitivity of the reaction and to determine its mechanism. All nanoparticles were active and selective thus demonstrating that Pd_{100} can indeed effectively hydrogenate MBY. Furthermore, the results suggested that more than one active site, namely plane and edge atoms (or σ_1 and σ_2 sites, respectively) could be responsible for the catalytic behavior observed. Indeed, a two-site Langmuir-Hinshelwood kinetic model allowed for an accurate description of the experimentally observed activity and selectivity. According to the reaction network shown in Figure 4.10B, semi-hydrogenation was then proposed to occur on both types of sites, but the reactivity depended on the coordination number of the atoms (paths 1 and 3). Edge atoms were 4-fold less active in the semi-hydrogenation as compared to plane atoms. Over-hydrogenation to the alkane occurred solely on the edge atoms presumably due to an increased adsorption strength of the alkene on the latter (path 2). The existence of parallel routes happening in different active sites in structure sensitive reactions and their influence on selectivity is a subject that hasn't hitherto been much discussed in the literature [17]. The observed activity of a catalyst could then be modeled with the following expression:

$$TOF_{obs} = TOF_{\sigma_1} \cdot x_{\sigma_1} + TOF_{\sigma_2} \cdot x_{\sigma_2} \tag{5.2}$$

The same approach was applied to the AOT-stabilized Pd nanoparticles in order to compare the results obtained with different stabilizing agents. Figure 5.2 shows a comparison of the observed TOFs as a function of nanoparticle dispersion for PVP and AOT-stabilized nanoparticles. The overall trend was respected, with increasing TOF as dispersion decreases. This behavior is referred to as antipathetic structure sensitivity and is

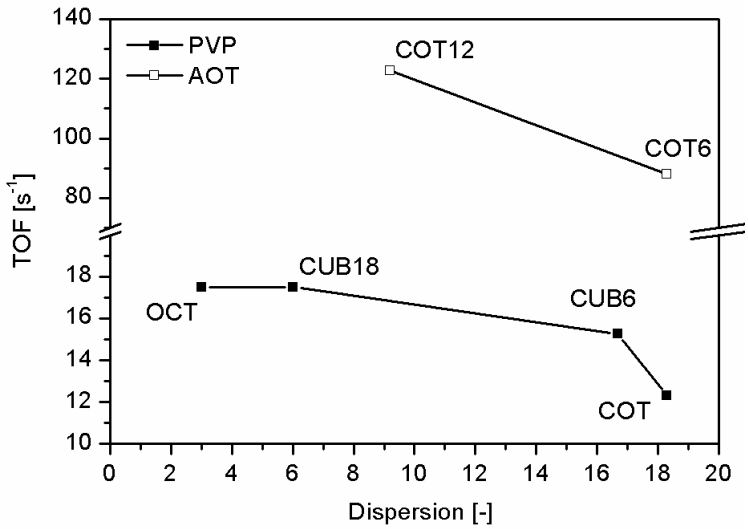

Figure 5.2: Observed TOFs of the hydrogenation of MBY over PVP and AOT stabilized nanoparticles as a function of dispersion. Reaction conditions: 1 g of MBY in 200 mL of water, 333 K, 0.3 MPa of H_2 and 0.05 mg of Pd.

Table 5.2: Specific activity for plane and edge atoms.

Stabilizer	TOF_{plane} [s^{-1}]	TOF_{edge} [s^{-1}]
PVP	19.3±2.4	4.7±0.8
AOT	164.4±0.1	22.9±0.01

common for this reaction [44]. Nonetheless, the TOFs registered when testing the AOT-stabilized nanoparticles were sensibly higher that those stabilized with PVP. This trend had already been observed in the hydrogenation of ethylene over TTAB and PVP stabilized nanoparticles and was attributed to a weaker interaction of TTAB with metal surfaces than PVP [190]. AOT can also be considered a weak stabilizer, since AOT-capped nanoparticles showed the same activity as CTAB-stabilized ones in the selective hydrogenation of MBY [48].

The specific TOFs were subsequently estimated by solving equation 5.2 with a least squares approach, using the surface characteristics for each sample presented in Table 5.1. Table 5.2 gathers the values obtained for both PVP and AOT.

It can be seen that the model could be successfully applied to the AOT-stabilized

nanoparticles as well. Furthermore, plane atoms were also found to be more active than edge atoms for the semi-hydrogenation. This could be rationalized since the adsorption strength of the substrate on a given metal varies in the same order: aromatic $<$ olefin $<$ diolefin $<$ alkyne [51]. This observation implies that an increase in the adsorption strength of the alkyne, such as adsorbing on an electronically deficient site (i.e. an edge atom) rather than on a plane atom, would reduce the activity, whereas an opposite trend would be observed for the olefin.

The selectivity towards the alkene was slightly influenced by the nature of the stabilizer, but not by the morphology of the nanoparticles. Indeed, all PVP-stabilized nanoparticles showed roughly 96% selectivity towards MBE at 50% conversion, whereas for the AOT-stabilized nanoparticles, a value of 90% was obtained at the same conversion. This promoting effect of PVP, could derive from its stronger interaction with the Pd nanoparticles. Promotion with N-containing molecules is usually rationalized by either a selective site blocking with respect to the alkene [175], or by a modification of the electronic properties of the nanoparticles [3, 75, 76, 178] and is thoroughly investigated and reported in Chapter 6.

5.4 Nanoparticle size and shape optimization

The determination of the specific TOFs for each type of active site allows to model and predict the activity of hypothetical nanoparticles of a given size and shape, much like it was done in the previous chapter.

Figure 5.3 shows the predicted TOF and MBY transformation rates for three common nanoparticle shapes in the 3-50 nm range. Naturally, the trend is the same than the one that was obtained in Chapter 4 for PVP-stabilized Pd nanoparticles. The magnitudes, however, vary substantially. In this case, shape was also irrelevant as far as plane atoms are concerned. That is, cubes and octahedra are expected to show the same activity.

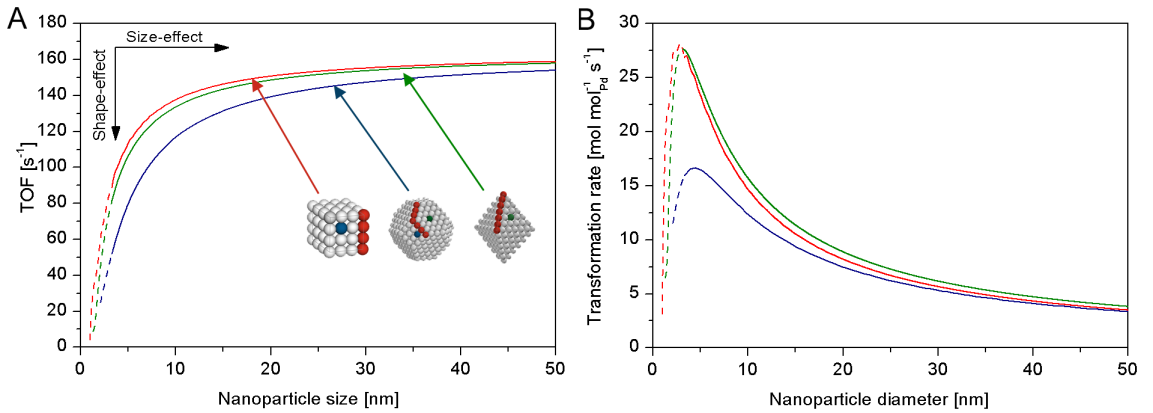

Figure 5.3: Optimization of AOT-stabilized Pd nanoparticle size and shape based on A) TOF and B) MBY transformation rate.

Consequently, cubes or octahedra of roughly 3 nm are expected to be the most active size and shape for this application.

5.5 Conclusions

The meso-scale level of rational catalyst design was tackled in this chapter. The interaction and effect of different stabilizing agents on the molecular reaction mechanism was studied. The results obtained in this chapter showed that nanoparticles stabilized by AOT were more active yet less selective than those stabilized by PVP.

The two-site mechanism developed in Chapter 4 was successfully applied to AOT-stabilized Pd nanoparticles in the water-assisted selective hydrogenation of MBY and was useful to rationalize the effect exerted by the stabilizing agents. Indeed, Pd atoms stabilized by AOT were found to be an order of magnitude more active than those stabilized by PVP. This could be attributed to the stronger interaction of PVP with Pd surface atoms as compared to AOT. Furthermore, AOT-stabilized Pd nanoparticles were found to be less selective. This promoting effect probably derives from a dual site-blocking/electronic modification of Pd in the presence of N-containing substances, a matter which is investigated and discussed in Chapter 6.

Chapter 6

Catalyst promotion through the use of modifiers

In this chapter, 2,2'-bipyridine and an imidazolium functionalized bipy ligand were used to synthesize Pd nanoparticles. The function of such ligands was twofold: first, as stabilizing agents to prevent the agglomeration of the nanoparticles during synthesis, and second, to act as permanent catalyst modifiers. The N-modified Pd nanoparticles were subsequently deposited on CNF/$SMF_{Inconel}$ supports and tested in the liquid-phase hydrogenation of 1-hexyne. The catalysts were found to be significantly more selective than an analogous reference catalyst with non-modified Pd nanoparticles. Moreover, the high selectivity was maintained up to full conversion and the over-hydrogenation was thus suppressed due to a site-blocking effect of the N-containing ligands.

This chapter is based on the following publication:

M. Crespo-Quesada, R. Dykeman, G. Laurenczy, P. Dyson, and L. Kiwi-Minsker. Supported Nitrogen-Modified Pd Nanoparticles for the Selective Hydrogenation of 1-hexyne. *Journal of Catalysis*, 279(1):66-74, 2011.

6.1 Introduction

6.1.1 Context

As presented in Section 2.5.2, the yield of the alkene in hydrogenation reactions increases considerably when modifiers or additives are added to the reaction mixture [177]. In liquid-phase reactions, common modifiers include nitrogen-containing ligands (ammonia, quinoline [76, 165, 175, 176], pyridine, etc.) and sulfur-containing compounds [176]. Additives can not only be added to the reaction mixture (*reaction modifiers*) but they can also be present as a catalyst component (*catalyst modifier*). In this way, a 0.5% Pd/Al_2O_3 catalyst treated with Zn acetate, pyridine and KOH showed high selectivity in the hydrogenation of MBY [75]. Permanent modification of Pd nanoparticles with pyridine has been achieved by stabilizing them inside poly-4-vinylpyridine block-copolymers [87, 191, 192]. Both systems were studied in the hydrogenation of dehydrolinalool and showed 99% selectivity, which was attributed to the electronic effects of the pyridine functionality on the Pd surface. As seen in Chapter 5, the nature of the compounds present in the catalyst formulation can play an important role in the final observed behavior. In some cases, choosing the appropriate stabilizing agent exerting a modifier effect on the active phase can further tailor the desired catalytic response.

Molecular additives are not the only alternative found in the literature for this purpose. In the past few years, ionic liquids (IL), i.e. salts that are liquid at room temperature, have gained popularity in catalysis since they create a non-nucleophilic environment which may increase the activity and the lifetime of the catalyst. Nevertheless, in some cases they can participate in the catalytic process acting as additives in the form of ligands [193]. Although vastly used as solvents in homogeneous catalysis, supported Pd nanoparticles embedded in ILs have already been found useful for tailoring the selectivity in several liquid-phase hydrogenations [143, 194, 195]. ILs have also been found to exert an electronic effect on embedded Pd nanoparticles in the hydrogenation of acetylene causing an increase

in the selectivity towards ethylene [144].

In heterogeneous catalysis, metallic nanoparticles are often unstable and prone to sintering, particularly at the temperatures typical of catalytic reactions [196]. In order to obtain high catalytic activity and stability, metal nanoparticles are generally dispersed on support materials, or directly synthesized on them. They are then more or less firmly anchored to the support, on which they are effectively separated from each other. All kinds of materials which are thermally stable and chemically relatively inert can be used as supports, but alumina, silica and carbon are the most widely used, with magnesia, titania, zirconia, zinc oxide, used for particular applications [196]. To overcome the drawbacks of conventional catalytic reactors, structured catalysts can be used [132]. In this chapter, SMF filters were used as structured supports (see Section 2.4.2). In order to increase their specific surface area and to enhance nanoparticle anchoring, the SMF were coated with a layer of CNF which were subsequently activated through boiling in H_2O_2 (see Section 2.4.3).

In the study reported in this chapter, an in-house synthesized imidazolium tagged bipy ligand and bipy itself were used in the synthesis of monodispersed Pd nanoparticles both in water and in ILs. These ligands had a dual aim: stabilizing the nanoparticles by anchoring them to the support and inducing a permanent modification of the surface. To the best of our knowledge, the combination of a functionalized structured support and a tailored-made ligand capable of strongly interacting in order to minimize leaching while increasing selectivity has not been previously reported. The resulting catalysts were tested in the liquid-phase hydrogenation of 1-hexyne in n-heptane and their performance was compared to that of a reference Pd/CNF/SMF catalyst, prepared by a conventional ion-exchange method [69], in the absence of modifiers.

Table 6.1: Catalysts used in this work.

Catalyst	Stabilizer	nanoparticle synthesis in	IL coating	% Pd[a]	% IL
Reference	-	-	-	0.6	-
Reference	-	-	[bmim][PF_6]	0.8	4.2
Reference	-	-	[C_2OHmim][BF_4]	0.5	5.4
Reference	-	-	[C_3CNmim][Tf_2N]	0.6	4.2
SILC(Bip)	Bipy	[bmim][PF_6]	[bmim][PF_6]	4.0[b]	3.0
SILC(Bih)	[BIHB]Br_2	[bmim][PF_6]	[bmim][PF_6]	3.9[b]	3.7
SC(Bip)	Bipy	water	-	3.2[b]	-
SC(Bih)	[BIHB]Br_2	water	-	2.0[b]	-

[a] Percentage expressed by mass of CNF.
[b] Percentage expressed by total mass of catalyst.
[BIHB]Br_2 {4,4'-bis[7-(2,3-dimethylimidazolium)heptyl]-2,2'-bipyridine}bromide
[bmim][PF_6] 1-Butyl-3-methyl-1H-imidazolium hexafluorophosphate
[C_2OHmim][BF_4] 1-(2-Hydroxyethyl)-3-methyl-1H-imidazolium tetrafluoroborate
[C_3CNmim][Tf_2N] 1-(3-cyanopropyl)-3-methyl-1H-imidazolium bis(trifluoromethane) sulfonimide

6.1.2 Experimental details

Table 6.1 lists the catalysts used throughout this work and provides a succinct description of the procedure used for their synthesis. A more detailed description can be found below.

N-modified Pd/CNF/SMF catalyst preparation

Support The composite CNF/$SMF_{Inconel}$ supports were prepared following the procedure presented in Section 3.2.1.

N-containing ligands 2,2'-bipyridine (bipy) was purchased and used as received. {4,4'-Bis[7-(2,3-dimethylimidazolium)heptyl]-2,2'-bipyridine}bromide ([BIHB]Br_2), on the other hand, was synthesized as described in Section 3.1.3.

N-modified Pd nanoparticle synthesis The N-modified Pd nanoparticles were prepared following the procedure presented in Section 3.1.3.

N-modified Pd nanoparticles immobilization $CNF/SMF_{Inconel}$ supports in the form of round (∼2 cm diameter) slices (0.3 g) were activated in 50 mL of boiling 30% H_2O_2 for 4 h. The nanoparticles were subsequently deposited onto the former by incipient wetness impregnation and dried for 15 h at 323 K in vacuo.

Reference Pd/CNF/SMF catalyst preparation

The method used to synthesize and immobilize the Pd nanoparticles onto $CNF/SMF_{Inconel}$ supports has been reported elsewhere [69]. Briefly, the $CNF/SMF_{Inconel}$ supports (activated in 50 mL of boiling 30% H_2O_2 for 4 h) were immersed in a solution containing a Pd precursor (Na_2PdCl_4) for 5 h at room temperature. Afterwards, they were dried, calcined and reduced in a flow of 200 mL min^{-1} of 50% H_2 in Ar at 423 K for 18 h, thus generating Pd nanoparticles with a mean diameter of ∼6.5 nm.

Catalyst characterization

Pd concentration was determined by AAS. Surface characterization of the nanoparticles was performed with XPS. The morphology of the nanoparticles was examined with TEM imaging, and SEM was used to investigate the morphology of the catalysts. NMR was used to measure product solubilities at low concentrations. Detailed descriptions of the apparatus used and conditions applied to perform all these analyses can be found in Section 3.5.

The solubility of H_2 in $[C_3CN_{mim}][Tf_2N]$ was estimated using a literature method [197]. 2.5 mL of the IL was sealed in a sapphire NMR tube at a pressure of 100 atm H_2. After vigorous shaking a ^1H NMR spectrum of the solution was recorded. The ^1H NMR spectrum was fitted with WINNMR and NMRICMA2.8/MATALAB programs (nonlinear least squares fit, minimizing the difference between the measured and calculated spectra to determine the spectral parameters and integrals). The Henry's constant for H_2 was found to be 510 MPa and the hydrogen concentration 1.28 mM at 1 atm [198].

In order to measure the solubility of the organic compounds in the ILs, an excess of the compound (either n-hexane, 1-hexene or 1-hexyne) was added to a 3 ml screw cap vial containing a magnetic stir bar and the IL ([bmim][PF_6], [C_2OHmim][BF_4] or [C_3CNmim][Tf_2N]) and mixed at room temperature (293 K) for 14 h, after which time the majority of the IL and a fraction of the organic compound were transferred to a 5 mm NMR tube and allowed to settle to ensure only the IL layer would be analyzed by the receiver coil. Spectra were recorded at 298 K without an internal reference. The resulting ^{1}H NMR spectra were analyzed using Bruker TOPSPIN 1.3 NMR software with deconvolution (fit type of Lorentzian) employed where necessary to obtain the appropriate integration.

Hydrogenation experiments

The hydrogenation of 1-hexyne in n-heptane was performed in the semi-batch stainless steel reactor described in Section 3.4.1. The structured catalyst was placed between the two metal gauzes fixed on the self-gassing hollow shaft stirrer shown in Figure 3.6. The reactor was charged with 1-hexyne (4.13 g) and octane as internal standard (2.82 g) and filled to 200 mL with n-heptane. The detailed experimental procedure can be found in the aforementioned section.

6.2 Reference Pd/CNF/SMF catalyst

6.2.1 Catalyst morphology

CNF/$SMF_{Inconel}$ supports

Figure 6.1A shows a representative image of the individual fibers of approximately 8 μm in diameter of the raw $SMF_{Inconel}$ after calcination. After reduction and one hour of CVD, a thick and uniform layer of CNF was formed, as seen in Figure 6.1B. The morphology of the CNF/$SMF_{Inconel}$ support comprises an array of CNF with an individual diameter of

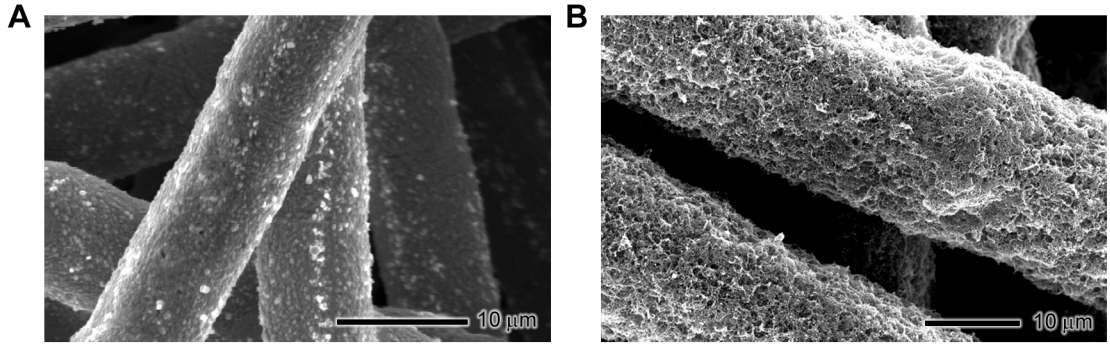

Figure 6.1: HRSEM images depicting the catalyst's preparation procedure. A) Calcined SMF Inconel and B) CNF grown on SMF after ethane CVD.

approximately 40-50 nm coating the surface of each fiber of the $SMF_{Inconel}$.

Final catalyst

An increase in magnification (Figure 6.2A) shows some interesting features of this material: the intertwined, yet open structure of CNF can be observed in addition to the Ni nanoparticles of 50-100 nm in size that served as catalyst for the formation of CNF, as confirmed by EDX [156], and that prove the tip-growth mode of the CNF. Figure 6.3 presents a TEM image of an isolated CNF. The inset shows a HRTEM picture of the surface of the Ni tip, where several layers of graphitic carbon are deposed during the CVD. This layer ensures the inertness of the $CNF/SMF_{Inconel}$ support during the reaction. The TEM image presented in Figure 6.2B shows monodispersed ($\sim$7 nm) Pd nanoparticles that are evenly distributed along a single CNF. The mean particle size was also estimated via CO-chemisorption, yielding a value of 6.5 nm, in good agreement with the TEM images.

6.2.2 Heat and mass transfer limitations

Before comparing catalyst performances or deriving kinetic expressions, it is necessary to verify whether the system operates under kinetic regime. The calculations were performed for the reference Pd/CNF/SMF catalyst, which was the most active, in order to ensure

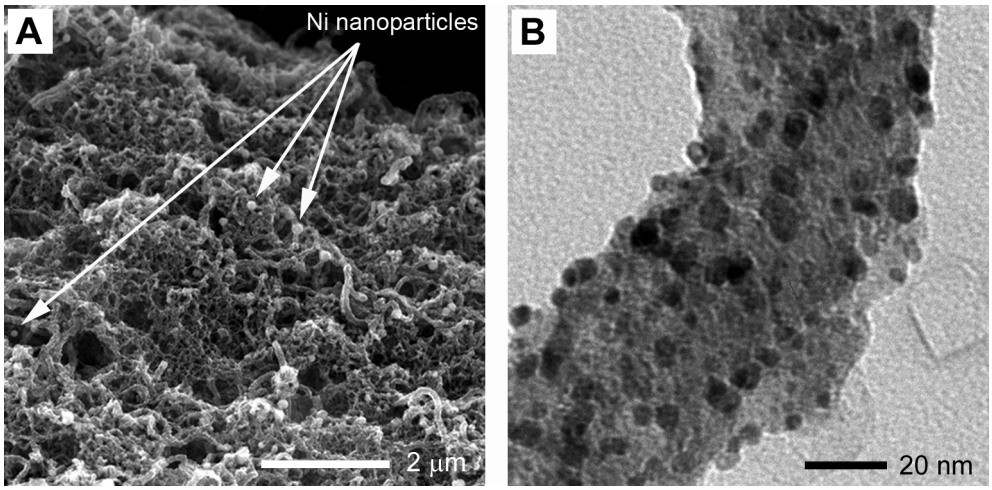

Figure 6.2: Reference catalyst. A) SEM image of the CNF/SMF support and B) TEM showing well dispersed Pd nanoparticles anchored onto the CNF.

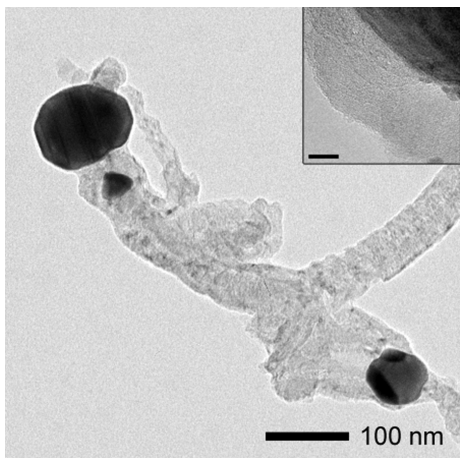

Figure 6.3: TEM image of a single CNF. Ni metallic particles of 50-100 nm can be found at the tip of the CNF, which are covered by several layers of graphitic carbon (see inset, scale bar: 10 nm).

that all other catalysts also operate under kinetic regime.

Internal heat transfer

Heat transfer is not likely to affect the reaction rate of a moderately exothermic liquid-phase reaction such as the hydrogenation of 1-hexyne. It is possible, however, to estimate the maximum temperature in the center of a catalyst pellet by combining and integrating the microscopic mass and heat balances in such pellet:

$$\Delta T_{max} = \frac{D_{eff,Y}\left(-\Delta \hat{H}_R\right) C_{Y,bulk}}{k_{eff}} \tag{6.1}$$

The enthalpy of the reaction was estimated to be -163 kJ/mol [199,200]. The subindex Y makes reference to 1-hexyne. A good approximation for the efficient conductivity, k_{eff}, was proposed by Woodside and Messmer [201].

$$k_{eff} = k_{Inconel}\left(\frac{k_{heptane}}{k_{Inconel}}\right)^{\varepsilon} \tag{6.2}$$

The effective diffusivity, D_{eff}, can be estimated from the molecular diffusivity of hexyne in heptane and the porosity and tortuosity of the SMF support.

$$D_{eff,Y} = \frac{\varepsilon}{\tau} D_{Y,heptane} \tag{6.3}$$

The porosity of the support is 0.8 and the tortuosity was assumed to be 4, as suggested by Satterfield [202]. The diffusivity of hexyne in heptane was estimated from Hayduk-Minhas' correlation for hydrocarbon mixtures [203]:

$$D_{Y,heptane} = 13.3 \cdot 10^{-8}\, T^{1.47}\, \mu_{heptane}^{\left(\frac{10.2}{V_Y} - 0.791\right)}\, V_Y^{-0.71} \tag{6.4}$$

where V_Y is the molar volume of 1-hexyne. This yields a maximum temperature difference of 0.07 K, for which heat transfer limitations can be disregarded.

External mass transfer

External mass transfer limitations were assessed with the stirring rate criterion. The reaction rate of the reference catalyst was found to be independent of the stirring rate between 1750 and 2200 rpm, thus discarding the influence of external mass transfer on the reaction rate within this domain.

Internal mass transfer

In order to determine the influence of internal mass transfer, a classical experiment consists in varying the size of the catalyst pellet. This is not feasible with the system used in this study. Another solution consists in applying the Weisz-Prater criterion [204]; this alternative is advantageous since the modulus can be calculated from measurable or easily estimated parameters:

$$\Phi = \frac{L_e^2 \left(-R_{Y,obs}\right) \rho_c}{D_{eff,Y}\, C_{Y,bulk}} \lll 1 \tag{6.5}$$

In our case, the support consists of two levels of porosity, i.e. the macroscopic SMF structure and the microscopic CNF which are grown on the former; Weisz' modulus was thus estimated in the microscopic level to exclude all possible internal mass transfer influences. An average pore diameter of the CNF structure could be estimated from the values of specific surface area and the pore volume [156] and was found to be 3.2 nm, which shows that CNF are a mesoporous material. The characteristic length chosen was the thickness of the CNF layer, which is the longest possible distance that a molecule of reactant has to travel and is equal to 1 μm [156]. Assuming a porosity of 0.5 and knowing that the tortuosity of activated carbon cloths was found to be 9.1 [205], Weisz' modulus at 25% conversion was estimated to be 0.09, thus discarding internal mass transfer influences in the mesoporous CNF structure.

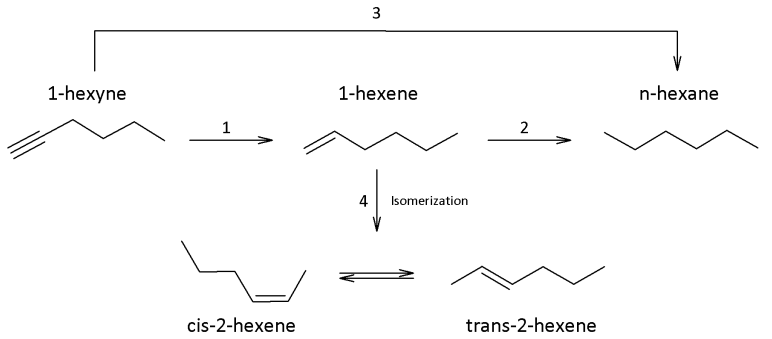

Figure 6.4: Reaction network for the hydrogenation of 1-hexyne.

6.2.3 Catalytic behavior

The reference catalyst showed a high activity in the hydrogenation of 1-hexyne with a TOF $\sim$200 s^{-1}. The full mechanism shown in Figure 2.8 could be simplified, since some of the byproducts were not observed under the experimental conditions used (Figure 6.4).

The formation of n-hexane takes place not only in a consecutive way (path 2, Figure 6.4), but also in a parallel way (path 3, Figure 6.4) since their formation is already detected at conversions close to zero. The 2-hexene isomers were almost undetectable until the maximum yield of 1-hexene was reached. After complete consumption of the 1-hexyne, 1-hexene was rapidly transformed into hexane and its two isomers with a ratio of 1:1.

A Langmuir-Hinshelwood mechanism was applied for modeling the kinetics assuming dissociative weak adsorption of hydrogen. For path 1 and 3 (Figure 6.4), the second addition of hydrogen was considered as the rate determining step. For path 2, the first addition of hydrogen was considered as the rate determining step. The adsorption equilibrium constants of the hydrogenated products are small compared to the alkyne. Therefore, the adsorption constant of n-hexane and the alkene isomers, K, was considered to be equal. This assumption, together with the weak hydrogen adsorption on Pt group metals [188], allows the following simplified equations to be deduced:

$$r_1 = \frac{k_1 K_Y C_Y K_H C_H}{\left(1 + K_Y C_Y + K_E C_E + K\left(C_A + C_I\right)\right)^2} \tag{6.6}$$

$$r_2 = \frac{k_2 K_E C_E K_H C_H}{\left(1 + K_Y C_Y + K_E C_E + K\left(C_A + C_I\right)\right)^2} \tag{6.7}$$

$$r_3 = \frac{k_3 K_Y C_Y K_H C_H}{\left(1 + K_Y C_Y + K_E C_E + K\left(C_A + C_I\right)\right)^2} \tag{6.8}$$

$$r_4 = \frac{k_4 K_E C_E^2}{\left(1 + K_Y C_Y + K_E C_E + K\left(C_A + C_I\right)\right)^2} \tag{6.9}$$

In order to ascertain an overall kinetic rate equation, the full set of differential equations describing the concentration variation of all species participating in the reaction is required (subscripts 1, 2, 3 and 4 refer to the different reaction paths in Figure 6.4):

$$\frac{dC_Y}{dt} = \frac{n_{Pd}}{V}\left(-r_1 - r_3\right) \tag{6.10}$$

$$\frac{dC_E}{dt} = \frac{n_{Pd}}{V}\left(r_1 - r_2 - r_4\right) \tag{6.11}$$

$$\frac{dC_A}{dt} = \frac{n_{Pd}}{V}\left(r_2 + r_3\right) \tag{6.12}$$

$$\frac{dC_I}{dt} = \frac{n_{Pd}}{V} r_4 \tag{6.13}$$

These eight equations (6.6-6.13) can be solved simultaneously using Berkeley's Madonna software [189] with Rosenbrock's method [206]. The model parameters were estimated by fitting the simulated curves to the experimental data giving the kinetic constants k_1-k_4 and the adsorption constants K_Y, K_E, K_H and K presented in Table 6.2.

Table 6.2: Adsorption and kinetic constants found for the reference catalyst and SILC(Bih)[a].

Adsorption constants [$\mathrm{L\,mol^{-1}}$]			Kinetic constants [$mol\, g_{Pd}^{-1}\, s^{-1}$]		
	Reference	SILC(Bih)		Reference	SILC(Bih)
K_Y	23.1	35.9	k_1	2486.1	2503.3
K_N^b	-	9.6	k_2	1162.3	54.1
K_E	0.8	0.1	k_3	208.8	154.4
K	8.3	4.7	k_4	11.1	10.1
K_H^c	$1 \cdot 10^{-3}$	$2 \cdot 10^{-3}$			

[a] Reaction conditions: 4.1 g of 1-hexyne, 2.82 g of octane as internal standard, 0.3 g of catalyst, 303 K and 1.05 MPa of H_2 in 200 mL of n-heptane.
[b] Dimensionless.
[c] This constant is the product $K_{H_2}C_{H_2}$ and is dimensionless.

It is worth noting that fitting such expressions makes the result dependent on the starting values given to the constants. In order to obtain reliable results, the starting values for each constant are set and certain constraints applied, such as hydrogen adsorption constant much smaller than the rest, no negative values and higher values for k_1 and K_Y. This kinetic model has been successfully applied for other liquid-phase alkyne hydrogenations over palladium catalysts [73,74]. Figure 6.5 shows the prediction curves obtained with the kinetic model proposed.

A correlation coefficient of 98.5% was achieved according to equation 6.14.

$$R^2 = \left[\frac{\sum (x - \overline{x})(y - \overline{y})}{\sqrt{\sum (x - \overline{x})^2 (y - \overline{y})^2}} \right]^2 \tag{6.14}$$

The adsorption constant of 1-hexyne was found to be 2 orders of magnitude higher than that of 1-hexene, in line with other results reported for hydrogenations over Pd [73,207]. Furthermore, the adsorption constant of hydrogen was 4 orders of magnitude smaller than that of the alkyne, thus validating the weak adsorption assumption made when developing the model. The kinetic constant of the first reaction (path 1, Figure 6.4) was only twice

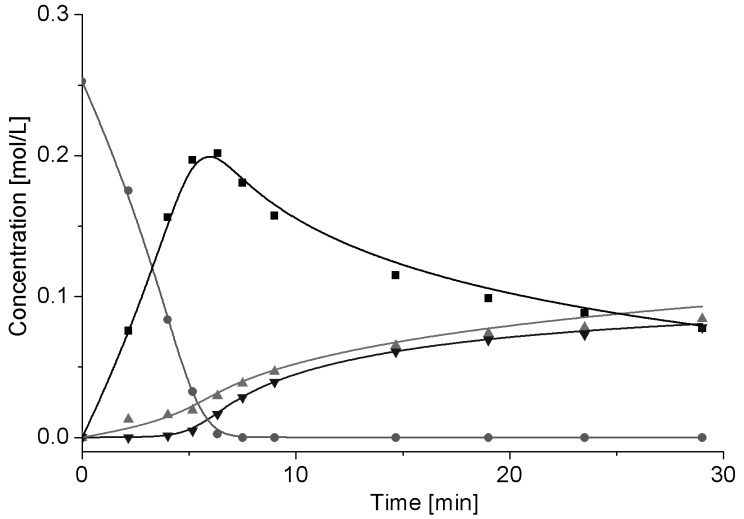

Figure 6.5: Experimental points and kinetic curves modeled using Berkeley's Madonna software for the reference catalyst. ● 1-hexyne, ■ 1-hexene, ▲ n-hexane, ▼ 2-hexene isomers. Reaction conditions: 4.1 g of 1-hexyne, 2.82 g of octane as internal standard, 0.3 g of catalyst, 303 K and 1.05 MPa of H_2 in 200 mL of n-heptane.

as high as that for the over-hydrogenation (path 2, Figure 6.4). This is in agreement with the thermodynamic basis for the selectivity proposed by Molnar et al. [3], i.e. the high selectivity towards the alkene is due to a stronger adsorption of the alkyne, compared to the alkene, rather than a higher kinetic constant of different hydrogenation steps.

6.3 Supported N-modified Pd nanoparticles

6.3.1 N-modified Pd nanoparticles

Figure 6.6 shows TEM images and the particle size distributions of each sample of the bipy-stabilized Pd nanoparticles synthesized in water and in [bmim][PF_6]. The solvent influences the mean diameter of the nanoparticles, but the ligand (either bipy or [BIHB]Br_2) does not, with approximately the same particle size distribution in the two solvents independent of the ligand employed. Pd loading on CNFs was found to be between 2 and 4%.

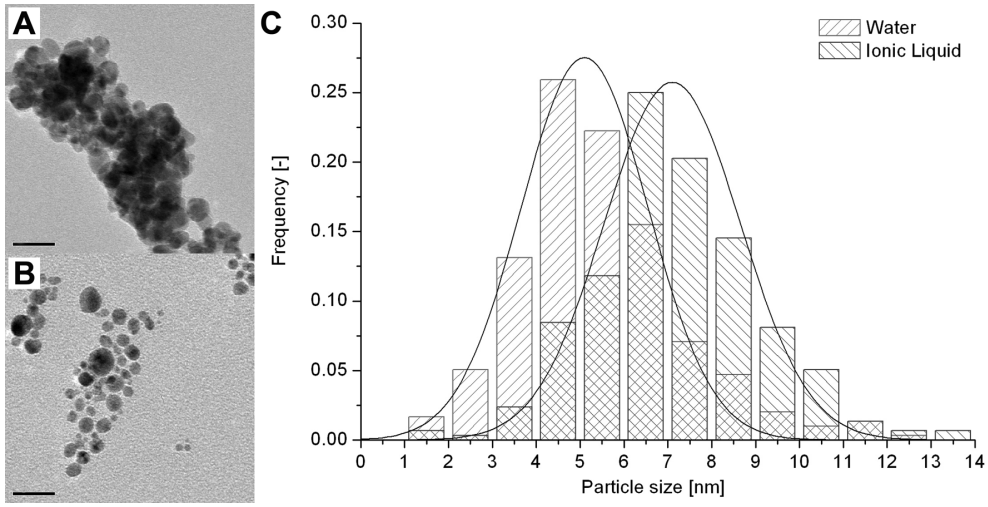

Figure 6.6: TEM images and C) particle size distribution of the Pd nanoparticles synthesized with bipy as stabilizer in A) [bmim][PF_6] and B) water. The scale bars correspond to 20 nm.

6.3.2 Catalytic effect of N-containing ligands: synthesis in [bmim][PF_6]

Figure 6.7 shows the catalytic results for SILC(Bih) (see Table 6.1) in the hydrogenation of 1-hexyne.

The differences compared to the reference catalyst (Figure 6.5) are significant, since the over-hydrogenation towards the alkane (path 2, Figure 6.4) appears to be completely suppressed. Furthermore, both the initial selectivity and the maximum yield of 1-hexene increased by 10%. A similar effect, albeit less pronounced, was observed with a S-based modifier [74] and quinoline [73] added to the reaction mixture in the liquid-phase hydrogenation of 2-methyl-3-butyn-2-ol.

The same kinetic model as described above was used with the exception that a new dimensionless constant, K_N, was added in the denominator of equations 6.6 to 6.9, to take into account the permanent adsorption of the N-containing ligands on the Pd nanoparticle surface:

$$r_1 = \frac{k_1 K_Y C_Y K_H C_H}{\left((1 + K_N) + K_Y C_Y + K_E C_E + K\left(C_A + C_I\right)\right)^2} \tag{6.15}$$

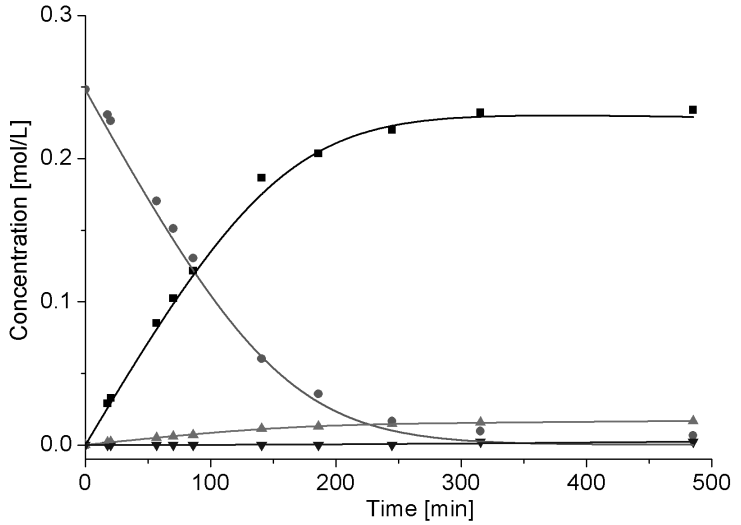

Figure 6.7: Experimental points and kinetic curves modeled using Berkeley's Madonna software for SILC(Bih). ● 1-hexyne, ■ 1-hexene, ▲ n-hexane, ▼ 2-hexene isomers. Reaction conditions: 4.1 g of 1-hexyne, 2.82 g of octane as internal standard, 0.3 g of catalyst, 303 K and 1.05 MPa of H_2 in 200 mL of n-heptane.

A comparison of the constants is provided in Table 6.2. The results shown suggest two possible explanations for the effect of the N-containing ligands.

Firstly, the initial coverage of the modifier (θ_N=0.49) is slightly higher than the maximum coverage of the substrate (θ_Y=0.46) and is 2 orders of magnitude higher than the maximum coverage of the desired product ($\theta_E = 2.4 \cdot 10^{-3}$). In order to determine whether the alkyne and the modifier were in a dynamic adsorption/desorption regime, 0.2 g of the catalyst was stirred in 200 mL of heptane containing 4.1 g of hexyne at 30 °C for 3 hours. The sample was studied by ^{1}H NMR spectroscopy and both bipy and [BIHB]Br_2 were below the detection limit. The concentration may be thus estimated to be < 3.75 mmol L^{-1}. This implies that, in order to react, the alkyne must temporarily displace the modifier from the active site, which probably adopts a more packed adsorption conformation, which is reverted to the original mode of adsorption once the alkyne has reacted. Therefore, the N-based ligands most probably increase the selectivity through a permanent site blocking effect.

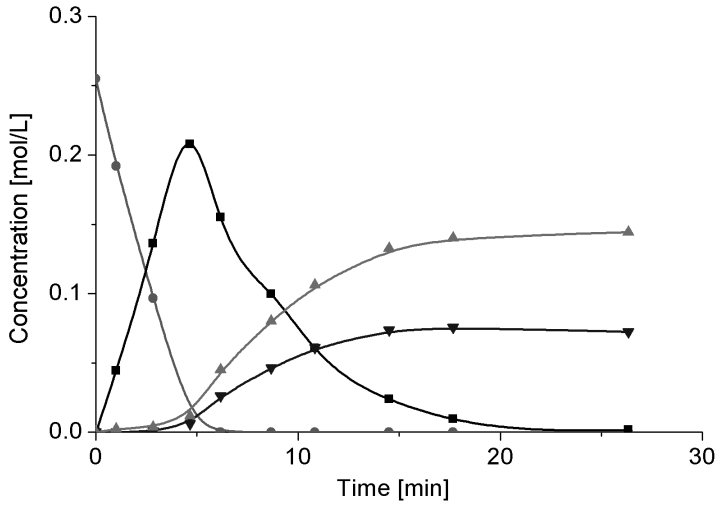

Figure 6.8: Experimental points for Lindlar's catalyst. ● 1-hexyne, ■ 1-hexene, ▲ n-hexane, ▼ 2-hexene isomers. Reaction conditions: 4.1 g of 1-hexyne, 2.82 g of octane as internal standard, 0.3 g of catalyst, 303 K and 1.05 MPa of H_2 in 200 mL of n-heptane.

Secondly, an electronic effect is also observed. As suggested in the literature, a nucleophilic ligand increases the electron density of Pd, thus leading to a change in the alkyne/alkene relative strength of adsorption as well as a decrease in alkene heat of adsorption, both of which were observed in the model (Table 6.2) [3,75,76,178].

A well known example of Pd permanent modification aimed at enhancing the selectivity is the addition of Pb to Pd in Lindlar's catalyst [164,165]. In order to compare its effectiveness with the catalytic results reported herein, Lindlar's catalyst (5% Pd/3.5%Pb/$CaCO_3$) was tested under the same reaction conditions (Figure 6.8).

Selectivity was found to be only 95% at 25% conversion (against 98.5% over our catalyst), and dropped quickly when approaching full conversion. The most important difference is that the over-hydrogenation reaction was not hindered with Lindlar's catalyst.

Catalytic effect of ILs

In order to study the effect due solely to the IL in which the nanoparticles were embedded, the reference catalyst was covered with a layer IL either [bmim][PF_6], [C_2OHmim][BF_4]

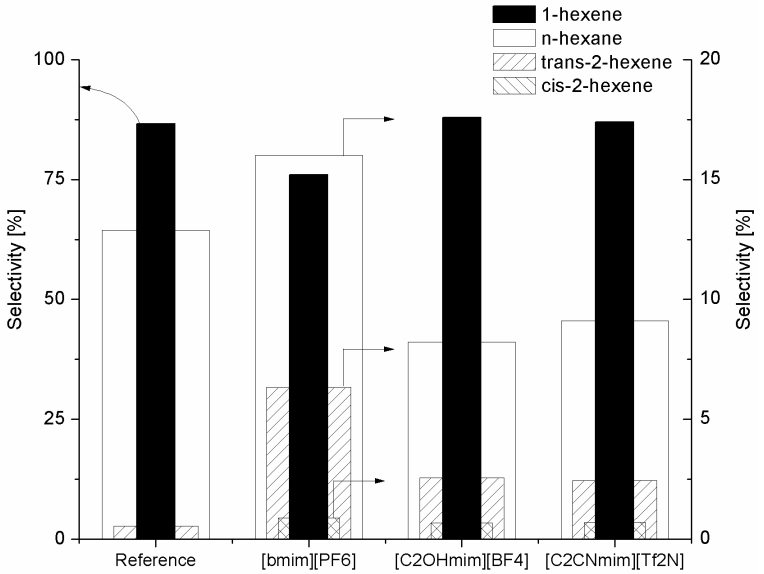

Figure 6.9: Product distribution at 50% conversion for the IL-coated reference catalysts. Reaction conditions:.

or $[C_3CNmim][Tf_2N]$ and tested in the hydrogenation of 1-hexyne. All catalysts were less active than the reference and, surprisingly, the selectivity towards the target product did not improve significantly. Nevertheless, the product distribution was affected by the type of IL as seen in Figure 6.9.

With the use of $[bmim][PF_6]$, selectivity towards 2-hexene isomers, particularly the trans-isomer, was increased at the expense of the alkene compared to the reference catalyst. Employing either $[C_2OHmim][BF_4]$ or $[C_3CNmim][Tf_2N]$, on the other hand, showed an alkane:isomers ratio significantly lower than that of the reference catalyst. ^1H NMR spectroscopy measurements revealed that the solubility of 1-hexyne, 1-hexene and n-hexane are practically the same in $[bmim][PF_6]$ and $[C_3CNmim][Tf_2N]$ hence eliminating solubility as being responsible for the differences observed in the product distribution. Differences in H_2 solubility in ILs could also offer a possible explanation [195], but gas solubility measurements showed no correlation between the two. A ligand site-blocking effect appears to be the most plausible explanation for the change in product distribution since both hydroxyl and nitrile functionalities can conceivably interact with the Pd surface, as is proposed for

Table 6.3: Performance of the various catalysts tested in the hydrogenation of hexyne.[a]

Catalyst	S[b] [%]	R $[mol\, mol_{Pd}^{-1}\, s^{-1}]$	TOF [s^{-1}]
Reference	88.0	47.0	223.8
SILC(Bip)	97.0	4.3	29.5
SILC(Bih)	94.0	11.0	60.8
SC(Bip)	98.4	1.7	11.5
SC(Bih)	97.8	1.4	7.6

[a] Reaction conditions: 4.1 g of 1-hexyne, 2.82 g of octane as internal standard, 0.3 g of catalyst, 303 K and 1.05 MPa of H_2 in 200 mL of n-heptane.
[b] Selectivity towards 1-hexene at 25% conversion.

Pd nanoparticles prepared in $[C_2OHmim][BF_4]$ and $[C_3CNmim][Tf_2N]$ [208–210]. Presumably, coverage of the Pd nanoparticle surface by the donor atoms of the IL is very high and influences the reaction selectivity.

6.3.3 Catalytic effect of N-containing ligands: synthesis in water

The change in the catalytic behavior may be attributed to the N-modified Pd nanoparticles, and to confirm this hypothesis, the nanoparticles were synthesized in water, separated by centrifugation and redispersed in acetone. The solution was then used for impregnating the CNF/SMF composite supports (SC(Bip) and SC(Bih)), and the resulting catalysts were tested under the same reaction conditions (see Table 6.3).

A similar behavior in the hydrogenation of 1-hexyne was found regardless of the N-containing ligand used for synthesizing the Pd nanoparticles. The N-modified Pd nanoparticles prepared in water demonstrated the same initial selectivity towards 1-hexene (∼98%). Moreover, the reaction rate and TOF were in both cases significantly lower than that of the reference catalyst.

XPS measurements showed that the Pd nanoparticles present different oxidation states on their surfaces. All three catalysts contain a peak between 335.2-335.4 eV, consistent with metallic Pd. The reference catalyst shows a peak corresponding to Pd^{2+} at 337.2 eV

consistent with palladium oxide. The corresponding band of the two N-modified nanoparticles was significantly shifted to higher values (337.9-338.1 eV) corresponding to Pd^{2+}ions coordinated to the N-containing ligands. Note that $PdCl_2$(bipy) exhibits a binding energy of 338.1 eV. These results show that the electronic properties of metallic Pd were not altered by the presence of the N-containing ligands. However, the Pd^{2+} species present on the surface of the catalyst were indeed strongly affected by the complexation of the N-containing ligands. The presence of multiple oxidation states on the surface of catalysts is known to influence their catalytic properties [211]. Here, however, the specific role of the N-modified Pd^{2+} species is not clear, but it is probable that these species contribute to the differences between the Pd nanoparticle catalysts.

A supplementary effect of the N-modified stabilizers may be due to the change of the surface chemistry of the carbon-based supports. A useful tool to examine the nature of the oxygen groups present on the surface of the CNF is XPS. The differences in binding energy for various bonding states are quite small for electronegative atoms. It is therefore convenient to measure the C 1s signal. The C1s spectra was resolved into six individual component peaks comprising carbidic carbon (Peak I), graphitic carbon (Peak II), phenolic or ether groups (Peak III), carbonyl groups (Peak IV), carboxyl or ester groups (Peak V) and satellite peaks due to $\pi - \pi^*$ transitions in aromatic rings (Peak VI). The corresponding binding energies at which these peaks appear can be found elsewhere [212, 213]. A qualitative inspection of the Figure 6.10 shows an increase in the number of carboxylic groups and thus of the acidity of the support upon activation. The deposition of the N-modified Pd nanoparticles affects almost exclusively the carboxylic acid groups, and suggests a subsequent reduction in the acidity of the support. However, as the vast majority of the surface oxygen groups lay beyond the detection limit of XPS [213], the effect of the addition of the N-containing ligands on acidity must be minimal and the overall increase in selectivity is, as expected, due to interactions of the N-containing ligands with

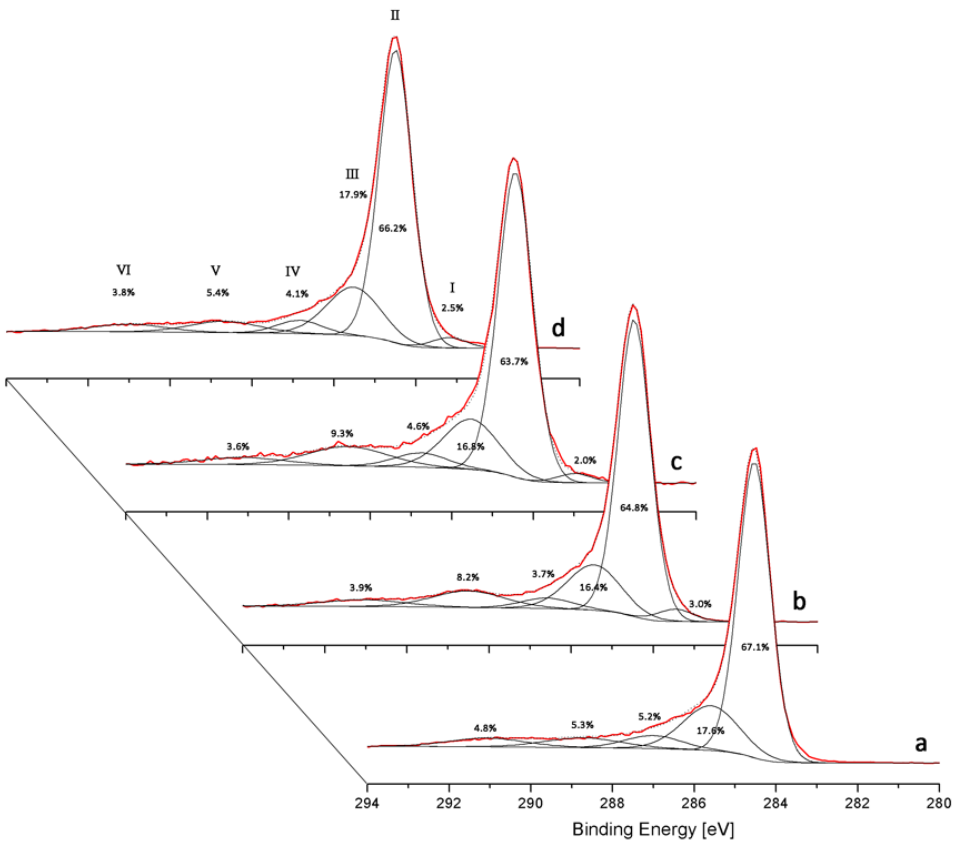

Figure 6.10: High-resolution XPS C 1s spectra of CNF a) as prepared, b) after treatment in boiling H_2O_2 for 4h, c) reference catalyst, and d) after impregnation with N-modified Pd nanoparticles, SC(Bih).

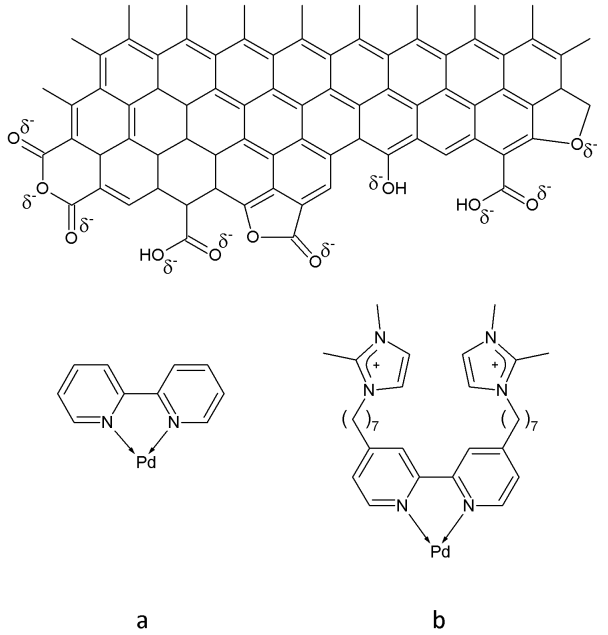

Figure 6.11: Representation of the possible interactions between the N-containing ligands and the oxygenated groups present on the surface of CNF: A) bipyridine and B) [BIHB]Br_2.

the Pd surface.

6.3.4 Resistance to leaching

Leaching of active Pd species from the support is one of the main causes for deactivation in three-phase hydrogenations [214–216]. To compare the level of leaching between the bipy and [BIHB]Br_2-modified catalysts, two halves of a disc of CNF/SMF support were impregnated with the N-modified nanoparticles. Both were stirred in 200 mL of heptane at 30 °C, 1.05 MPa of H_2, 2000 rpm for 1 h. The analysis of the solvent phase revealed that the [BIHB]Br_2-modified catalyst was more stable (9% leaching) than the bipy-modified nanoparticles (14% leaching, implying 55% more leaching in the latter), presumably due to a stronger interaction with the oxygenated surface groups present of the CNF. Ionic interactions between surface bound $O^{\delta-}$ atoms and the cationic $[BIHB]^{2+}$ ligands are probably responsible for the higher stability of the system, as proposed in Figure 6.11.

6.4 Conclusions

N-modified Pd nanoparticles immobilized on CNF/SMF supports were synthesized and studied in the selective hydrogenation of 1-hexyne. Compared to a reference catalyst, selectivity to 1-hexene increased from 83% to 98% near full conversion. Furthermore, the over-hydrogenation to n-hexane was largely suppressed in the presence of N-modified Pd nanoparticles.

A Langmuir-Hinshelwood model was found to be consistent with the observed reaction kinetics and showed that the N-contained ligands permanently adsorb on the Pd surface "blocking" the active sites for 1-hexene adsorption. Nonetheless, an electronic effect from the N-coordinated Pd^{2+} species resulting in a change in the adsorption strengths and kinetic constants also contributes to the change in the catalytic performance. Moreover, the imidazolium functionalized ligand was found to reduce Pd leaching from the catalyst presumably due to a stronger ionic interaction with the oxygenated surface groups present on the CNF.

In this chapter, the potential of stabilizing agents to promote the catalytic response of the active phase was evaluated. The interaction of the active phase with the support was superficially assessed, getting a step closer to the micro-scale rational catalyst design.

Chapter 7

Stabilizer removal through UV-Ozone cleaning

In this chapter, 10 nm PVP-stabilized Pd nanocubes were deposited on CNF/$SMF_{Inconel}$ supports and subsequently treated with UV-Ozone (UVO) in order to eliminate the traces of PVP still present on the surface. Cubes, being a thermodynamically unfavorable shape, are very prone to restructuring to minimize the interfacial free energy, therefore HRSEM imaging was used to evaluate their morphological stability. The process of PVP removal was monitored by XPS, XRD and in-situ ATR-IR. The hydrogenation of acetylene was used as case study to assess the effect of PVP removal on the catalytic response.

This chapter is based on the following publication:

M. Crespo-Quesada, J.M. Andanson, A. Yarulin, B. Lim, Y. Xia, and L. Kiwi-Minsker. UV–Ozone Cleaning of Supported Poly (Vinyl Pyrrolidone)-Stabilized Palladium Nanocubes: Effect of Stabilizer Removal on Morphology and Catalytic Behavior. *Langmuir*, 27(12):7909-7916, 2011.

7.1 Introduction

7.1.1 Context

As seen in the preceding chapters, structure sensitivity studies on well-defined metallic nanoparticles are a valid alternative to theoretical studies [217–219] or to 2D model catalysts ranging from single crystals [24] to monodispersed nanoclusters deposited by lithography techniques [220]. There is however a major drawback in the utilization of such catalysts: in order to study the true catalytic behavior of each crystal plane, this approach requires the removal of the stabilizer and/or capping agents used during synthesis.

In order to remove these substances, plasma cleaning [221], calcination [222], heat [223, 224] and high temperature hydrogen treatments [225] have been reported in the literature. These techniques, however, either require complicated equipment, or can compromise the morphological integrity of the nanoparticles due to harsh treatment conditions. UV-ozone (UVO) cleaning is a useful alternative capable of yielding nearly atomically-clean surfaces [226]. Indeed, this technique has been used in the elimination of various organic capping agents from colloidal Pt [227] and Au [228] nanoparticles.

The available evidence indicates that UVO cleaning is primarily the result of photosensitized oxidation processes, as depicted in Figure 7.1. The contaminant molecules are excited and/or dissociated due to the absorption of UV light ($h\nu_1 = 254\,nm$). Simultaneously, atomic oxygen and ozone are produced when O_2 is dissociated due to the absorption of UV with a wavelength of 184.9 nm ($h\nu_2$). Atomic oxygen is also produced when ozone is decomposed through the absorption of $UV_{h\nu_1}$ light. The excited contaminant molecules and the free radicals produced by the dissociation of contaminant molecules, react with atomic oxygen and ozone to form simpler volatile molecules [226].

Additionally, short wavelength UV ($h\nu_2$) radiation was found to etch both biological and polymeric materials via "ablative photodecomposition" and without significant heating of the sample [226], vital for preserving the morphology of nanoparticles. UVO has been found

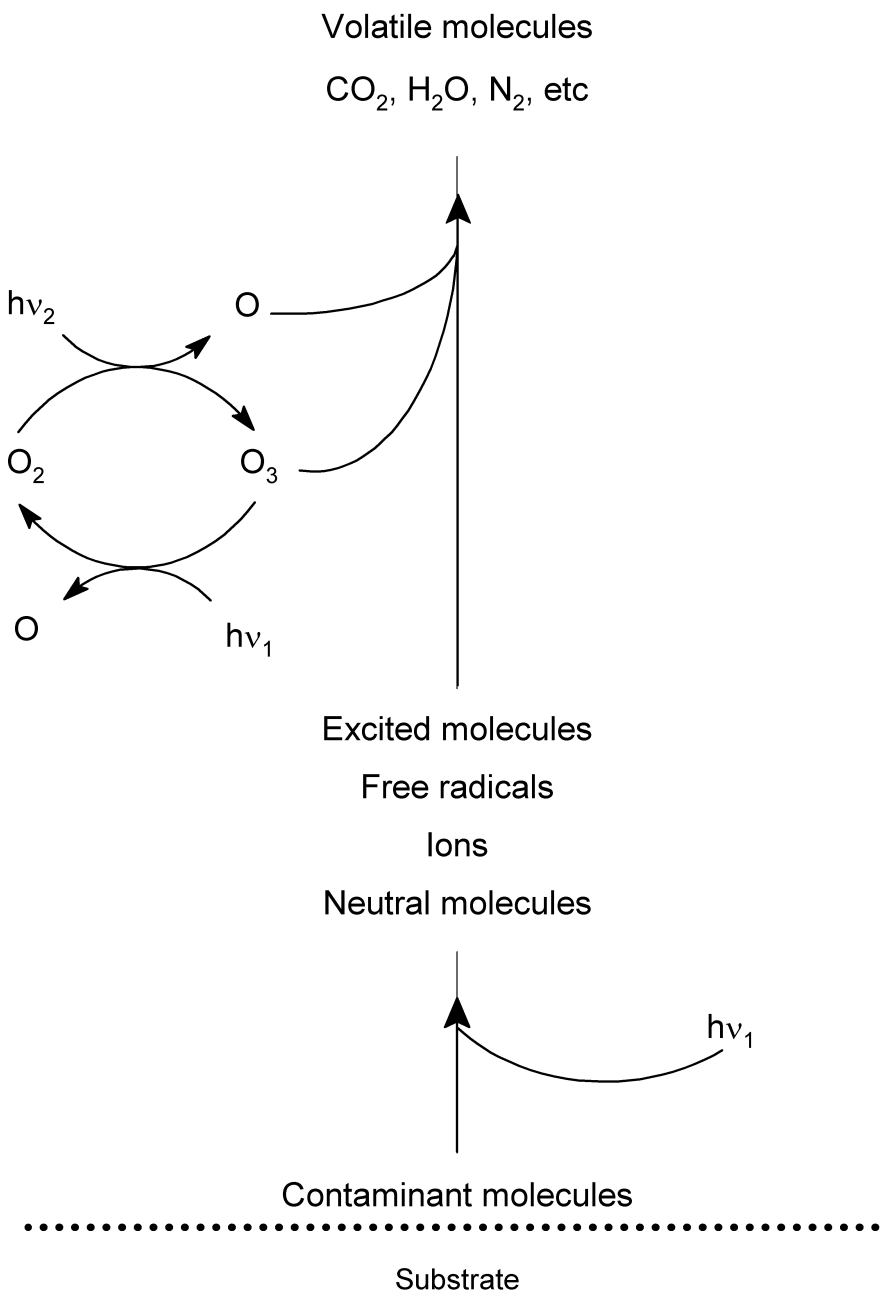

Figure 7.1: Simplified schematic representation of UV-Ozone cleaning process.

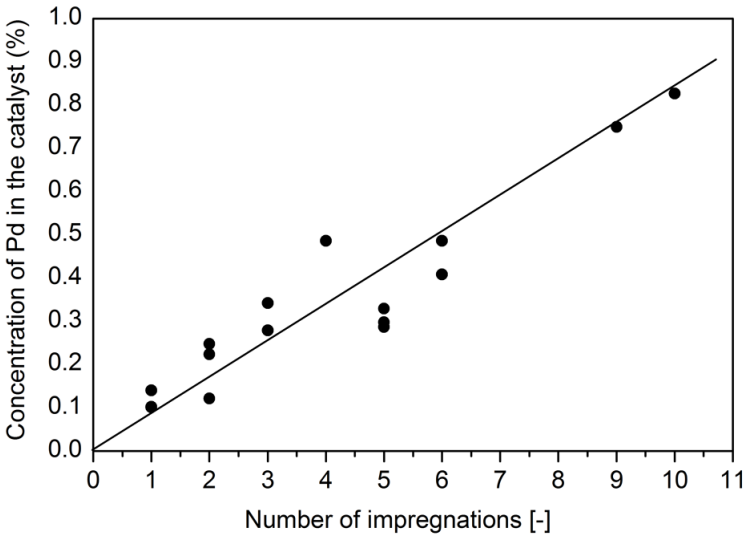

Figure 7.2: Variation of Pd loading with consecutive impregnations.

to etch Teflon and Viton, and will thus likely etch other organic materials as well [226].

7.1.2 Experimental details

Catalyst preparation

The PVP-stabilized nanoparticles were prepared following the procedures presented in Section 3.1.1. The composite CNF/$SMF_{Inconel}$ supports were prepared following the procedures presented in Section 3.2.1.

The nanocubes were subsequently immobilized on the CNF/$SMF_{Inconel}$ supports by incipient wetness impregnation. The discs were then dried under vacuum at 333 K overnight. Pd loading could be conveniently varied by altering the concentration of the colloidal suspension and/or by changing the number of impregnations, as depicted in Figure 7.2.

UVO cleaning was used in order to eliminate traces of PVP from the surface of the nanoparticles. The irradiation with the UV light was conducted using a Helios Quartz (Milan, Italy) 8 W low-pressure mercury lamp emitting at 185 and 257 nm inside a custom-made metallic enclosure. The sample was placed at 5 mm from the lamp during a given

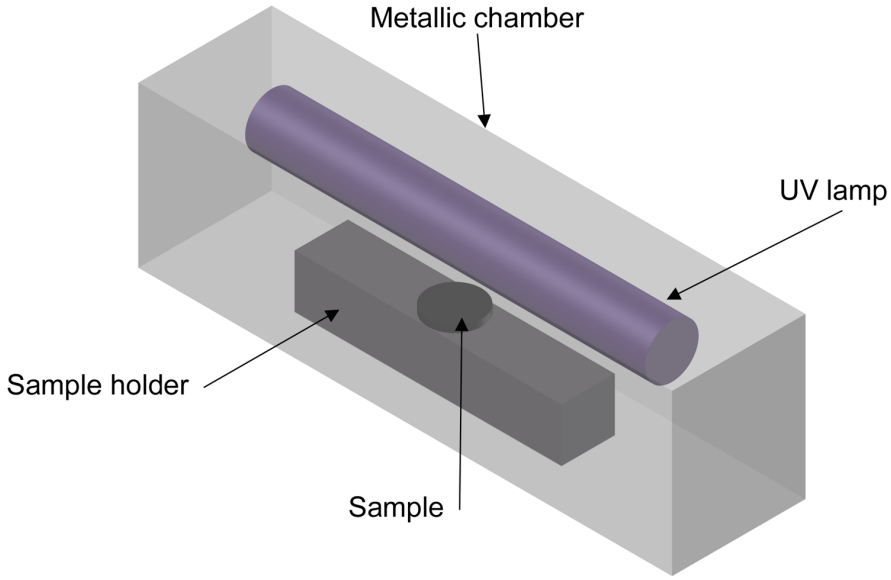

Figure 7.3: Scheme of the setup used for the UVO treatment of catalysts.

amount of time (2-6 h) and was then removed from the UVO chamber (Figure 7.3).

Catalyst characterization

Pd concentration was determined by AAS. Surface characterization of the nanoparticles as well as the support was performed with XRD, XPS and ATR-IR. The nano and micro-morphology of the catalysts was examined with HRSEM, TEM and HRTEM imaging. Detailed descriptions of the apparatus used and conditions applied to perform all these analyses can be found in Section 3.5.

ATR-IR analyses were performed using a homemade ATR high-pressure stainless steel cell equipped with a Ge crystal, which was polished using diamond paste to remove any contaminant traces from previous experiments. During the experiments, the temperature of the cell was kept constant at 293 K. Circa 500 μL of a colloidal solution containing the nanoparticles in ethanol was cast-dropped on the crystal. The ATR cell was either closed in order to flow N_2, H_2 or CO gas, or the UV lamp was placed 5 mm over the crystal, allowing the in-situ monitoring of the UVO cleaning process.

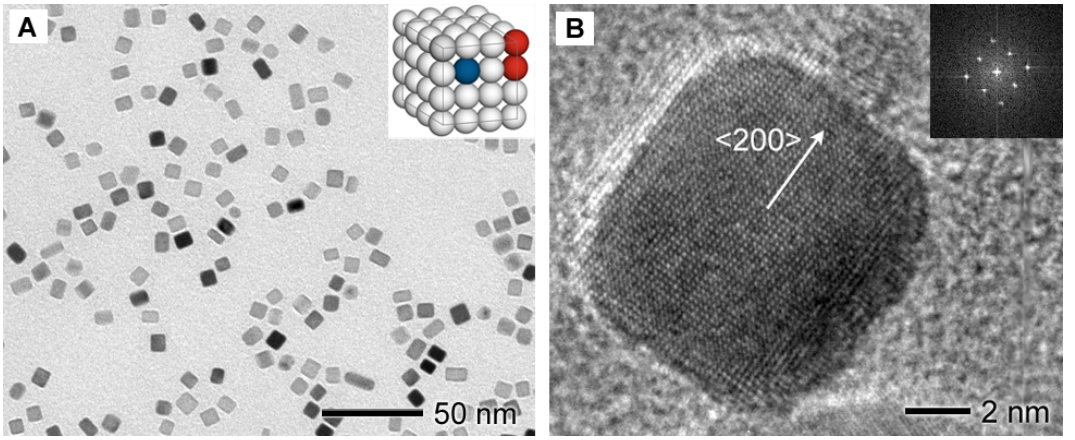

Figure 7.4: A) TEM image of the Pd nanocubes: The inset is a schematic representation of an fcc nanocube, where the Pd_{100} face atoms as well as the corner and edge atoms are evidenced; B) High-resolution image and FTT pattern (inset) of a single nanocube. The lattice spacing of 1.94 Å can be indexed to the {200} reflection of Pd.

Hydrogenation experiments

The hydrogenation of acetylene was carried out in the jacketed differential tubular reactor described in Section 3.4.2. The experimental procedure as well as the calculations made can be found in the same section.

7.2 Catalyst morphology

Pd nanoparticles

Figure 7.4 shows typical TEM and HRTEM images of the PVP-stabilized Pd nanocubes. The inset in Figure 7.4A gives a schematic illustration of a face-centered cubic (fcc) lattice, where atoms belonging to (100) crystal planes, corners, and edges are evidenced. By counting over 200 nanoparticles from different regions of the sample, a mean particle size of 10.1 ± 0.9 nm and a yield of over 95% for the cubic shape enclosed by (100) facets were estimated.

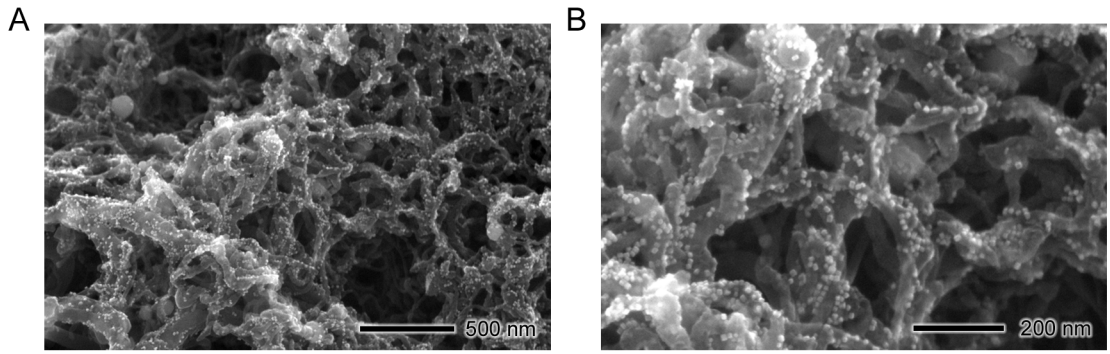

Figure 7.5: A) SEM picture of the supported 10 nm Pd nanocubes where the individual nanoparticles are already visible and B) higher magnification image where the Pd nanocubes can be clearly resolved.

Final catalyst

SEM imaging of the support preparation procedure and its morphological characteristics can be found in Section 6.2.1 (Figure 6.1).

The smaller, bright squares seen in Figure 7.5A are the 10 nm Pd nanocubes, already visible at relatively low magnifications (x 50,000). It can be appreciated that the dispersion of the Pd nanoparticles was uniform and that no agglomerates were formed during the impregnation and drying steps. Furthermore, probably due to the presence of PVP on their surfaces, the nanocubes tended to deposit on the outermost layers of the CNF, leaving the fibers deep inside free of Pd nanocubes. Finally, Figure 7.5B shows a high-magnification SEM image, where the shape of the nanoparticles can be clearly resolved.

7.3 PVP removal

Thermal treatments at relatively high temperatures (∼573 K) have been employed to eliminate organic capping agents without significantly altering the shape and size of metallic nanoparticles [223–225,229]. In this work, the as-prepared catalyst was also subjected to a cyclic oxidation/reduction treatment, which was proven to eliminate the carbonaceous de-

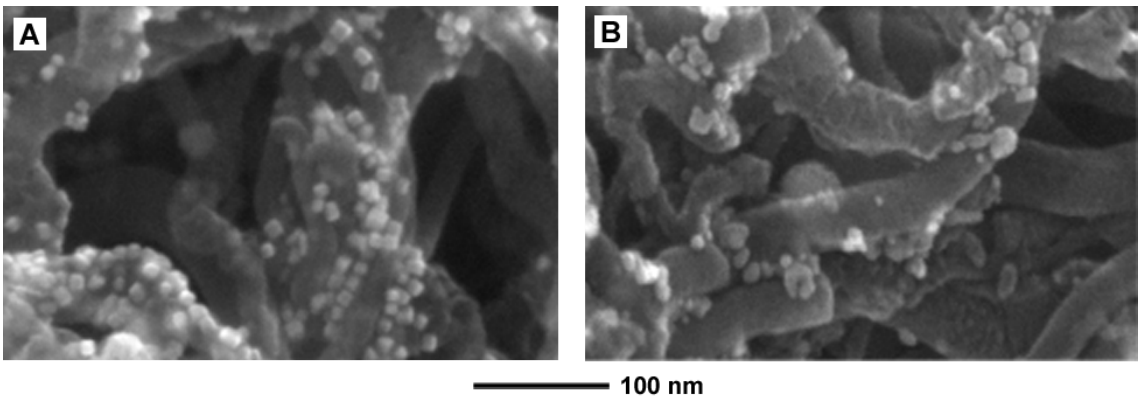

Figure 7.6: HRSEM image of supported Pd nanocubes A) before and B) after the cyclic oxidation/reduction cycle to remove PVP.

posits formed during the combustion of organic molecules [225]. The catalyst was exposed to 2% O_2/N_2 at 393 K for 1 h, after which the gas was switched to 2% H_2/Ar and kept at the same temperature for one additional hour. The cycle was then repeated. Despite that the treatment eliminated PVP from the catalyst (as revealed by XPS), the shape, size, and distribution were drastically altered as seen by SEM imaging (Figure 7.6). Since the aim of this work was to eliminate PVP while keeping the morphology of the active phase intact, the high-temperature treatment method was then deemed not applicable.

7.3.1 High resolution SEM imaging

HRSEM imaging was proven to be a very useful technique in the assessment of morphological changes of nanoscale, shape-tailored Pd nanoparticles during PVP removal. It was found that the shape, size, and distribution of the nanoparticles were well maintained even after 6 hours of UVO treatment, as shown in Figure 7.7 confirming that UVO cleaning was suitable for this application.

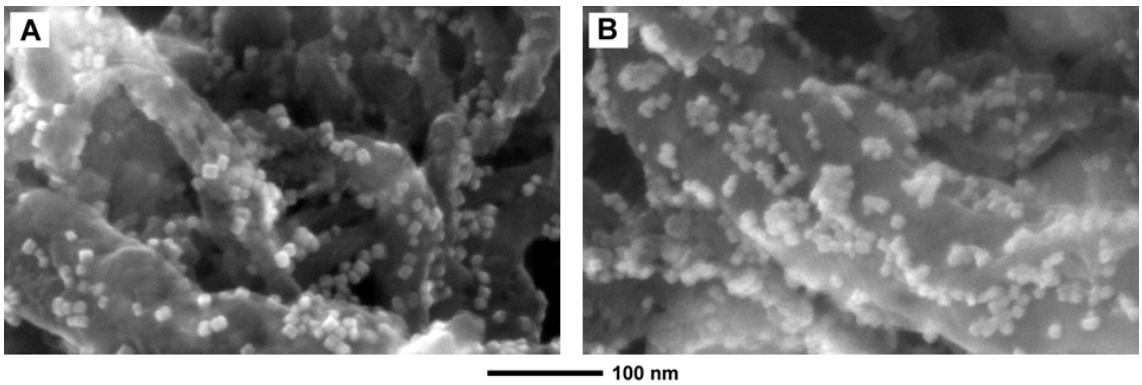

Figure 7.7: High magnification SEM pictures A) before and B) after 6 h of UVO treatment.

7.3.2 *Ex-situ* characterization by XPS and XRD

Pd nanoparticles characterization

The elimination of PVP via UVO treatment was further analyzed *ex situ* by XPS and XRD. Figure 7.8A shows the survey spectra of the fresh catalyst, as well as after 2, 4 and 6 h of UVO treatment, respectively. In this case, the N 1*s* peak (400 eV), while visible in the fresh catalyst, was drastically reduced after only 2 h of treatment. High-resolution scans of the zone revealed that 63% of the N present in the fresh catalyst was eliminated during the first 2 h of treatment. Furthermore, the amount of N was undetectable after 4 and 6 h of treatment. It was found, however, that the UVO cleaning procedure was not able to eliminate PVP from the side which was facing opposite to the lamp. Figure 7.8B shows the XPS spectra for both sides of the catalyst after 4 h under UVO treatment where the peak corresponding to N can be distinctively seen on the side facing away from the lamp.

It can be appreciated from Figure 7.8B that the peaks corresponding to Pd widen throughout the cleaning process. High-resolution scans revealed that the amount of $Pd^{\delta+}$ on the surface of the catalyst increased remarkably by the end of the treatment. Indeed, the amount of $Pd^{\delta+}$ increases from 12% in the fresh catalyst to 54% after 4 h of treatment. However, this increase is probably due to the passivation of Pd through dissociative

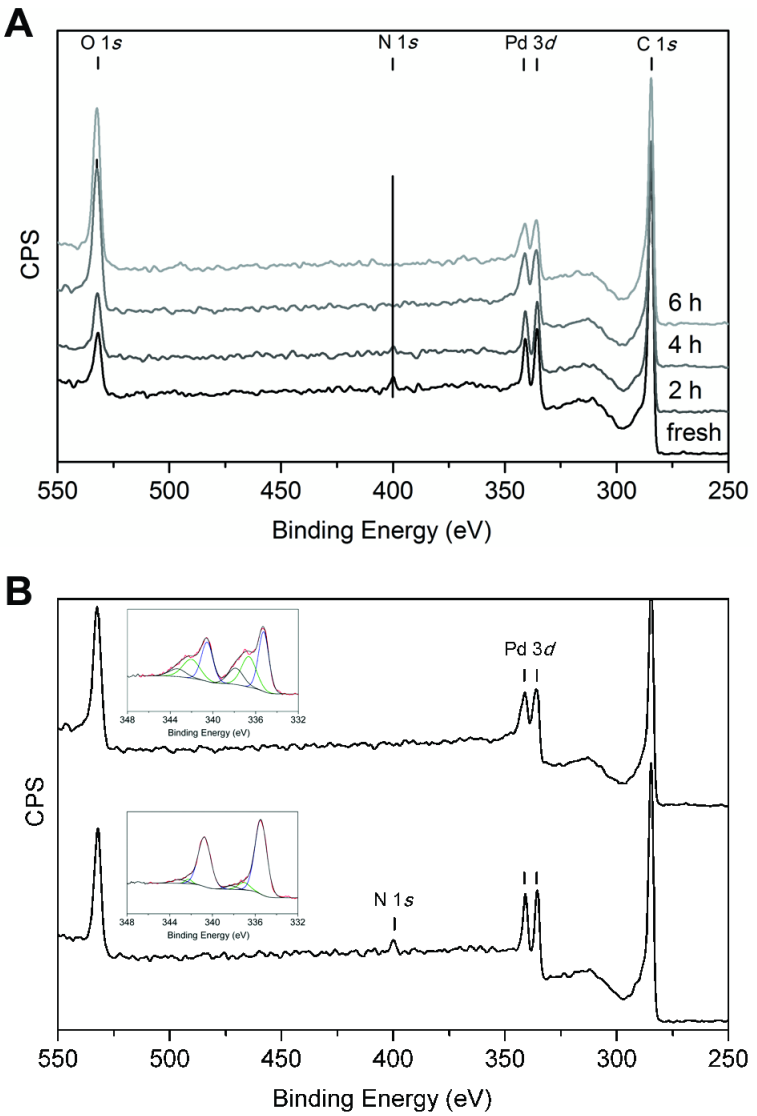

Figure 7.8: A) General XPS survey scans of the fresh catalyst as well as after 2, 4 and 6 h of UVO treatment; B) General XPS survey scans of the supported nanocubes after 4 h of UVO treatment of the side facing away from the UVO lamp (bottom trace) and facing towards the UVO lamp (top trace). The insets correspond to high-resolution scans of the Pd $3d$ region.

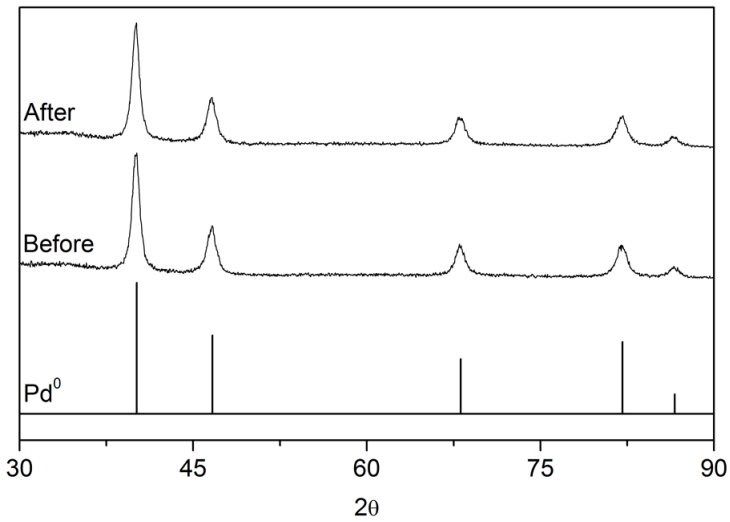

Figure 7.9: XRD spectra of Pd black before and after a 6 h UVO treatment.

chemisorption of oxygen and not to the formation of bulk PdO. Studies on the growth mechanism of PdO nanoparticles showed that the morphology of the nanoparticles was unaltered under 1 bar of O_2 at relatively high temperatures [230]. Pd_{100} and Pd_{111} were found to form a simple (2x2) oxygen overlayer when exposed to molecular oxygen at room temperature [231]. Furthermore, the absence of morphological changes on the nanoparticles after treatment (Figure 7.7) suggest that no bulk PdO was formed, since it is known that, due to high lattice parameter differences, its growth induces cracking and disintegration of the metallic surface [230, 232].

In order to verify this hypothesis, XRD coupled with XPS measurements were performed on Pd black powder both in its fresh state and after 6 h of UVO treatment. Pd black was chosen over the nanocubes due to the weak XRD signals obtained with the latter. XRD measurements showed the exclusive presence of metallic Pd on both fresh and treated samples (Figure 7.9), whereas XPS detected an increase of 20% in the amount of $Pd^{\delta+}$thus confirming the passivating effect of UVO treatment. The catalyst was finally treated in hydrogen at 393 K for half an hour and the relative amounts of $Pd(0)/Pd^{\delta+}$ were found to reverse to those found in the fresh catalyst.

Support characterization

It is also important to study the effect of the UVO treatment on the CNF/SMF support, since it might change the surface chemistry of the latter. The nature of the oxygen groups present on the surface of the CNF can be studied with XPS. Carbon atoms differ in their binding energy if they're bonded to an oxygen atom (phenols, ethers, carbonyl groups) or to two oxygen atoms (carboxyl and lactone groups) [161]. Their corresponding signals appear as satellites on the high binding energy side of the main C $1s$ peak, as shown in Figure 7.10. The C $1s$ spectra can be resolved into six individual component peaks representing carbidic carbon (Peak I), graphitic carbon (Peak II), phenol or ether groups (Peak III), carbonyl groups (Peak IV), carboxyl or ester groups (Peak V) and shake-up satellite peaks due to $\pi - \pi*$ transitions in aromatic rings (Peak VI). The corresponding binding energies at which these peaks appear can be found elsewhere [212,213].

It can be seen that there's already a significant amount of oxygen-coordinated carbon in the as-prepared support (Figure 7.10a), although the vast majority correspond to phenol, ether and carbonyl groups, which are weakly acidic to neutral in nature. A common way of decreasing the hydrophobicity of as-prepared CNF is by deliberately adding oxygenated surface groups by treating them in boiling hydrogen peroxide (Figure 7.10b). Following activation, the amount of graphitic carbon diminishes sensibly, mainly in favor of carboxylic groups, which are strongly acidic. It can be seen that a 4 h treatment under UVO (Figure 7.10c) also increases the relative amount of carboxylic groups on the surface of CNF. Furthermore, the I_O/I_C ratio was found to be an order of magnitude lower in as-prepared CNF as compared to H_2O_2-activated/UVO-treated CNF, suggesting that the absolute amount of oxygen-containing groups is significantly increased by the treatment. Finally, the deposition of PVP-stabilized Pd nanoparticles (Figure 7.10d) does not seem to affect the relative amount of the different functionalities. It can be thus concluded that UVO-treatment increases the acidity of CNF.

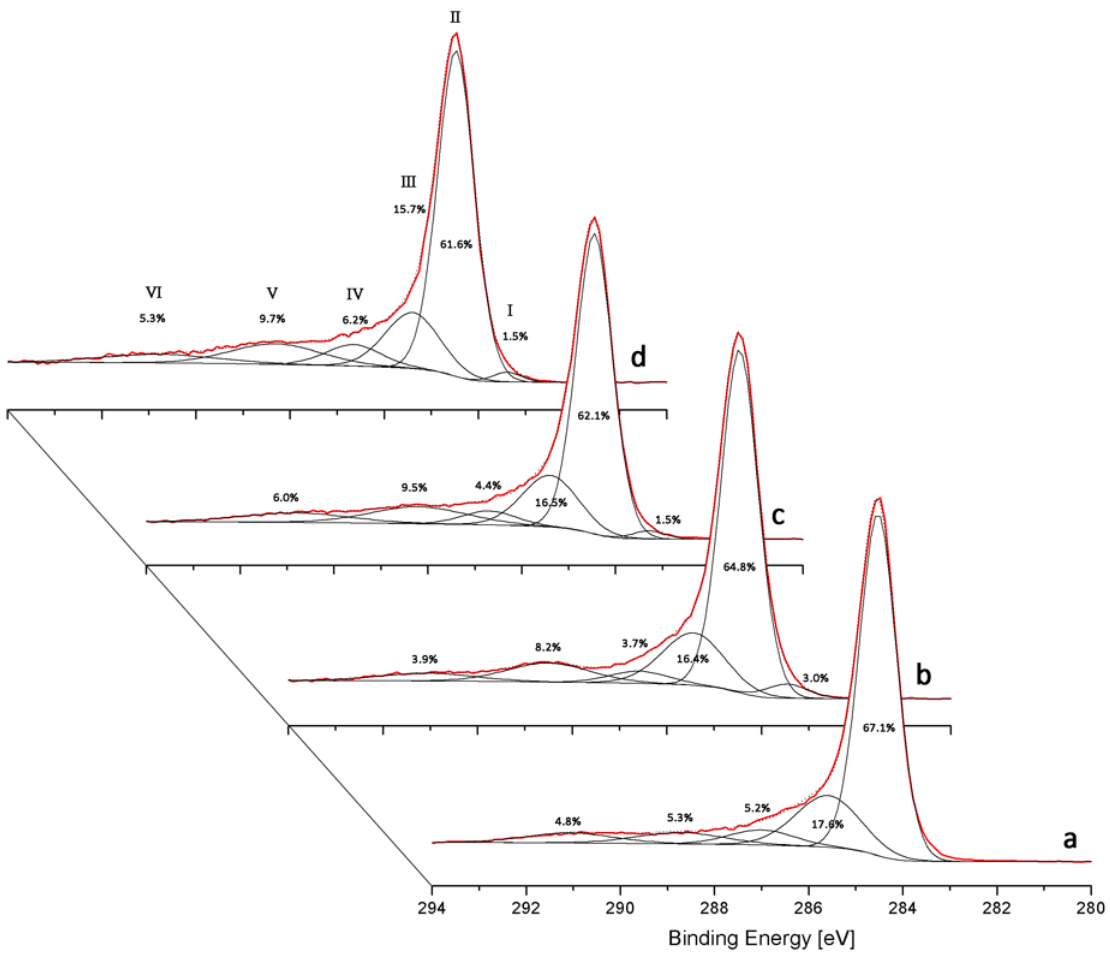

Figure 7.10: High resolution XPS C 1*s* spectra of CNF a) as prepared, b) after 4 h in boiling H_2O_2, c) after 4 h of UVO treatment and d) after the deposition of the Pd nanocubes.

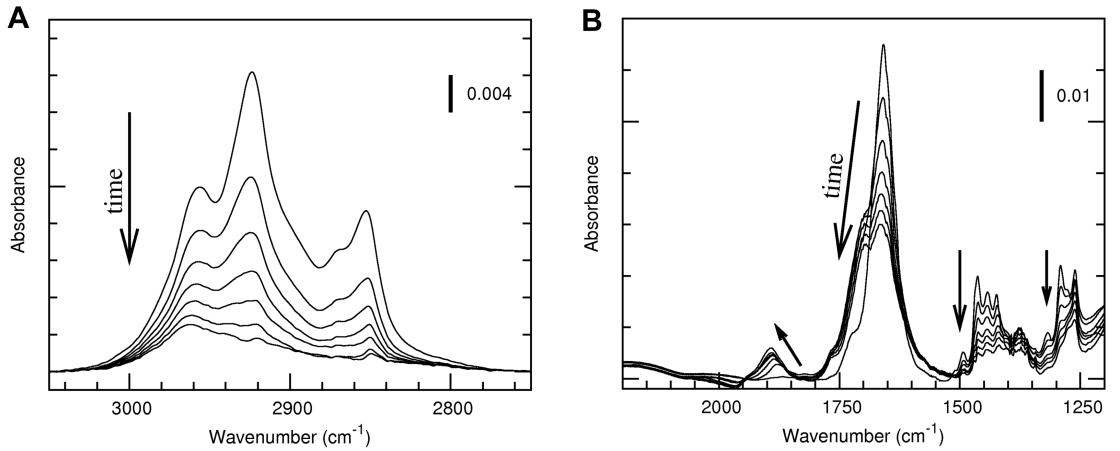

Figure 7.11: ATR-IR spectra of PVP/Pd nanocubes under UVO treatment at 0, 5, 10, 15, 20, 25 and 30 min: C-H A) stretching and B) fingerprint regions.

7.3.3 *In-situ* characterization by ATR-IR

The kinetics of PVP removal by UVO cleaning was followed by *in-situ* ATR-IR spectroscopy. The details of PVP IR bands assignment in a similar system (PVP on Pt) can be found elsewhere [233]. The evolution of the IR spectra during the first 30 min of treatment in the range of the C-H stretching and fingerprint region are given in Figure 7.11A and B, respectively.

A fast and homogeneous decrease of the concentration of the molecules involving the C-H stretching vibration (Figure 7.11A), as well as most of the PVP vibrations (Figure 7.11B), was observed. The decrease in the IR signal results from the elimination of PVP, the two most noticeable exceptions being the rising IR signal between 1850 and 1950 cm^{-1} and the change in the shape of the carbonyl stretching band in the range of 1600-1800 cm^{-1} during the first 5 min of UVO treatment. The C=O stretch of PVP is especially sensitive to the molecular environment, and the shift could indicate a change in the structure of PVP itself, in the interaction between the metal nanoparticles and PVP, or in the hydrogen-bond network. The rising signal at around 1900 cm^{-1} probably corresponds to carbon monoxide, a product of the decomposition of the PVP by UVO that is known to have a

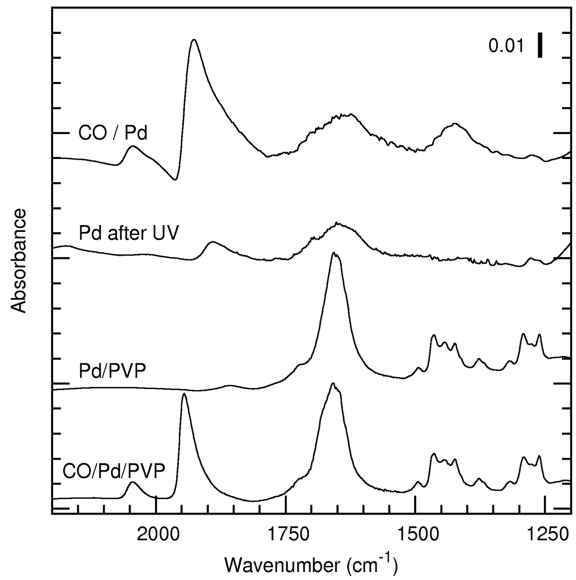

Figure 7.12: ATR-IR spectra of Pd nanocubes before and after UVO treatment (3 h) under N_2 or CO atmosphere (Spectra have been offset for clarity reasons).

high affinity for Pd [234]. Furthermore, Borodko et al. also found CO absorbed on Pt while studying the thermal decomposition of PVP on Pt [233].

In order to validate the assignment of the band to CO adsorbed on Pd, ATR-IR spectra of PVP/Pd and Pd nanoparticles (after UVO treatment) are shown on Figure 7.12. After 3 h of UVO treatment, PVP was removed and only a few bands (1900 and 1650 cm^{-1}) are still visible. The broad signal rising at 1650 cm^{-1} typically corresponds to the water bending mode. The addition of CO over Pd leads to two positives bands at 1930 and 2045 cm^{-1} preceded by two negative signals at higher wavenumbers. The presence of negative bands is an anomalous effect which is well known in IR spectroscopy for such thin and irregular metallic samples [235]. A similar experiment of CO on Pd particles before UVO treatment also confirmed the two CO absorption modes on Pd/PVP nanocubes. The two signals correspond to CO molecules adsorbed onto Pd in a linear (on-top) and bridged configuration at 2045 and 1930 cm^{-1}, respectively, in accordance with the literature available on CO absorption on Pd stabilized by PVP [236]. The shift between the CO signal

at 1900 cm^{-1} after UVO treatment, and the signal at 1930 cm^{-1} can be explained by the increase of the concentration of CO adsorbed on the surface of Pd [234].

An interesting feature was observed when comparing the rate of PVP depletion with ATR-IR spectroscopy between pure PVP and the PVP surrounding the nanoparticles. Figure 7.13 shows the evolution of the IR spectra in the C-H fingerprint region (1800-1000 cm^{-1}). The strongest infrared signal (1750 and 1600 cm^{-1}) corresponds to an overlapping of many molecular vibrations: C=O and C-N stretching as well as amide and water bending modes. The details of PVP IR bands assignment in a similar system (PVP on Pt) can be found elsewhere [233]. A fast and homogeneous decrease of the concentration of most of the PVP vibrations can be observed in both cases, analogously to the findings shown in Figure 7.11. In this case, however, the same spectra was recorded when PVP alone (Figure 7.13B) was subjected to UVO cleaning than when the PVP-stabilized nanoparticles (Figure 7.13A) were exposed to the UV lamp. This seems to suggest that the presence of Pd nanoparticles embedded in the PVP matrix did not interfere with the cleaning process, although they were passivated after being exposed to UVO.

7.4 Catalytic behavior of UVO treated Pd nanoparticles

7.4.1 Effect of UVO cleaning on Pd nanocubes: acetylene hydrogenation

TOF increased fourfold after the UVO treatment (catalysts A and B), suggesting that the stabilizing agent partially blocked the active sites of the nanoparticles as seen in Table 7.1. This trend had already been observed in the hydrogenation of ethylene over nanoparticles stabilized by tetradecyltrimethylammonium bromide (TTAB) and PVP and it could be attributed to a weaker interaction of TTAB with metal surfaces [190]. Nevertheless, PVP-stabilized Pd nanocubes were found to be twice as active when supported on UVO-treated CNF/SMF supports. This result suggests that the increase in activity observed in catalyst

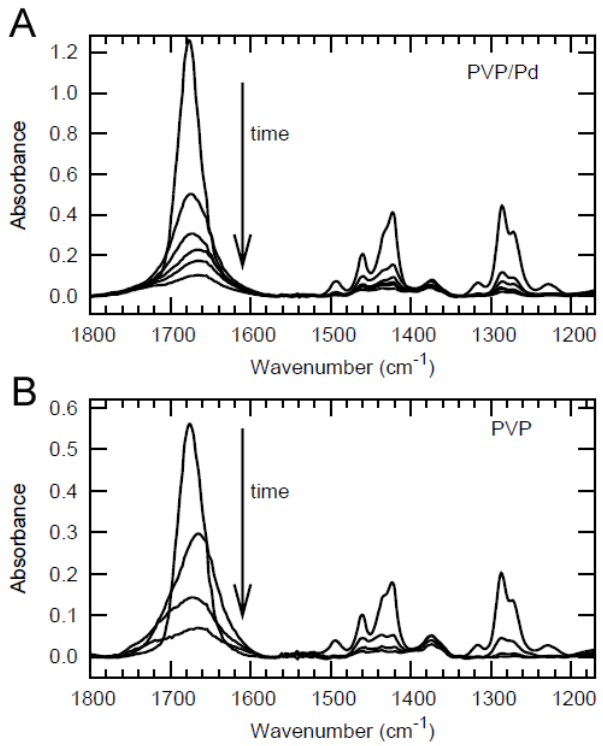

Figure 7.13: ATR-IR spectra showing the influence of the presence of Pd in the rate of PVP decomposition with UVO cleaning from 0 to 10 h of treatment. A) Pd/PVP and B) PVP.

Table 7.1: Summary of the catalysts used in this study and catalytic results[a].

Catalyst	% Pd[b]	CNF oxidized	PVP removed	TOF [s^{-1}]	Deactivation [%][c]
A	0.48	No	No	94.7 ± 2.5	5.0
B	0.10	Yes	Yes	359.9 ± 9.1	15.5
C	0.48	Yes	No	188.8 ± 4.8	12.9

[a] Reaction conditions: 393 K, $C_2H_2 : H_2 : Ar$ = 1.2:20:78.8, 25% conversion.
[b] Percentage expressed with respect to the amount of CNF.
[c] Expressed as percentage of initial activity lost in 3.5 h on stream.

B was probably partially due to the modification of the support during UVO treatment.

It is known that the reaction conditions during the stabilization of the catalyst may have a large effect on the composition and morphology of the carbonaceous layer on Pd and on the kinetic properties of the catalyst under steady state [3, 79, 237]. The nature of the support could thus influence the catalytic behavior when its surface chemistry is modified [238]. The influence of support acidity was studied with the preparation of a third catalyst (catalyst C). In this case, the support was pre-treated for 4 h under UVO and the PVP-stabilized Pd nanocubes were subsequently deposed on it. Table 7.1 summarizes the preparation procedure for the catalysts tested in the hydrogenation of acetylene.

Although selectivity was not significantly influenced by the treatment, green oil formation was slightly favored in the UVO-treated samples, despite the fact that CO is formed and adsorbs on palladium during the decomposition of PVP, as seen by in-situ IR measurements. It is nonetheless worth noting that although carbon monoxide is frequently used to increase the selectivity towards ethyne [237], the amount adsorbed is clearly far from saturation as it can be seen in Figure 7.12. Furthermore, CO was found to desorb from Pd much faster in the presence of acetylene [239–241]. Then, this effect probably arises from the change in support acidity after UVO. Indeed, increased support acidity was found to reduce the yield of olefin in the hydrogenation of acetylene [242], propyne [243], and 1,3-butadiene [244].

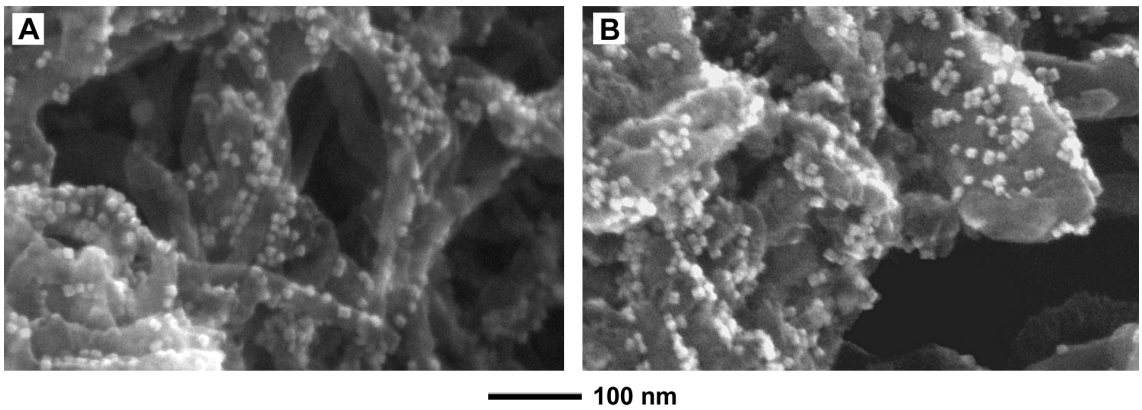

Figure 7.14: SEM images of the (A) fresh supported nanocubes and (B) after 10 h on stream. Reaction conditions: 393 K, $C_2H_2 : H_2 : Ar = 1.2{:}20{:}78.8$, 25% conversion.

Whereas the non-treated catalyst (A) was fairly stable, with a decrease of only 5% of the initial activity after 3.5 h on stream, catalysts B and C deactivated much more quickly, although the catalyst that deactivated the most (14.5% of initial activity in 3.5 h) was the UVO-treated (catalyst B). There seems to be a correlation between support acidity and deactivation, as already reported in the literature [243]. This deactivation probably arises from a slight increase in the formation of green oil in catalysts B and C resulting from the increased acidity of the support. In all cases the behavior of the PVP-stabilized nanocubes on UVO-treated CNF (catalyst C) was intermediate to that of the PVP-stabilized nanocubes (catalyst A) and the UVO-treated nanocubes (catalyst B).

A frequent problem encountered when working with shape-tailored nanoparticles is their morphological instability, especially when the reaction is carried out in colloidal solution [10, 113, 118] due to the strong dependence of interfacial free energy density on temperature and on the presence of adsorbed molecule on the surface of a nanocrystal [245]. However, the support seemed to grant high morphological stability to the nanocubes, which retained their shape and distribution even after 10 h on stream (Figure 7.14).

7.5 Conclusions

PVP-stabilized Pd nanocubes, a thermodynamically unfavorable shape, were synthesized, deposited on CNF/SMF supports and treated with UVO in order to eliminate the trace amount of stabilizing agent still present on its surface. Ex-situ XPS analyses showed that N from PVP was already undetectable after 4 h under UVO cleaning. The surface of the Pd nanocubes was found to passivate after the UVO treatment, but no bulk PdO phase was formed on the basis of XRD measurements. Furthermore, the treatment was found to increase the number of oxygen-containing groups present on the surface of the CNF/SMF support, thus changing its acid/base properties. In-situ ATR-IR analysis showed that there was a homogeneous decrease of most PVP vibrations. CO was found to be generated from the decomposition of PVP and to adsorb on the surface of Pd although the coverage was far from saturation. High-resolution SEM imaging showed a remarkable morphological stability of the nanocubes even after 6 h of UVO treatment.

The catalyst was tested in the hydrogenation of acetylene. The removal of PVP increased the activity of the catalyst fourfold and selectivity was mainly unaltered, although a slight increase in green oil formation was observed. The nanocubes were found to be morphologically stable under the reaction conditions used.

The method described herein was used for treating supported nanoparticles of other common *fcc* shapes, which expose different types of crystal planes, in order to study the structure sensitivity of the hydrogenation of acetylene. This would allow the rational design of a catalyst from nano to micro-scale.

Chapter 8

Supported Pd nanoparticles for C_2H_2 hydrogenation

In this chapter, the PVP-stabilized nanoparticles studied in Chapter 4 were supported on structured SMF-based supports. After PVP removal following the procedure shown in Chapter 7, the catalysts were tested in the selective hydrogenation of acetylene. The model developed in Chapter 4 involving two types of active sites was applied and used to study the structure sensitivity of the reaction. Furthermore, a long-term stability test allowed to assess the morphological stability of the nanoparticles. Lastly, the effect of the type of support was studied and ZnO was found to show an interesting synergy with the active phase.

This chapter is based on the following publication:

M. Crespo-Quesada, C. Voisard, A. Yarulin, Y. Xia and L. Kiwi-Minsker. Shape and Size-Tailored Supported Pd Nanoparticles in the Hydrogenation of Acetylene. In preparation.

8.1 Introduction

8.1.1 Context

A step further in the complexity ladder of rational catalyst design, lies the micro-scale level, in which all factors previously studied are taken into account and where the chemical nature as well as microstructure of the support are now included in the equation.

Most structure sensitivity studies, particularly involving shape-tailored nanoparticles, are conducted in colloidal form [38, 39]. Indeed, there is only a handfull of examples in the literature dealing with structure sensitivity on supported systems [55–57], and even in those cases, only a subset takes all levels of complexity into account when interpreting the results [56]. Indeed, using unsupported well-defined Pd nanoparticles were proved to be an invaluable path towards unveiling the reaction mechanism on the active phase of chemical reactions (see Chapter 4). However, for most catalytic applications, Pd nanoparticles are immobilized on supports of different kinds.

This chapter tries to combine all the tools developed throughout the thesis in order to study the structure sensitivity of acetylene hydrogenation over relatively complex catalysts. The elimination of PVP from supported Pd nanoparticles through the technique shown in Chapter 7 allows one to study the catalytic behavior at a nano-scale level on "clean" metallic surfaces. The application of the model developed in Chapter 4 to this system permitted the study and rationalization of the structure sensitivity of the hydrogenation of acetylene. Long term testing showed that the morphology of the supported nanoparticles was stable only during the first 10-15 h, but that surface recombination took place from that point onwards. Finally, the same nanoparticles were deposited onto ZnO-coated SMF structured supports in order to elucidate the effect of the nature of the support on the catalytic behavior of the final catalyst.

8.1.2 Experimental details

Catalyst preparation

The shape-tailored PVP-stabilized nanoparticles were prepared following the procedures presented in Section 3.1.1. The composite CNF/$SMF_{Inconel}$ and ZnO/$SMF_{FeCrAlloy}$ supports were prepared following the procedures presented in Section 3.2.1.

Nanoparticle immobilization The Pd nanoparticles were subsequently immobilized onto either one of the supports following two different impregnation procedures.

Incipient wetness impregnation (IWI) This method involved impregnating the supports directly with the nanoparticle solution in a drop-wise manner until saturation. They were then dried under vacuum at 333 K overnight.

Modified incipient wetness impregnation (MIWI) This method, on the other hand, involved diluting an appropriate amount of the nanoparticle solution in 50 mL of ethanol and sonicating for 5 min prior to plunging the support in the solution. The support was thus kept in contact with this solution under stirring for 5 h, after which it was removed and dried under vacuum at 333 K overnight.

PVP removal through UVO cleaning PVP was removed from the surface of the catalyst through UVO cleaning following the protocol developed in Chapter 7. Each disc was kept under the UV source for 8 h on each side.

Catalyst characterization

Pd concentration was determined by AAS. Surface characterization of the nanoparticles as well as the support was performed with XPS. The nano and micro-morphology of the

catalysts was examined with HRSEM and TEM. Detailed descriptions of the apparatus used and conditions applied to perform all these analyses can be found in Section 3.5.

Hydrogenation experiments

The hydrogenation of acetylene was carried out in the jacketed differential tubular reactor described in Section 3.4.2. The experimental procedure as well as the calculations made can be found in the same section.

8.2 Nanoparticle immobilization

8.2.1 Pd nanoparticles

Figures 4.1 shows TEM images of the nanoparticles used in this chapter. All samples were monodispersed (see Figure 4.3) and monocrystalline. Either Pd_{100} (Figure 4.1A, B and C), Pd_{111} (Figure 4.1D) or a mixture of both (Figure 4.1E) were present on their surfaces (see Figure 4.2 and Figure 7.4 for HRTEM images and FTT diffraction patterns).

8.2.2 ZnO/$SMF_{FeCrAlloy}$ support

The morphology of the CNF/$SMF_{Inconel}$ supports was already shown in Section 6.2.1. ZnO/$SMF_{FeCrAlloy}$ supports were also prepared and used to deposit the shape-tailored Pd nanoparticles. Figure 8.1 shows SEM images of the composite structured support, where it can be appreciated that the coating is homogeneous and uniformly covers all the surface of the fibers. Furthermore, the island-like arrangement of the hexagonal PdZn crystals is also easily discernible.

8.2.3 Incipient wetness impregnation (IWI)

Many methods have been presented in the literature regarding the immobilization of metal nanoparticles [246]. Given the characteristics of the colloidal solutions used and the sup-

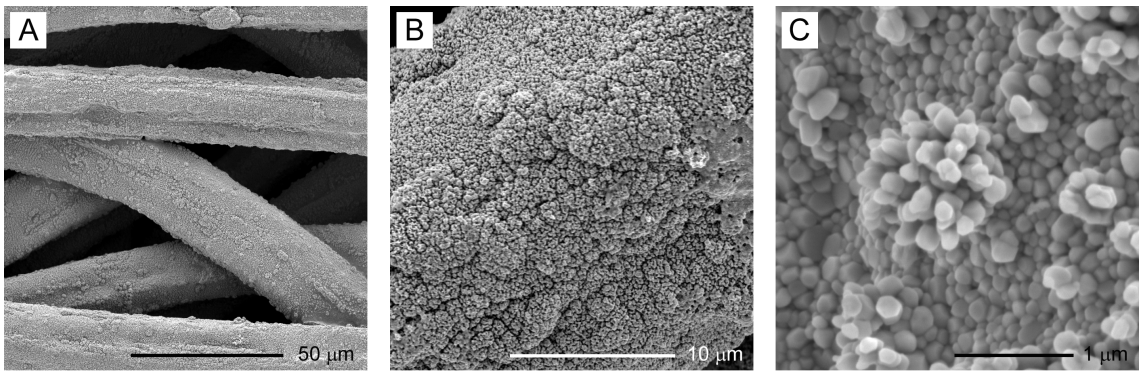

Figure 8.1: SEM images of the ZnO/$SMF_{FeCrAlloy}$ supports with increasing detail. A) General overview of SMF fibers coated with a uniform layer of ZnO, B) detail of the surface of a single SMF where the "island-like" structure of the ZnO layer can be appreciated and C) close-up view of the ZnO layer where the hexagonal ZnO crystals can be observed.

ports available, incipient wetness impregnation (IWI) seemed the most straightforward method. In this method the active metal is present in an aqueous or organic solution. Then the metal-containing solution is contacted with a support and capillary action draws the solution into the pores of the latter. The catalyst can then be dried to drive off the volatile components within the solution, depositing the metal on the catalyst surface.

In this particular case, the support was not plunged into the solution. The Pd-nanoparticle containing ethanol solution was cast-dropped directly onto the support until saturation of the latter. This method allowed optimizing the amount of solution used for each impregnation.

Figure 8.2 shows HRSEM images of the supported nanoparticles. The smaller nanoparticles (Figure 8.2A, B and E) were successfully immobilized using this technique. CUB18 and OCT, however, formed large aggregates that could in some cases reach several hundreds of nanometers in size (Figure 8.2C and D).

8.2.4 Modified incipient wetness impregnation (MIWI)

An alternative method was then employed in order to try dispersing the large nanoparticles evenly and scatteredly throughout the support. Since it was known that these nanopar-

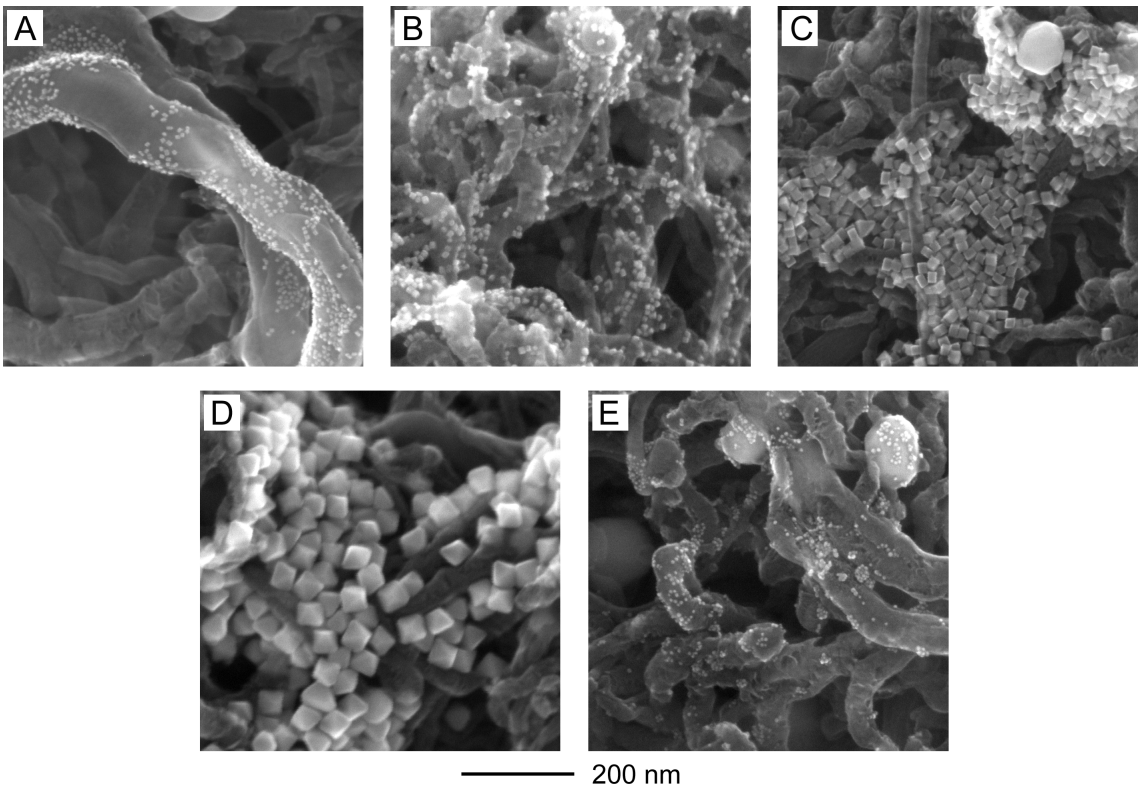

Figure 8.2: HRSEM images of the PVP-stabilized Pd nanocrystals after immobilization on CNF/$SMF_{Inconel}$ supports through the incipient wetness impregnation (IWI) method. A) CUB6, B) CUB10, C) CUB18, D) OCT and E) COT.

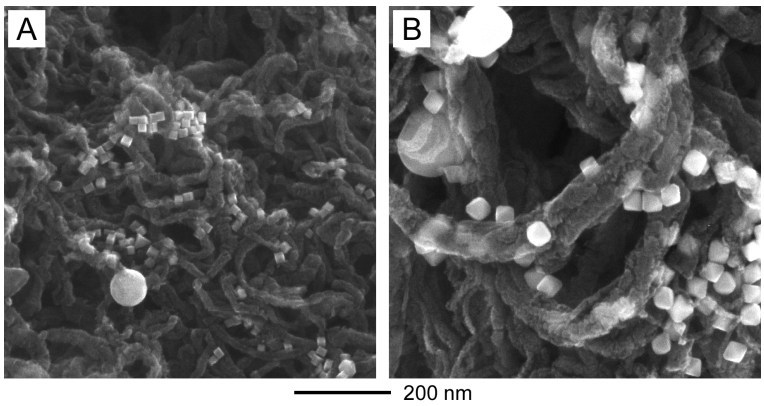

Figure 8.3: HRSEM images of the large PVP-stabilized Pd nanocrystals after immobilization on CNF/SMF$_{\text{Inconel}}$ supports through the modified incipient wetness impregnation (MIWI) method. A) CUB18 and B) OCT.

ticles could be well dispersed when in a diluted solution, a modified incipient wetness impregnation (MIWI) technique was applied. In this case, a diluted solution of nanoparticles was first sonicated and then the support was contacted with it under stirring for a given amount of time.

Figure 8.3A and B show the resulting catalysts obtained when immobilizing the nanoparticles with the MIWI technique. It is possible to see that the dispersion improved remarkably, and no large aggregates were observed under HRSEM analysis. The result, however, was still not satisfying for catalytic testing, since agglomeration might lead to an effective metal dispersion lower than that predicted by the sole shape and size of the nanoparticles, thus conveying the impression that they were less active than expected.

Although these catalysts were deemed unfit for catalytic testing and structure sensitivity assessment, they were still considered useful for morphology stability studies, since their larger sizes rendered the HRSEM imaging an easier task to perform.

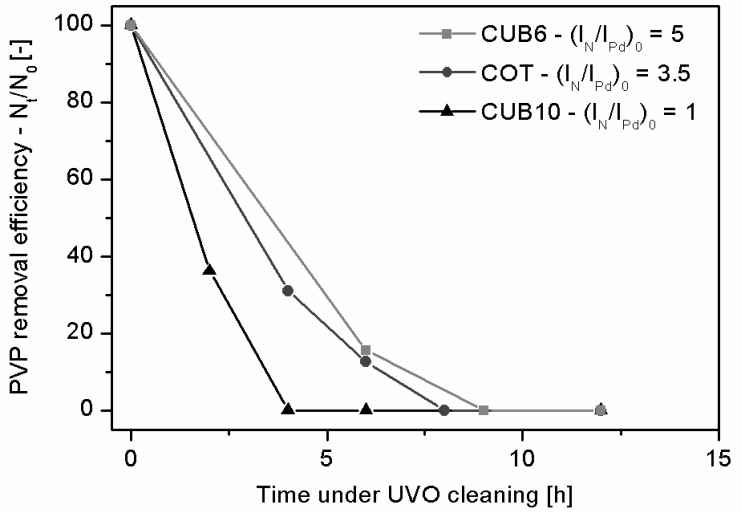

Figure 8.4: Efficiency of the UVO cleaning process for CUB6, CUB10 and COT samples as estimated from XPS surface analysis.

8.3 Elimination of PVP through UVO cleaning

In order to study the structure sensitivity of the hydrogenation of acetylene over PVP-free crystal planes, the catalysts were subjected to UVO cleaning as presented in Chapter 7. The cleaning process was followed with XPS.

PVP removal through N depletion observed through XPS can be observed in Figure 8.4. It can be seen that the rate of PVP removal depended on it initial amount. Nevertheless, the same mechanism seems to take place in all cases, with a fast depletion at the beginning of the process followed by a slower cleaning rate step. 8 h were necessary to render N non detectable by XPS in the slowest case scenario. Since UVO cleaning also excerts an influence on the support as seen in Figure 7.10, and in order to ensure that the observed catalytic response corresponded to the Pd nanoparticles and not to a support effect, all catalysts were treated for 8 h on both sides.

8.4 Structure sensitivity of acetylene hydrogenation

8.4.1 Kinetic regime verification

Before comparing catalyst performances, it is necessary to verify whether the system operates under the kinetic regime. The calculations were performed for the COT nanoparticles, which were the most active, in order to ensure that all other catalysts also operate under kinetic regime.

There are a number of ways of evaluating the influence of mass-transfer in a catalytic reaction. In this case, Madon-Boudart's test was applied [247], since meeting its requirements is particularly easy with the catalysts used and it rules out any kind of mass-transfer influences with as little as a few catalytic runs.

This test involves changing the concentration of active metal by changing its loading but maintaining the same or nearly the same dispersion. Absence of mass transport influences is established by the constancy of reaction rates. In other words, the reaction rate in the kinetic regime is directly proportional to the concentration of exposed metal atoms on the support particle. Thus, for a catalytic reaction:

$$r = k\eta g\left(C_s\right) \tag{8.1}$$

$$k \propto C_{am} \tag{8.2}$$

$$\phi = \frac{V_c}{S_c}\sqrt{\frac{kg\left(C_s\right)}{D_e C_s}} \tag{8.3}$$

where $g(C_s)$ is the concentration function in the rate expression, η the effectiveness factor and C_{am} is the concentration of the active metal. Equation 8.1 indicates that the observed rate is dependent on the effectiveness factor which in turn depends on Thiele's

modulus defined in Equation 8.3. Equation 8.2 is characteristic of heterogeneous catalytic reactions taking place under kinetic regime.

The effectiveness factor and Thiele's modulus relate in the following way:

$$\eta = \phi^p \tag{8.4}$$

which derives, after substituting and rearranging in:

$$r \propto C_{am}^{1+(p/2)} \tag{8.5}$$

In this way, s is the slope obtained when plotting ln r against $\ln C_{am}$. Thus, in absence of mass-transfer limitations, a ln-ln plot of the activity versus the surface metal atom concentration will exhibit a linear correlation with a slope of unity given that in the kinetic regime $\eta \to 1$, then $p \to 0$ and, as a result, $s \to 1$.

When severe instances of pore diffusion control appear, Thiele's modulus is large and $\eta = 1/\phi$, so $p = -1$ and $s = 0.5$.

These results show that if the ln-ln relationship between activity and the active material concentration is plotted, a slope of unity proves the absence of all kinds of mass transfer limitations.

Figure 8.5 shows Madon-Boudart's test performed on COT nanoparticles. A linear fit of the experimental points yielded the following equation:

$$ln\, r = 1.66 + 1.01\, ln\, C_{am} \tag{8.6}$$

The slope of one shows that there are no mass transfer artifacts of any kind for this catalyst. Since they were the most active ones, it can be safely assumed that all others will also operate under kinetic regime.

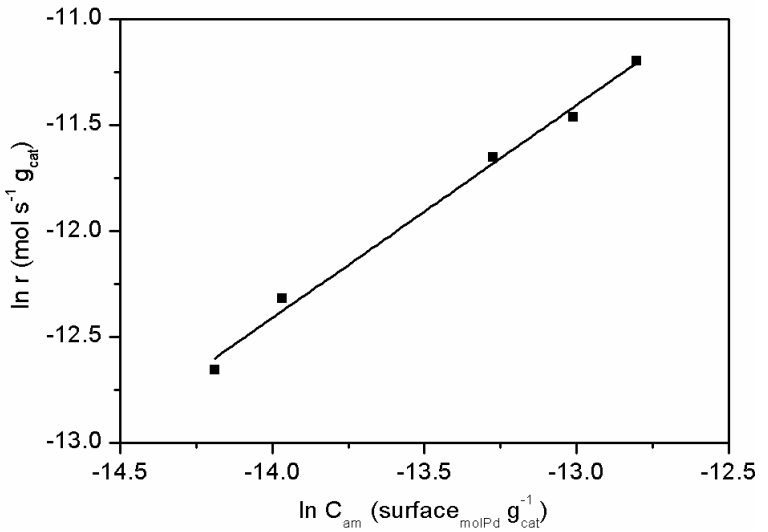

Figure 8.5: Madon-Boudart test for acetylene hydrogenation over COT Pd/CNF/$SMF_{Inconel}$ catalyst at 120 °C ($Ar : C_2H_2 : H_2$ = 78.5:1.5:20, Q_{tot} = 300-1200 ml min^{-1}).

Table 8.1: Surface statistics of the nanoparticles used in this study [20].

Sample	d_p [nm]	D [%]	x_{111} [%]	x_{100} [%]	x_{edge} [%]
CUB6	6	16.7	-	72.1	15.8
CUB10	10	10.7	-	82.1	10.3
COT	5.5	18.3	43.7	5.6	30.3

8.4.2 Catalytic results

CNF supported CUB6 (Figure 8.2A), CUB10 (Figure 8.2B) and COT (Figure 8.2E) were tested in the selective hydrogenation of acetylene under the same reaction conditions. Table 8.1 gathers the surface statistics for these three samples.

These samples allowed determining the effect of size (CUB6 vs. CUB10) as well as shape (CUB6 vs. COT) on this reaction. Figure 8.6 shows the catalytic results obtained.

Concerning the size-effect, it can be observed that the hydrogenation of acetylene shows an antipathetic structure sensitivity, since the observed TOF for CUB10 was higher that that of CUB6. This trend has already been reported in the literature [52,68].

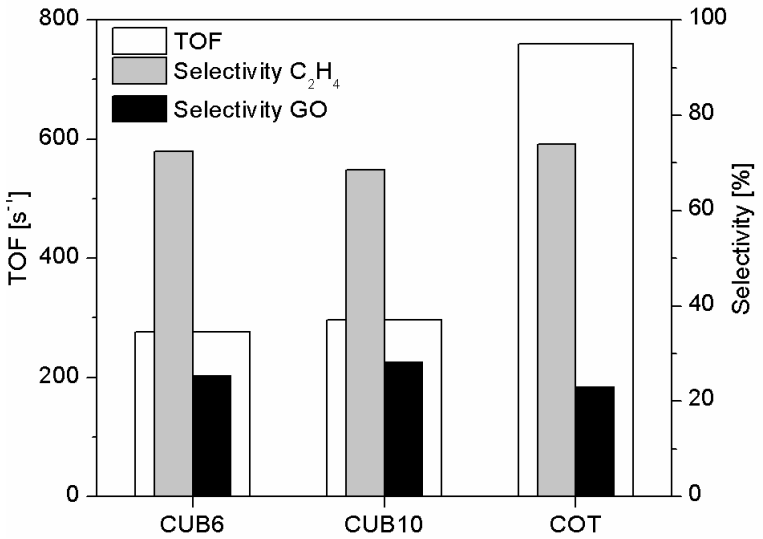

Figure 8.6: Observed TOF and selectivity obtained for CUB6, CUB10 and COT in the selective hydrogenation of acetylene.

Shape-effects, on the other hand, are scarce in the literature. The results presented herein showed cube-octahedral nanoparticles to be considerably more active than cubic ones with a similar dispersion (CUB6 vs. COT). This suggested that Pd_{111} is probably much more active than Pd_{100}.

The model presented in Chapter 4 was thus applied to the results obtained here. It was necessary, however, to consider that each crystallographic plane possessed a different specific TOF, implying that three types of active sites were involved in the catalysis of acetylene hydrogenation. Equation 4.3 can be then rewritten as:

$$TOF_{obs} = TOF_{111} \cdot x_{111} + TOF_{100} \cdot x_{100} + TOF_{edge} \cdot x_{edge} \tag{8.7}$$

Equation 8.7 was first applied to CUB6 and CUB10 samples in order to determine the values for TOF_{100} and TOF_{edge}, which can be found on Table 8.2. It can be seen that Pd_{100} atoms were found to be roughly 4 times more active than edge sites in the hydrogenation of acetylene, analogously to the findings in Chapter 4. These values were subsequently used as starting points for the estimation of TOF_{111} from sample COT (Table 8.2), which

Table 8.2: Catalytic results obtained for the study of the structure sensitivity of acetylene hydrogenation.

Sample	R_Y^a	TOF_{obs} $[s^{-1}]$	TOF_{111} $[s^{-1}]$	TOF_{100} $[s^{-1}]$	TOF_{edge} $[s^{-1}]$	TOF_{est} $[s^{-1}]$
CUB6	46.1	276.0	-	362.7	91.8	276.0
CUB10	31.7	296.3	-	349.7	88.7	296.3
COT	139.1	760.1	1622.7	369.3	100	760.1

[a] Transformation rate of acetylene: $\left[\text{mol} \cdot \text{mol}_{\text{Pd}}^{-1} \cdot \text{s}^{-1}\right]$

yielded a value of 1622.7 s^{-1}, that is around 4.5 times more active than the other type of plane atoms.

The final values for TOF_{111}, TOF_{100} and TOF_{edge} were estimated to be 1622.7±81.1 s^{-1}, 361.5±9.4 s^{-1} and 92.8±4.4 s^{-1}, respectively. This implies that, unlike the hydrogenation of MBY, in the hydrogenation of acetylene shape plays a much more important role on the catalytic behavior of the active phase.

However, this observed structure sensitivity could be an indirect evidence of a different structure-sensitive process: C-laydown deposition in the early stages of the reaction. Indeed, different Pd crystals facets were shown to have different activities in the essential carbon laydown process during alkyne hydrogenations [67]. This layer is thought to prevent the dissolution of hydrogen in the bulk of the nanoparticles, which is known to be too energetic to be selective [248]. Therefore, only surface hydrogen, much less active but more selective is available for reacting. It was however experimentally observed [67], as well as predicted through DFT calculations [249], that carbon diffusion into the bulk of $Pd_{(111)}$ is energetically unfavorable. It can be thus expected the carbon laydown process to be less pronounced on COT nanoparticles as compared to CUB6 and CUB10, which would derive in the observed differences in the activity of each type of plane atom. The large differences in plane atom reactivity between liquid-phase MBY hydrogenation (Chapter 4) and gas-phase acetylene hydrogenation might then come from the absence of PVP on the

surface of the nanoparticles. It could then be speculated that the presence of PVP around the nanoparticles hinders this carbon laydown process, thus rendering both planes equally active.

Selectivity, on the other hand, did not seem to depend on the types of active sites, an thus shape or size (Figure 8.6). This had already been reported in the literature. Indeed, the data available points towards the independence of selectivity on nanoparticle structure [68,69]. The values for the selectivity towards ethylene, ethane and green oil were found to be 71.5±2.8, 3.1±0.3 and 25.5±2.6, respectively. These values are in line with those reported in the literature for Pd catalysts [68,69]. Furthermore, the high selectivity towards green oil is characteristic of acetylene. Indeed, with increasing substitution, the selectivity of oligomers formation decreases due to steric interferences in the C–C bond forming step [3]. The low selectivity towards ethane at 25% conversion suggests that the direct hydrogenation of acetylene towards ethane does not take place. It is thus formed from the over-hydrogenation of ethylene, which is expected to be relatively slow at low conversions. Indeed, the direct hydrogenation towards ethane was found to be a possible, yet negligible reaction [77].

Since selectivity was found to be independent of particle morphology, optimization can then be performed solely based on activity considerations. Therefore, if the specific TOFs obtained for each type of active site are combined with equation 8.7 and the surface statistics for common fcc crystal shapes [20], then predictive curves of TOF can be obtained, as shown in Figure 8.7A.

An obvious shape-effect can be observed, since TOF_{100} was found to be much lower than TOF_{111}. Therefore, cubic nanoparticles, which present (100) crystallographic planes on their surfaces, will be kinetically disfavored with respect to octahedral or tetrahedral nanoparticles, which are bounded by (111) crystal planes. Cube-octahedra lie in between, as expected since their surfaces are characterized by a mixture of both crystal planes. It

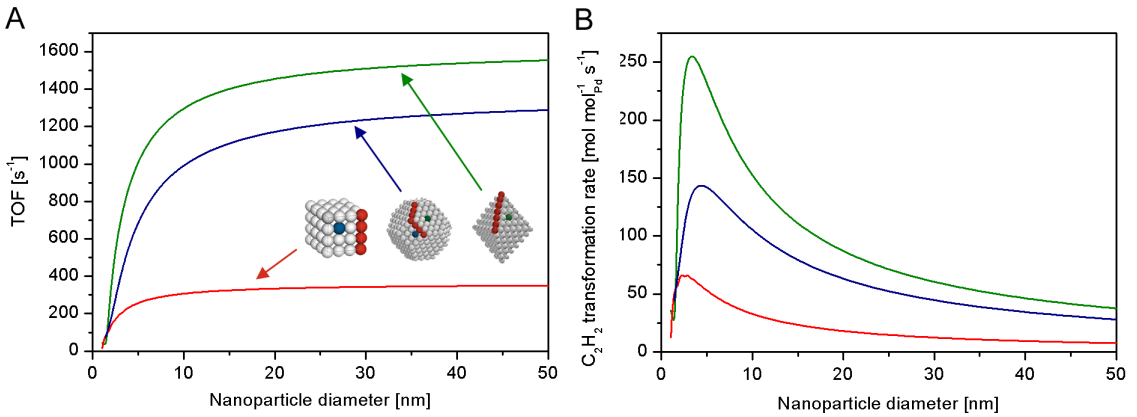

Figure 8.7: Predictive size and shape effect graphs for the selective hydrogenation of acetylene. A) TOF as a function of nanoparticle size and shape and B) C_2H_2 transformation rate as a function of nanoparticle size and shape.

can also be seen that for nanoparticles larger than 20 nm, no size-effects are expected since TOF remains relatively unchanged.

TOF values do not take into account the amount of atoms inside the nanoparticles, which are not involved in the catalysis. It is then possible to express the activity in terms of total amount of Pd required (Figure 8.7B). By doing this, a size optimization can be easily performed, since although large particles have a larger TOF, much valuable Pd will remain unexposed to the reacting molecules. Therefore, is this optimization criterion is used, octahedral Pd nanoparticles become yet more convenient than cube-octahedral, since the latter present very low dispersions. The optimal nanoparticle for this specific application seems then to be octahedral nanoparticles of roughly 5 nm in edge length.

It is worth mentioning that these results are simulated for low conversions (∼25%). In order to assess the influence of nanoparticle morphology on the over-hydrogenation of ethylene towards ethane, similar measurements should be performed at higher conversions. There is, however, the general concensus that the hydrogenation of ethylene is a structure insensitive reaction [67].

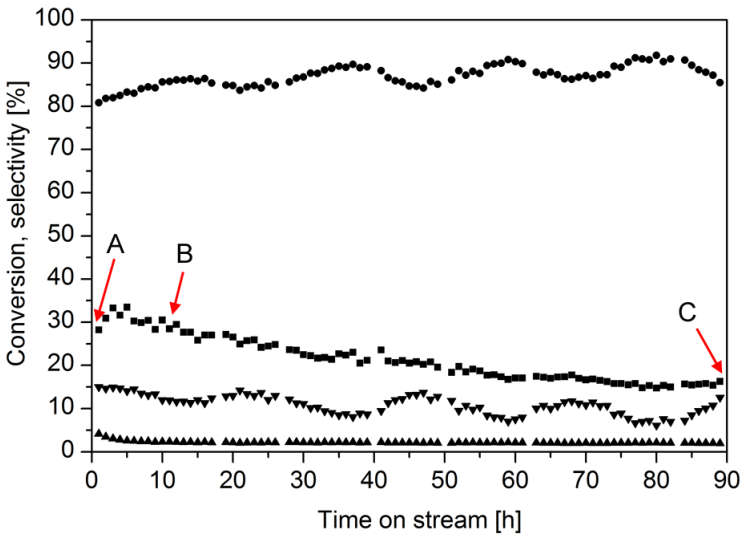

Figure 8.8: Stability test performed on supported CUB18 nanoparticles. A) 0 h, B) 10 h, and C) 90 h on stream.

8.5 Stability test

Nanoparticle morphological stability is an important aspect. In order to study it, CUB18 nanoparticles were immobilized on CNF/$SMF_{Inconel}$ supports and subjected to the same reaction conditions for 90 h.

Figure 8.8 shows the evolution of conversion and selectivity as a function of the time on stream. It can be seen that selectivity towards ethylene remains fairly stable around a mean value varying in 24 h cycles. This is in line with the results shown in Section 8.4.2, where selectivity was shown to be independent of particle morphology. A drop of roughly 10% in conversion was observed after 90 h on stream, which is relatively low as compared to the results found in the literature for other Pd-based catalysts [68].

HRSEM imaging was used in order to assess the morphological evolution of the nanoparticles with time on stream. Figure 8.9 shows three micrographs of the catalyst corresponding to points A, B and C in Figure 8.8, i.e., in its fresh state and after 10 h and 90 h on stream, respectively. Nanoparticle morphology was found to be well maintained after 10 h on stream. On the other hand, Figure 8.9C shows that a thick layer of green oil

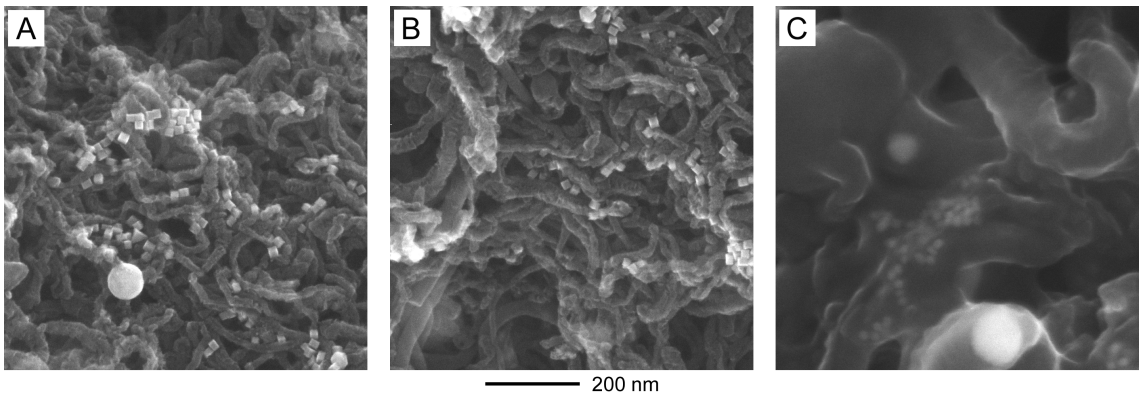

Figure 8.9: HRSEM imaging of supported CUB18 nanoparticles throughout the stability test. Panels A, B and C correspond to the times on stream depicted in Figure 8.8.

deposited and completely covered the catalyst surface after 90 h on stream. Although the nanoparticles could be seen under the layer, it was impossible to observe their shape.

Therefore, the used catalyst was subjected to a 5 min ultrasonic bath in ethanol in order to detach some of the CNF from the SMF support. Figure 8.10 is the result of such procedure. In this case, TEM imaging was able to capture the morphology of the nanoparticles on the CNFs. It can be seen that most of the nanoparticles evolved towards rounded nanoparticles whilst maintaining their size. In some cases the evolution towards cube-octahedral nanoparticles was obvious, as in the two particles encircled in Figure 8.10B.

This allows to speculate that the only reason for catalyst deactivation was the deposition of an ever growing layer of green oil on the surface of the nanoparticles. The fact that the conversion drop was not extreme and that it seemed to stabilize towards the end could be rationalized with the fact that the nanoparticles were evolving towards more active counterparts, showing (111) planes on their surfaces. It would be interesting and not surprising to see an improvement in conversion as nanoparticle evolution continues towards thermodynamically more stable shapes.

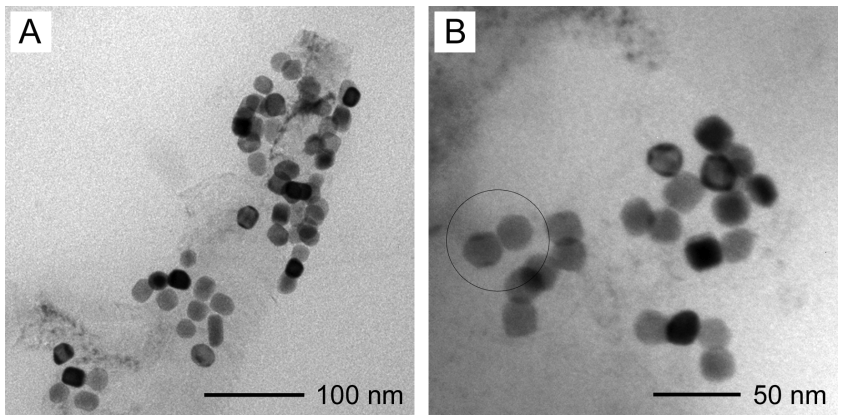

Figure 8.10: TEM images of the supported CUB18 nanoparticles after 90 h on stream. A) Low-magnification image that shows the an individual CNF fiber covered with the aged CUB18 particles and B) High magnification picture where particles having evolved in cube-octahedra can be clearly seen.

8.6 Influence of the support

Supported well-defined Pd nanoparticles can indeed be used to study the structure sensitivity of chemical reactions. The main drawback with respect to their use unsupported lies in the fact that metal-support interactions can modify the true catalytic behavior of the nanoparticles.

In order to test this hypothesis, CUB6 and COT nanoparticles were supported on $ZnO/SMF_{FeCrAlloy}$ discs and tested under the same reaction conditions. Figure 8.11 shows the obtained results.

It can be seen that the Pd nanoparticles deposited on ZnO showed a lower activity coupled with a slight selectivity increase. This trend had already been observed for the hydrogenation of MBY over Pd/ZnO/SMF catalysts [73,74]. The change in catalytic behavior was ascribed to the reducibility of ZnO which allows the formation of an intermetallic PdZn compound on the surface of the catalyst. The formation of this species can be assessed with XPS, as shown in Figure 8.12. A change in the binding energy of Pd(0) was observed before and after the reaction. There is evidence in the literature pointing towards the formation of the PdZn alloy under hydrogen at temperatures as low as 373 K [250].

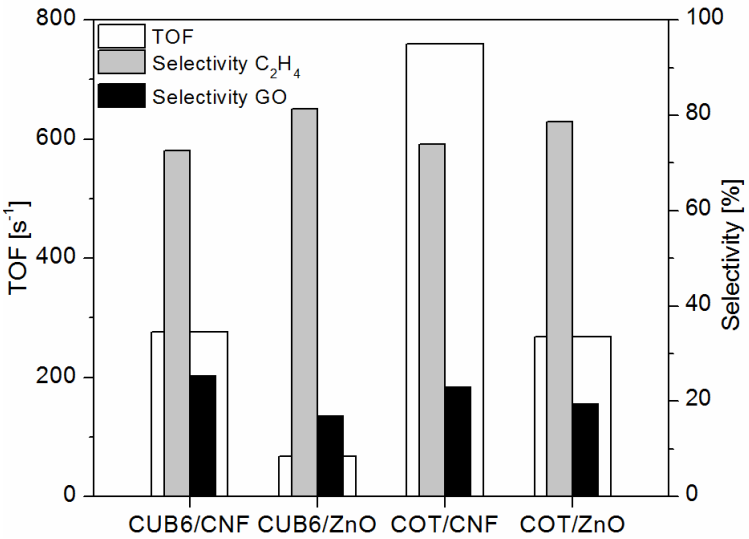

Figure 8.11: Support effect in the hydrogenation of acetylene for CUB6 and COT samples.

A change in the binding energy of metallic Pd of +0.6-1 eV upon alloy formation has been reported in the literature [47, 169–171]. This electron deficient new phase will coordinate much more strongly to electron rich compounds such as alkynes much like edge atoms would do as compared to plane atoms in a metallic nanoparticle.

8.7 Conclusions

Well-defined shape-controlled palladium nanoparticles were successfully immobilized on modified SMF-based supports and tested in the hydrogenation of acetylene. UVO cleaning was used in order to eliminate traces of PVP still present on the surface of the nanoparticles.

The reaction was shown to present an antipathetic structure sensitivity, i.e. TOF increases with particle size. Furthermore, a model analogous to the one developed in Chapter 4 was successfully applied for this reaction. In this case, however, plane atoms behaved differently depending on the crystallographic plane exposed. Pd_{111} was found to be roughly four times more active than Pd_{100}, which, in turn, was 4 times more active than edge atoms. This observed behavior was rationalized with the C-laydown deposition

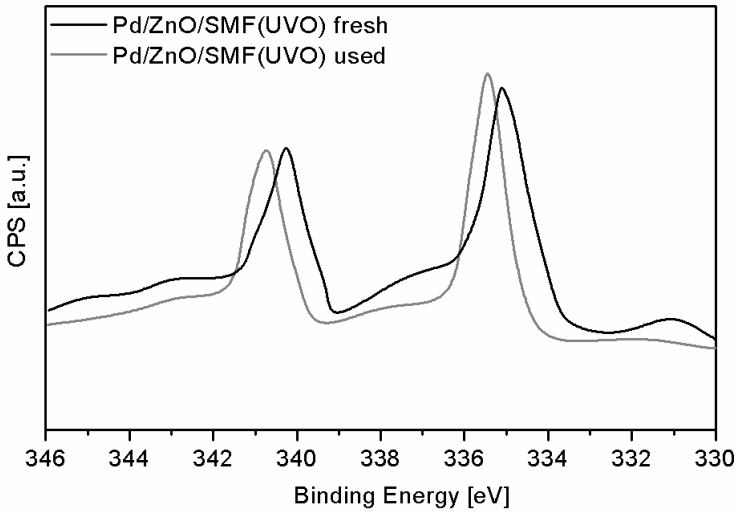

Figure 8.12: High resolution XPS spectra of fresh and used Pd/ZnO/SMF catalysts where a shift towards higher BE for Pd $3d$ can be observed.

process known to happen at the beginning of the reaction. This layer hinders hydrogen dissolution, which diminishes the activity of the hydrogenation of acetylene. This phenomenon is known to be disfavored on Pd_{111} surfaces, leading to the increased activity shown from this plane. Selectivity, on the other hand, was not influenced by nanoparticle morphology. Catalyst optimization allowed predicting that octahedra of 5 nm would be the most active shape for this particular application.

Cubic nanoparticles subjected to 90 h on stream showed surface stability for at least 10 h, but their shape was lost after 90 h on stream. Catalyst deactivation was due to green oil deposition on the catalyst's surface, which was counterbalanced by the increase of activity expected for nanoparticles bounded predominantly by Pd_{111} planes.

ZnO-coated SMF structured supports were used to perform the same reaction in order to elucidate the effect of the support on the catalytic performance. As it had been observed previously in our group, Pd/ZnO/SMF catalysts were less active and slightly more selective than the Pd/CNF/SMF counterparts. This could be rationalized on the basis of the formation of an intermetallic PdZn phase with modified adsorption properties.

Chapter 9

Concluding remarks and outlook

9.1 Conclusions

The **main objective** set for this thesis was the **rational design** of a Pd-based catalyst for triple carbon-carbon bond hydrogenations. In order to achieve this goal, a multi level integrated approach was applied ranging from the nano-scale design of the active sites to the micro-scale design of the supported Pd nanoparticles including metal-additive and metal-support interactions as well as mass and heat transfer phenomena.

Nano-scale rational catalyst design

In order to rationally design a catalyst's active site, several methodologies have been hitherto applied. Chapter 4 constitutes an alternative to those methods and attempts to close the *material* and *pressure gaps* between model single crystal surfaces, tested under ultra high vacuum conditions, and real catalytic systems.

Well-defined PVP-stabilized monodispersed unsupported Pd nanoparticles (cubes, octahedra and cube-octahedra) were used to study the structure sensitivity of the water-assisted hydrogenation of MBY. The observed activity and selectivity suggested that two types of active sites were involved in the catalysis, which differ in coordination numbers

and are located on planes and edges, respectively. The main premise of this study was that the catalytic behavior of the nanoparticle depended on the relative amounts of each type of active site located on their surfaced. Thus, a single set of intrinsic adsorption and kinetic constants applied on a two-site Langmuir-Hinshelwood mechanism allowed the full kinetic description of any nanoparticle whose surface statistics should be estimated. This, in turn, allowed to predict the most efficient nanoparticle size and shape in terms of a dual activity-selectivity criterion.

Meso-scale rational catalyst design

At this level of complexity, the rational design of a catalyst includes the possible interactions, positive or negative, of the active phase with the species with which it's in close contact. Well-defined Pd nanoparticles prepared via colloidal techniques can be considered as a new generation of model catalysts, which allow overcoming the material and pressure gaps in catalysis. They do present, however, a main drawback. Their synthesis inevitably requires the use of stabilizing and/or capping agents able to tune their size and shape. These substances may alter the observed behavior of the nanoparticles. Three chapters (5-7) were devoted to studying this effect.

The effect of the stabilizing agent used on the structure sensitivity of the water-assisted hydrogenation of MBY was studied in Chapter 5 by comparing the results obtained with PVP and AOT-stabilized Pd nanoparticles using the two-site mechanism previously developed. AOT-stabilized nanoparticles were found to be an order of magnitude more active, but less selective than the PVP-stabilized counterparts. This could be attributed to the stronger interaction of PVP with Pd surface atoms as compared to AOT. The promoting effect on selectivity exerted by PVP probably derived from a dual site-blocking/electronic modification of Pd commonly found in the presence of nitrogen-containing substances.

In order to deepen the understanding of the promoting effect that N-containing additives exert on Pd, Chapter 6 studies the catalytic behavior of supported N-stabilized

Pd nanoparticles in the liquid-phase hydrogenation of 1-hexyne as compared to that of a reference catalyst where no stabilizers were used during its synthesis. The promoting effect was found to arise from two factors, namely a blocking of the active sites towards the intermediate compound and an electronic effect exerted by the N-containing additives. In this Chapter, a support is used for the first time, and given its relatively inertnes, its possible interaction with the active phase is neglected. The N-containing additives were also found to enhance the anchoring of the Pd nanoparticles onto these supports.

Finally, in Chapter 7 a methodology was developed in order to eliminate these organic stabilizing agents. PVP-stabilized Pd cubes were thus supported on CNF-modified SMF structured supports and subjected to UV-Ozone cleaning. Ex-situ XPS analyses showed that N from PVP was already undetectable after 4 h under UVO cleaning whereas in-situ ATR-IR analyses showed that there was a homogeneous decrease of most PVP vibrations and that CO generated from the decomposition of PVP and adsorbed on the surface of Pd. The surface of the Pd nanocubes was found to passivate after the UVO treatment, but no bulk PdO phase was formed. Indeed, high-resolution SEM imaging showed a remarkable morphological stability of the nanocubes even after 6 h of UVO treatment. The catalyst was tested in the hydrogenation of acetylene. The removal of PVP increased the activity of the catalyst fourfold but a slight increase in by-product formation was observed. Furthermore, UVO cleaning was found to increase the number of oxygen-containing groups present on the surface of the CNF/SMF support, thus changing its acid/base properties, which may also influence the observed behavior.

Micro-scaled rational catalyst design

In Chapter 8, the previous levels of complexity are integrated into the study of clean well-defined supported Pd nanoparticles. In order to achieve this, PVP-stabilized Pd nanocubes (6 and 10 nm) as well as cube-octahedra (5.5 nm) were deposited on CNF/SMF and ZnO/SMF supports, PVP eliminated through UVO cleaning and the resulting catalysts

were tested in the hydrogenation of acetylene.

Firstly, the structure sensitivity of the reaction was studied. A model analogous to the one developed in Chapter 4 was successfully applied for this reaction. In this case, however, plane atoms behaved differently depending on the crystallographic plane exposed. Pd_{111} was found to be roughly four times more active than Pd_{100}, which, in turn, was 4 times more active than edge atoms. This observed behavior was rationalized with the C-laydown deposition process known to happen at the beginning of the reaction. This layer hinders hydrogen dissolution, which diminishes the activity of the hydrogenation of acetylene. This phenomenon is known to be disfavored on Pd_{111} surfaces, leading to the increased activity shown from this plane. Selectivity, on the other hand, was not influenced by nanoparticle morphology. Secondly, in this case the effect of the support is also addressed by testing the same nanoparticles on different supports. Pd/ZnO/SMF catalysts were less active and slightly more selective than the Pd/CNF/SMF counterparts. This could be rationalized on the basis of the formation of an intermetallic PdZn phase which modifies the adsorption properties of surface Pd.

An integrated approach for rational catalyst design

This deep study of the catalytic behavior of well-defined Pd-based catalysts throughout several levels of scale and complexity have given us the tools to perform a rational catalyst design for alkyne hydrogenations.

Depending on the specific reaction, the active phase can be optimized in terms of the desired level of activity and selectivity and can be tuned even further with the use of well-chosen additives. N-containing stabilizing agents were found to confer enhanced selectivity to a particular catalyst. Finally, the type of support can be chosen in order to maximize the desired behavior. ZnO-based supports constitute a preferable alternative to C-based supports in terms of selectivity, although activity can be severely compromised.

9.2 Outlook

Two studies are currently ongoing to complete the results shown in this work.

Firstly, a third type of stabilizing agent, this time an inorganic compound will be tried under the same conditions as the nanoparticles shown in Chapters 4 and 5. Cube-octahedral Pd nanoparticles synthesized in the presence of Na_2MoO_4 of roughly 6-7 nm in diameter can be prepared in our facilities. A new method for synthesizing them in a larger size is being developed. These results will be combined with AOT and PVP in order to give a general view of the stabilizer effects encountered in the hydrogenation of MBY depending on the their nature: inorganic compound, surfactant or polymer, respectively.

Secondly, the interesting promoting effect of Zn when ZnO is used as support is currently being investigated in depth with the aid of model powdered catalysts in the gas-phase hydrogenation of MBY. The formation of the bimetallic PdZn phase upon high temperature hydrogen treatment is monitored by temperature programmed reduction (TPR), XPS and XRD. Furthermore, its effect on catalytic behavior as a function of the reduction temperature is studied and compared to that of a standard Pd/Al_2O_3 catalyst. The results of this project are gathered in the following publication:

F. Cardenas-Lizana, M. Crespo-Quesada and L. Kiwi-Minsker. Supported Pd Nanoparticles in the Selective Hydrogenation of 2-methyl-3-butyn-2-ol: Effect of the Support. In preparation.

Finally, the integrated approach herein described could be extended to include the milli and macro-scale levels of rational catalyst design. In order to do this, the optimal supported catalyst should be shaped to be compatible with the chemical reactor in which it would perform. This would imply performing a reactor design specifically for the reaction of interest, concentrating on the mass ans heat transport characteristics of the reactor/catalyst pair as compared to the intrinsic reaction kinetics studied at the nano and meso-scale levels.

Bibliography

[1] R. Schlogl. *Cattech*, 5(3):146–170, 2001.

[2] O. Levenspiel. *Chemical reaction engineering.* Wiley, second edition, 1972.

[3] A. Molnar, A. Sarkany, et al. *Journal of Molecular Catalysis A-Chemical*, 173(1-2):185–221, 2001.

[4] C. J. Jia and F. Schuth. *Physical Chemistry Chemical Physics*, 13(7):2457–2487, 2011.

[5] N. Semagina and L. Kiwi-Minsker. *Catalysis Reviews*, 51(2):147–217, 2009.

[6] M. Bowker. *The basis and applications of heterogeneous catalysis.* Oxford University Press, 1998.

[7] R. E. Oesper. *Journal of Chemical Education*, 25(10):531, 1948.

[8] R. A. van Santen and M. Neurock. *Molecular heterogeneous catalysis.* Wiley-VCH, 2006.

[9] U. S. Ozkan. *Design of heterogeneous catalysts.* Wiley-VCH, 2009.

[10] R. Narayanan and M. A. El-Sayed. *Journal of Physical Chemistry B*, 109(26):12663–12676, 2005.

[11] J. Le Bars, U. Specht, et al. *Langmuir*, 15(22):7621–7625, 1999.

[12] B. Coq and F. Figueras. *Journal of Molecular Catalysis A-Chemical*, 173:117–134, 2001.

[13] C. Burda, X. Chen, et al. *Chemical Reviews*, 105(4):1025–1102, 2005.

[14] T. Teranishi and M. Miyake. *Chemistry of Materials*, 10(2):594–600, 1998.

[15] R. L. Augustine and S. T. O'Leary. *Journal of Molecular Catalysis A-Chemical*, 95(3):277–285, 1995.

[16] D.Y. Murzin. *Journal of Molecular Catalysis A-Chemical*, 315(2):226–230, 2010.

[17] G. C. Bond. *Chemical Society Reviews*, 20(4):441–475, 1991.

[18] H. S. Taylor. *Proceedings of the Royal Society of London Series A*, 108(745):105–111, 1925.

[19] M. Boudart. In *Advances in Catalysis*, volume 20, pages 153–166. Academic Press, 1969.

[20] R. Van Hardeveld and F. Hartog. *Surface Science*, 15(2):189–230, 1969.

[21] G. C. Bond. *Accounts of Chemical Research*, 26(9):490–495, 1993.

[22] M. Che and C. O. Bennett. In *Advances in Catalysis*, volume 36, pages 55–172. Academic Press, 1989.

[23] M. Crespo-Quesada, A. Yarulin, et al. *Journal of the American Chemical Society*, 133(32):12787–12794, 2011.

[24] R. Imbihl and G. Ertl. *Chemical Reviews*, 95(3):697–733, 1995.

[25] G. Ertl. *Surface Science*, 299(1-3):742–754, 1994.

[26] P. L. J. Gunter, J. W. Niemantsverdriet, et al. *Catalysis Reviews-Science and Engineering*, 39(1-2):77–168, 1997.

[27] F. Zaera. *Progress In Surface Science*, 69(1-3):1–98, 2001.

[28] H. J. Freund. *Topics in Catalysis*, 48(1-4):137–144, 2008.

[29] J. Silvestre-Albero, G. Rupprechter, et al. *Journal of Catalysis*, 240(1):58–65, 2006.

[30] J. Silvestre-Albero, G. Rupprechter, et al. *Chemical Communications*, (1):80–82, 2006.

[31] Y. Xia, Y. J. Xiong, et al. *Angewandte Chemie-International Edition*, 48(1):60–103, 2009.

[32] A. R. Tao, S. Habas, et al. *Small*, 4(3):310–325, 2008.

[33] Y. Li, E. Boone, et al. *Langmuir*, 18(12):4921–4925, 2002.

[34] R. Narayanan and M. A. El-Sayed. *Langmuir*, 21(5):2027–2033, 2005.

[35] A. M. Gololobov, I. E. Bekk, et al. *Kinetics and Catalysis*, 50(6):830–836, 2009.

[36] M. Jin, H. Liu, et al. *Nano Research*, 4:83–91, 2011.

[37] A. Y. Stakheev, A. M. Gololobov, et al. *Russian Chemical Bulletin*, 59(9):1713–1719, 2010.

[38] C. Wang, H. Daimon, et al. *Angewandte Chemie-International Edition*, 47(19):3588–3591, 2008.

[39] M. Inaba, M. Ando, et al. *Electrochimica Acta*, 52(4):1632–1638, 2006.

[40] R. Narayanan and M. A. El-Sayed. *Nano Letters*, 4(7):1343–1348, 2004.

[41] R. Narayanan and M. A. El-Sayed. *Journal of Physical Chemistry B*, 108(18):5726–5733, 2004.

[42] H. B. Pan and C. M. Wai. *Journal of Physical Chemistry C*, 114(26):11364–11369, 2010.

[43] N. Semagina, A. Renken, et al. *Journal of Physical Chemistry C*, 111:13933–13937, 2007.

[44] N. Semagina, A. Renken, et al. *Journal of Catalysis*, 246(2):308–314, 2007.

[45] A. C. Gluhoi, J. W. Bakker, et al. *Catalysis Today*, 154(1-2):13–20, 2010.

[46] S. A. Nikolaev and V. V. Smirnov. *Catalysis Today*, 147:336–341, 2009.

[47] A. Sarkany, Z. Schay, et al. *Applied Catalysis A-general*, 380(1-2):133–141, 2010.

[48] N. Semagina and L. Kiwi-Minsker. *Catalysis Letters*, 127(3-4):334–338, 2009.

[49] O. M. Wilson, M. R. Knecht, et al. *Journal of the American Chemical Society*, 128(14):4510–4511, 2006.

[50] J. P. Boitiaux, J. Cosyns, et al. *Applied Catalysis*, 6(1):41–51, 1983.

[51] S. Hub, L. Hilaire, et al. *Applied Catalysis*, 36:307–322, 1988.

[52] A. Borodzinski. *Catalysis Letters*, 71(3-4):169–175, 2001.

[53] A.M. Doyle, S.K. Shaikhutdinov, et al. *Angewandte Chemie-International Edition*, 44(4):629–631, 2005.

[54] Y. A. Ryndin, L. V. Nosova, et al. *Applied Catalysis*, 42:131–141, 1988.

[55] I. Lee, F. Delbecq, et al. *Nature Materials*, 8(2):132–138, 2009.

[56] E. Schmidt, W. Kleist, et al. *Chemistry-A European Journal*, 16:2181–2192, 2010.

[57] I. Lee, M. A. Albiter, et al. *Physical Chemistry Chemical Physics*, 13(7):2449–2456, 2011.

[58] D.Y. Murzin. *Chemical Engineering Science*, 64(5):1046 – 1052, 2009.

[59] D.Y. Murzin. *Journal of Catalysis*, 276(1):85–91, 2010.

[60] C. K. Tsung, J. N. Kuhn, et al. *Journal of the American Chemical Society*, 131(16):5816–5822, 2009.

[61] K. M. Bratlie, H. Lee, et al. *Nano Letters*, 7:3097–3101, 2007.

[62] B. Chen, U. Dingerdissen, et al. *Appl. Catal. A*, 280:17–46, 2005.

[63] J. Rajaram, A. P. S. Narula, et al. *Tetrahedron*, 39(13):2315–2322, 1983.

[64] H. U. Blaser, A. Indolese, et al. *Journal of Molecular Catalysis A-Chemical*, 173(1-2):3–18, 2001.

[65] A. Benedetti, G. Fagherazzi, et al. *Catalysis Letters*, 10(3-4):215–223, 1991.

[66] A. Molnar, G. V. Smith, et al. *Journal of Catalysis*, 101(1):67–72, 1986.

[67] D. Teschner, E. Vass, et al. *Journal of Catalysis*, 242(1):26–37, 2006.

[68] M. Ruta, N. Semagina, et al. *Journal of Physical Chemistry C*, 112(35):13635–13641, 2008.

[69] P. Tribolet and L. Kiwi-Minsker. *Catalysis Today*, 105(3-4):337–343, 2005.

[70] N.A. Zakarina, G.D. Zakumbaeva, et al. *Kinetics and Catalysis*, 24(4):733–737, 1983.

[71] G. D. Zakumbaeva, N. A. Zakarina, et al. *Kinetics and Catalysis*, 24(2):379–383, 1983.

[72] M. M. Telkar, C. V. Rode, et al. *Applied Catalysis A-General*, 273(1-2):11–19, 2004.

[73] N. Semagina, M. Grasemann, et al. *Journal of Catalysis*, 251(1):213–222, 2007.

[74] M. Crespo-Quesada, M. Grasemann, et al. *Catalysis Today*, 147(3-4):247–254, 2009.

[75] E.M. Sulman. *Rus. Chem. Rev.*, 63(11):923–936, 1994.

[76] T. Mallat and A. Baiker. *Applied Catalysis A-General*, 200(1-2):3–22, 2000.

[77] J. Margitfalvi, L. Guczi, et al. *Reaction Kinetics and Catalysis Letters*, 15(4):475–479, 1980.

[78] A. N. R. Bos, E. S. Bootsma, et al. *Chemical Engineering and Processing*, 32(1):53–63, 1993.

[79] A. Borodzinski and A. Cybulski. *Applied Catalysis A-General*, 198(1-2):51–66, 2000.

[80] J. A. Anderson, J. Mellor, et al. *Journal of Catalysis*, 261(2):208–216, 2009.

[81] M. Crespo-Quesada, R. R. Dykeman, et al. *Journal of Catalysis*, 279(1):66–74, 2011.

[82] T. Sakai and P. Alexandridis. *Langmuir*, 20(20):8426–8430, 2004.

[83] Y. Li, X.M. Hong, et al. *Organic Letters*, 2:2385, 2000.

[84] S. N. Sidorov, I. V. Volkov, et al. *Journal of the American Chemical Society*, 123:10502–10510, 2001.

[85] A. Borsla, A. M. Wilhelm, et al. *Catalysis Today*, 66(2-4):389–395, 2001.

[86] R.W.J. Scott, A.K. Datye, et al. *Journal of the American Chemical Society*, 125:3708, 2003.

[87] L.M. Bronstein, D.M. Chernyshov, et al. *Journal of Catalysis*, 196(2):302–314, 2000.

[88] S. Eriksson, U. Nylen, et al. *Applied Catalysis A-general*, 265:207–219, 2004.

[89] J. Agrell, G. Germani, et al. *Applied Catalysis A-general*, 242:233–245, 2003.

[90] H. Bonnemann, W. Brijoux, et al. *Topics in Catalysis*, 4:217–227, 1997.

[91] A.J. Zarur and J.Y. Ying. *Nature*, 403:65–67, 2000.

[92] D.G. Shchukin and G.B. Sukhorukov. *Advanced Materials*, 16(8):671–682, 2004.

[93] R. M. Rioux, H. Song, et al. *Journal of Physical Chemistry B*, 109(6):2192–2202, 2005.

[94] H. Song, R. M. Rioux, et al. *Journal of the American Chemical Society*, 128(9):3027–3037, 2006.

[95] Y. W. Zhang, M. E. Grass, et al. *Journal of Physical Chemistry C*, 111(33):12243–12253, 2007.

[96] S. H. Joo, J. Y. Park, et al. *Nano Letters*, 10(7):2709–2713, 2010.

[97] M. Boutonnet, J. Kizling, et al. *Colloids and Surfaces*, 5:209–225, 1982.

[98] M. Boutonnet, J. Kizling, et al. *Applied Catalysis*, 20:163–177, 1986.

[99] M. Boutonnet, J. Kizling, et al. *Journal of Catalysis*, 103:95–104, 1987.

[100] D.H. Chen, C.C. Wang, et al. *Journal of Colloid and Interface Science*, 210:123–129, 1999.

[101] N. Semagina, E. Joannet, et al. *Applied Catalysis a-General*, 280(2):141–147, 2005.

[102] N. R. Jana and X. G. Peng. *Journal of the American Chemical Society*, 125(47):14280–14281, 2003.

[103] N. Toshima, Y. Shiraishi, et al. *Applied Organometallic Chemistry*, 15(3):178–196, 2001.

[104] M. Ganesan, R. G. Freemantle, et al. *Chemistry of Materials*, 19(14):3464–3471, 2007.

[105] C. B. Murray, C. R. Kagan, et al. *Annual Review of Materials Science*, 30:545–610, 2000.

[106] B.D. Busbee, S.O. Obare, et al. *Advanced Materials*, 15:414–416, 2003.

[107] S. Link and M.A. El-Sayed. *Journal of Physical Chemistry B*, 103:8410–8426, 1999.

[108] B. Lim, M. J. Jiang, et al. *Advanced Functional Materials*, 19(2):189–200, 2009.

[109] Y. Sun and Y. Xia. *Science*, 298(5601):2176–2179, 2002.

[110] Y. J. Xiong, J. Y. Chen, et al. *Nano Letters*, 5(7):1237–1242, 2005.

[111] G. Chang, M. Oyama, et al. *Acta Materialia*, 55(10):3453–3456, 2007.

[112] Y. J. Xiong, B. Wiley, et al. *Angewandte Chemie-International Edition*, 44:7913–7917, 2005.

[113] J. Y. Chen, J. M. McLellan, et al. *Journal of the American Chemical Society*, 128(46):14776–14777, 2006.

[114] N. Pinna, K. Weiss, et al. *Advanced Materials*, 13:261–264, 2001.

[115] F.M.V. Kooij, K. Kassapidou, et al. *Nature*, 406:868–871, 2000.

[116] R.C. Jin, Y.W. Cao, et al. *Science*, 294:1901–1903, 2001.

[117] Y. J. Xiong, J. M. McLellan, et al. *Journal of the American Chemical Society*, 127(48):17118–17127, 2005.

[118] Y. J. Xiong, H. G. Cai, et al. *Journal of the American Chemical Society*, 129(12):3665–3675, 2007.

[119] Y. J. Xiong and Y. N. Xia. *Advanced Materials*, 19(20):3385–3391, 2007.

[120] G. Kickelbick. *Progress in Polymer Science*, 28:83–114, 2003.

[121] T. K. Sau and C. J. Murphy. *Journal of the American Chemical Society*, 126(28):8648–8649, 2004.

[122] Y. Sun and Y. Xia. *Advanced Materials*, 14:833–837, 2002.

[123] S. H. Chen, Z. L. Wang, et al. *Journal of the American Chemical Society*, 125(52):16186–16187, 2003.

[124] M. P. Pileni. *Nature Materials*, 2(3):145–150, 2003.

[125] C.J. Johnson, E. Dujardin, et al. *Journal of Materials Chemistry*, 12:1765–1770, 2002.

[126] B. Wiley, Y. G. Sun, et al. *Accounts of Chemical Research*, 40(10):1067–1076, 2007.

[127] F. Kim, S. Connor, et al. *Angewandte Chemie-International Edition*, 43(28):3673–3677, 2004.

[128] S. E. Habas, H. Lee, et al. *Nature Materials*, 6(9):692–697, 2007.

[129] B. Lim, Y. J. Xiong, et al. *Angewandte Chemie-International Edition*, 46(48):9279–9282, 2007.

[130] H. Song, F. Kim, et al. *Journal of Physical Chemistry B*, 109(1):188–193, 2005.

[131] M. E. Grass, Y. Yue, et al. *Journal of Physical Chemistry C*, 112(13):4797–4804, 2008.

[132] Andrzej Cybulski and Jacob A. Moulijn, editors. *Structured catalysts and reactors*. Marcel Dekker, Inc., second edition, 2006.

[133] T.A. Nijhuis, G. van Koten, et al. *Applied Catalysis A-general*, 238:259–271, 2003.

[134] J. M. Winterbottom, H. Marwan, et al. *Catalysis Today*, 79(1-4):391–399, 2003.

[135] A.N. Karavanov, V.M. Gryaznov, et al. *Catalysis Today*, 25:447–450, 1995.

[136] V. Holler, K. Radevik, et al. *Industrial Engineering Chemistry Research*, 40(6):1575–1579, 2001.

[137] L. Kiwi-Minsker, E. Joannet, et al. *Industrial Engineering Chemical Research*, 44(16):6148–6153, 2005.

[138] N. Semagina, A. Renken, et al. *Chemical Engineering Science*, 62(18-20):5344–5348, 2007.

[139] D.R. Cahela and B.J. Tatarchuk. *Catalysis Today*, 69:33–39, 2001.

[140] J. De Greef, G. Desmet, et al. *Catalysis Today*, 105(3-4):331–336, 2005.

[141] I. Cerri, M. Pavese, et al. *Catalysis Today*, 83:19–31, 2003.

[142] I. Yuranov, A. Renken, et al. *Applied Catalysis A-general*, 281:55–60, 2005.

[143] M. Ruta, I. Yuranov, et al. *Journal of Catalysis*, 247(2):269–276, 2007.

[144] M. Ruta, G. Laurenczy, et al. *Journal of Physical Chemistry C*, 112(46):17814–17819, 2008.

[145] M. Grasemann, N. Semagina, et al. *Industrial Engineering Chemical Research*, 2007.

[146] G. Wiessmeier and D. Hnicke. *Industrial Engineering Chemical Research*, 35:4412–4416, 1996.

[147] C. Fukuhara, H. Ohkura, et al. *Applied Catalysis A-general*, 273:125–132, 2004.

[148] B. Kucharczyk, W. Tylus, et al. *Applied Catalysis B-environmental*, 49:27–37, 2004.

[149] N. Jarrah, J. G. van Ommen, et al. *Catalysis Today*, 79(1-4):29–33, 2003.

[150] K. Nikolajsen, L. Kiwi-Minsker, et al. *Chemical Engineering Research and Design*, 84(7):562–568, 2006.

[151] A.R. Pradhan, M.A. Macnaughtan, and D. Raftery. *Journal of the American Chemical Society*, 122:404–405, 2000.

[152] Kim Nikolajsen. PhD thesis, EPFL, Lausanne, 2007.

[153] E. Auer, A. Freund, J. Pietsch, et al. *Applied Catalysis A-general*, 173(2):259–271, 1998.

[154] F. Rodriguez-Reinoso. *Carbon*, 36(3):159–175, 1998.

[155] C. Park and M. A. Keane. *Journal of Colloid and Interface Science*, 266(1):183–194, 2003.

[156] P. Tribolet and L. Kiwi-Minsker. *Catalysis Today*, 102-103:15–22, 2005.

[157] M. L. Toebes, Y. H. Zhang, et al. *Journal of Catalysis*, 226(1):215–225, 2004.

[158] R. T. K. Baker, M. A. Barber, et al. *Journal of Catalysis*, 26(1):51–62, 1972.

[159] N. M. Rodriguez. *Journal of Materials Research*, 8(12):3233–3250, 1993.

[160] M. L. Toebes, E. M. P. van Heeswijk, et al. *Carbon*, 42(2):307–315, 2004.

[161] H. P. Boehm. *Carbon*, 40(2):145–149, 2002.

[162] H. Bonnemann, W. Brijoux, et al. *Applied Organometallic Chemistry*, 11:783–796, 1997.

[163] S. J. Tauster, S. C. Fung, et al. *Journal of the American Chemical Society*, 100(1):170–175, 1978.

[164] H. Lindlar. *Helvetica Chimica Acta*, 35(2):446–456, 1952.

[165] R. Schlogl, K. Noack, et al. *Helvetica Chimica Acta*, 70:627–679, 1987.

[166] D. Lee, J. Y. Lee, et al. *Carbon Dioxide Utilization For Global Sustainability*, 153:169–172, 2004.

[167] A. Sarkany, Z. Zsoldos, et al. *Journal of Catalysis*, 141:566–582, 1993.

[168] M. G. Musolino, C. Busacca, et al. *Applied Catalysis A-general*, 379(1-2):77–86, 2010.

[169] N. Iwasa, S. Masuda, et al. *Applied Catalysis A-general*, 125:145–157, 1995.

[170] P. S. Wehner, G. C. Tustin, et al. *Journal of Catalysis*, 88(1):246–248, 1984.

[171] Z. Zsoldos, A. Sarkany, et al. *Journal of Catalysis*, 145(1):235–238, 1994.

[172] E. Jeroro and J. M. Vohs. *Catalysis Letters*, 130(3-4):271–277, 2009.

[173] E. Jeroro, M. P. Hyman, et al. *Physical Chemistry Chemical Physics*, 11(44):10457–10465, 2009.

[174] E. Jeroro and J. M. Vohs. *Journal of Physical Chemistry C*, 113(4):1486–1494, 2009.

[175] T.A. Nijhuis, G. van Koten, et al. *Catalysis Today*, 79-80:315–321, 2003.

[176] J. Yu and J.B. Spencer. *Chemical Communications*, pages 1103–1104, 1998.

[177] R. Tschan, M.M. Schubert, et al. *Catalysis Letters*, 75:31–36, 2001.

[178] J. P. Boitiaux, J. Cosyns, et al. *Applied Catalysis*, 15(2):317–326, 1985.

[179] L. Kiwi-Minsker, N. Semagina, et al. In *Metal Nanoclusters in Catalysis and Materials Science*, pages 293–299. Elsevier, 2008.

[180] Friedrich G. Helfferich. Kinetics of multistep reactions. volume 40 of *Comprehensive Chemical Kinetics*, pages 1–488. Elsevier, 2004.

[181] M. Sasaki, M. Osada, et al. *Journal of Molecular Catalysis A-chemical*, 141(1-3):223–240, 1999.

[182] I. Balint, A. Miyazaki, et al. *Physical Chemistry Chemical Physics*, 6(9):2000–2002, 2004.

[183] J. P. Boitiaux, J. Cosyns, et al. *Applied Catalysis*, 32(1-2):145–168, 1987.

[184] S. Bhattacharjee, D. M. Dotzauer, et al. *Journal of the American Chemical Society*, 131(10):3601–3610, 2009.

[185] L. Piccolo, A. Valcarcel, et al. *Physical Chemistry Chemical Physics*, 10(36):5504–5506, 2008.

[186] A. Quintanilla, V. C. L. Butselaar-Orthlieb, et al. *Journal of Catalysis*, 271(1):104–114, 2010.

[187] R. Ma and N. Semagina. *Journal of Physical Chemistry C*, 114(36):15417–15423, 2010.

[188] U. K. Singh and M. A. Vannice. *Journal of Catalysis*, 191(1):165–180, 2000.

[189] R.I. Macey and G.F. Oster. *Berkeley MadonnaTM*, 1997-2001.

[190] H. Lee, S. E. Habas, et al. *Angewandte Chemie-International Edition*, 45(46):7824–7828, 2006.

[191] E. Sulman, Y. Bodrova, et al. *Applied Catalysis A: General*, 176(1):75–81, 1999.

[192] N. Semagina, A. V. Bykov, et al. *Journal of Molecular Catalysis A-chemical*, 208(1-2):273–284, 2004.

[193] T. Welton. *Coordination Chemistry Reviews*, 248(21-24):2459–2477, 2004.

[194] J. P. T. Mikkola, P. P. Virtanen, et al. *Applied Catalysis A-General*, 328(1):68–76, 2007.

[195] J. P. Mikkola, P. Virtanen, et al. *Green Chemistry*, 8(2):197–205, 2006.

[196] I. Chorkendorff and J.W. Niemantsverdriet. *Concepts of modern catalysis and kinetics*. Wiley-VCH, 2003.

[197] D. B. Zhao, Z. F. Fei, et al. *Inorganic Chemistry*, 43(6):2197–2205, 2004.

[198] P. J. Dyson, G. Laurenczy, et al. *Chemical Communications*, (19):2418–2419, 2003.

[199] D. W. Rogers, E. Crooks, and K. Dejroongruang. *Journal of Chemical Thermodynamics*, 19(11):1209–1215, 1987.

[200] T. Kasprzycka-Guttman. *The Thermochemistry of the CC Bond.* John Wiley & Sons, Ltd, 2004.

[201] W. Woodside and J. H. Messmer. *Journal of Applied Physics*, 32(9):1688, 1961.

[202] C. N. Satterfield. *Mass Transfer in Heterogeneous Catalysis.* MIT Press, 1970.

[203] W. Hayduk and B. S. Minhas. *Canadian Journal of Chemical Engineering*, 60(2):295–299, 1982.

[204] P. B. Weisz and C. D. Prater. In V. I. Komarewsky W.G. Frankenburg and E. K. Rideal, editors, *Advances in Catalysis*, volume 6. Academic Press, 1954.

[205] C. Brasquet and P. Le Cloirec. *Chemical Engineering Science*, 55(15):2767–2778, 2000.

[206] H. H. Rosenbrock and C. Storey. *Computational Techniques for Chemical Engineers.* Pergamon Press, Oxford, 1966.

[207] A. Bruehwiler, N. Semagina, et al. *Industrial & Engineering Chemistry Research*, 47(18):6862–6869, 2008.

[208] Y. G. Cui, I. Biondi, et al. *Physical Chemistry Chemical Physics*, 12(8):1834–1841, 2010.

[209] N. Yan, X. Yang, et al. *Organometallics*, 28(4):937–939, 2009.

[210] L. Zhou and L. Wang. *Synthesis-Stuttgart*, (16):2653–2658, 2006.

[211] G. A. Somorjai. *Science*, 227(4689):902–908, 1985.

[212] S. Biniak, G. Szymanski, et al. *Carbon*, 35(12):1799–1810, 1997.

[213] Z. R. Yue, W. Jiang, et al. *Carbon*, 37(11):1785–1796, 1999.

[214] M. Besson and P. Gallezot. *Catalysis Today*, 81:547–559, 2003.

[215] J. Panpranot, O. Tangjitwattakorn, et al. *Applied Catalysis A-General*, 292:322–327, 2005.

[216] J. G. Ulan and W. F. Maier. *Journal of Molecular Catalysis*, 54(2):243–261, 1989.

[217] A. C. Kizilkaya, J. M. Gracia, et al. *Journal of Physical Chemistry C*, 114(49):21672–21680, 2010.

[218] C. J. Zhang and P. Hu. *Journal of the American Chemical Society*, 123(6):1166–1172, 2001.

[219] G. C. Wang and J. Nakamura. *Journal of Physical Chemistry Letters*, 1(20):3053–3057, 2010.

[220] J. Grunes, J. Zhu, et al. *Journal of Physical Chemistry B*, 106(44):11463–11468, 2002.

[221] B. Gehl, A. Framsdorf, et al. *Advanced Functional Materials*, 18(16):2398–2410, 2008.

[222] C. Lange, D. De Caro, et al. *Langmuir*, 15(16):5333–5338, 1999.

[223] Z. L. Wang, J. M. Petroski, et al. *Journal of Physical Chemistry B*, 102(32):6145–6151, 1998.

[224] R. Yu, H. Song, et al. *Journal of Physical Chemistry B*, 109(15):6940–6943, 2005.

[225] I. Lee, R. Morales, et al. *Proceedings of the National Academy of Sciences of the United States of America*, 105(40):15241–15246, 2008.

[226] J. R. Vig. *Journal of Vacuum Science and Technology A-Vacuum Surfaces and Films*, 3(3):1027–1034, 1985.

[227] C. Aliaga, J. Y. Park, et al. *The Journal of Physical Chemistry C*, 113(15):6150–6155, 2009.

[228] S. Pang, Y. Kurosawa, et al. *Chemistry Letters*, 34(4):544–545, 2005.

[229] P. Siffalovic, L. Chitu, et al. *Langmuir*, 26(8):5451–5455, 2010.

[230] S. Penner, W. Di, et al. *Journal of Chemical Physics*, 125(9), 2006.

[231] G. Zheng and E. I. Altman. *Surface Science*, 504(1-3):253–270, 2002.

[232] E. Lundgren, J. Gustafson, et al. *Physical Review Letters*, 92(4), 2004.

[233] Y. Borodko, S. E. Habas, et al. *The Journal of Physical Chemistry B*, 110(46):23052–23059, 2006.

[234] J. Szanyi, W. K. Kuhn, et al. *Journal of Vacuum Science and Technology A - Vacuum Surfaces and Films*, 11(4):1969–1974, 1993.

[235] T. Burgi. *Physical Chemistry Chemical Physics*, 3(11):2124–2130, 2001.

[236] J. S. Bradley, J. M. Millar, et al. *Faraday Discussions*, 92:255–268, 1991.

[237] A. Borodzinski and G. C. Bond. *Catalysis Reviews-Science and Engineering*, 50(3):379–469, 2008.

[238] M. L. Toebes, J. A. van Dillen, et al. *Journal of Molecular Catalysis A-Chemical*, 173(1-2):75–98, 2001.

[239] U. Schroder and N. H. Schoon. *Journal of Catalysis*, 143(2):381–387, 1993.

[240] L. Cider and N. H. Schoon. *Applied Catalysis*, 68(1-2):191–205, 1991.

[241] L. Cider, U. Schroder, et al. *Journal of Molecular Catalysis*, 67(3):323–331, 1991.

[242] A. H. Weiss, B. S. Gambhir, et al. *Industrial and Engineering Chemistry Process Design and Development*, 16(3):352–357, 1977.

[243] J. T. Wehrli, D. J. Thomas, et al. *Applied Catalysis*, 70(2):253–262, 1991.

[244] M. Primet, M. El Azhar, et al. *Applied Catalysis*, 58(1):241–253, 1990.

[245] C. Rottman and M. Wortis. *Physical Review B*, 24(11):6274–6277, 1981.

[246] A. Roucoux, J. Schulz, et al. *Chemical Reviews*, 102(10):3757–3778, 2002.

[247] R. J. Madon and M. Boudart. *Industrial & Engineering Chemistry Fundamentals*, 21(4):438–447, 1982.

[248] A. M. Doyle, S.l K. Shaikhutdinov, et al. *Angewandte Chemie International Edition*, 42(42):5240–5243, 2003.

[249] L. Gracia, M. Calatayud, et al. *Physical Review B*, 71(3), 2005.

[250] M. W. Tew, H. Emerich, et al. *Journal of Physical Chemistry C*, 115(17):8457–8465, 2011.

Curriculum Vitae

Education

2007-2011 **Ecole Polytechnique Fédérale de Lausanne** **Switzerland**

PhD in Chemical Engineering at the Group of Catalytic Reaction Engineering (GGRC)

2002-2007 **Universitat de Barcelona** **Spain**

Master's diploma in Chemical Engineering

1998-2002 **Colegio Nacional Arturo Umberto Illia** **Argentina**

High-school diploma (Scientific orientation)

Publications

- M. Crespo-Quesada, A. Yarulin, M. Jin, Y. Xia, and L. Kiwi-Minsker. The Structure Sensitivity of Alkynol Hydrogenation on Shape- and Size-Controlled Pd Nanocrystals: Which Sites Are Most Active and Selective? *Journal of the American Chemical Society*, 133(32):12787-12794, 2011.

- M. Crespo-Quesada, J.M. Andanson, A. Yarulin, B. Lim, Y. Xia, and L. Kiwi-Minsker. UV–Ozone Cleaning of Supported Poly (Vinyl Pyrrolidone)-Stabilized Palladium Nanocubes: Effect of Stabilizer Removal on Morphology and Catalytic Behavior. *Langmuir*, 27(12):7909-7916, 2011.

- M. Crespo-Quesada, R. Dykeman, G. Laurenczy, P. Dyson, and L. Kiwi-Minsker.

Supported Nitrogen-Modified Pd Nanoparticles for the Selective Hydrogenation of 1-hexyne. *Journal of Catalysis*, 279(1):66-74, 2011.

- M. Crespo-Quesada and L. Kiwi-Minsker. Size-Tailored Pd Nanoparticles in the Selective Hydrogenation of 2-methyl-3-butyn-2-ol: Effect of the Stabilizing Agent. Submitted.

- L. Kiwi-Minsker and M. Crespo-Quesada. Integrated Approach for Intensification of Heterogeneous Catalytic Processes. *CHIMIA*, 65(9):699, 2011.

- A. Yarulin, M. Crespo-Quesada, E. Egorova, L. Kiwi-Minsker. Structure Sensitivity of Acetylene Hydrogenation Over Catalysts with Shape-Controlled Palladium Nanoparticles. *Kinetics and Catalysis*, Accepted, 2011.

- M. Crespo-Quesada, M. Grasemann, N. Semagina, A. Renken, and L. Kiwi-Minsker. Kinetics of the Solvent-Free Hydrogenation of 2-methyl-3-butyn-2-ol Over a Structured Pd-Based Catalyst. *Catalysis Today*, 147(3-4):247-254, 2009.

- X. Yang, N. Yan, Z. F. Fei, M. Crespo-Quesada, G. Laurenczy, L. Kiwi-Minsker, Y. Kou, Y. D. Li, and P. J. Dyson. Biphasic Hydrogenation Over PVP Stabilized Rh Nanoparticles in Hydroxyl Functionalized Ionic Liquids. *Inorganic Chemistry*, 47(17): 7444-7446, 2008.

Publications in preparation

- M. Crespo-Quesada, C. Voisard, A. Yarulin, Y. Xia and L. Kiwi-Minsker. Shape and Size-Tailored Supported Pd Nanoparticles in the Hydrogenation of Acetylene.

- F. Cardenas-Lizana, M. Crespo-Quesada and L. Kiwi-Minsker. Supported Pd nanoparticles in the selective hydrogenation of 2-methyl-3-butyn-2-ol: Effect of the Support.

Presentations

- EuropaCat X. August 28th - September 2nd, 2011. Glasgow, United Kingdom. *Oral presentation.*
- 19th International congress of chemical and process engineering CHISA 2010 & 7th European congress of chemical engineering ECCE7. August 28th - September 1st, 2010. Prague, Czech Republic. *Oral presentation.*
- 10th International symposium on the scientific bases for the preparation of heterogeneous catalysts, PREPA10. July 11th - 15th, 2010. Louvain-la-neuve, Belgium. *Oral presentation.*
- Workshop single sites in heterogeneous catalysis, NANO-HOST. September 28th - 29th, 2009. Milan, Italy. *Poster presentation.*

Languages

- Spanish - Mother tongue
- English - Fluent
- French - Good knowledge
- Italian - Good knowledge